Oxidation protection of carbon/carbon composites and non- destructive characterization methodology development

Jiaping Zhang

Sorbonne Université

Ecole doctorale

L'ECOLE DOCTORALE DE CHIMIE PHYSIQUE ET DE

CHIMIE ANALYTIQUE DE PARIS CENTRE (ED 388)

Oxidation protection of carbon/carbon composites and non-destructive characterization methodology development

Par [Jiaping ZHANG]

Thèse de doctorat de Chimie Physique et Chimie Analytique

Dirigée par [Philippe JONNARD et Qiangang FU]

Présentée et soutenue publiquement le [28 June 2019]

Devant un jury composé de :

M. Zhanshan WANG	Professeur	Tongji University	(Rapporteur)
M. Fei MA	Professeur	Xi'an Jiaotong University	(Rapporteur)
M. Ahmed NAITABDI	Maître de Conférences	Sorbonne Université	(Examinateur)
Mme. Xiaoli FAN	Professeur	Northwestern Polytechnical University	(Examinatrice)
M. Philippe JONNARD	Directeur de recherche	Sorbonne Université	(Directeur de thèse)
M. Qiangang FU	Professeur	Northwestern Polytechnical University	(Co-directeur de thèse)

Acknowledgements

This thesis presents the work I have done in Northwestern Polytechnical University (NWPU) and Sorbonne Université (SU). Here I would like to express my sincere gratitude to my supervisors, Dr. Philippe Jonnard and Dr. Qiangang Fu, for not only their immense knowledge and sharp insights to research, but also enthusiastic supports and encouragements. Specially, I owe my thanks to Dr. Fu for encouraging me to expand my horizon by studying abroad, and to Dr. Jonnard for recruiting me and making possible a wonderful research experience of me in Paris. They teach me the ability to perform independent research. I am very happy and lucky to work with them.

I would like to thank Dr. Karine Le Guen from the team for her valuable advices in revising the thesis and the paper. She always corrects carefully what I write and gives useful comments.

Special thanks to Dr. Alain Dubois for all his warm help from scholarship application to administrative procedures in SU. I am also very grateful for his help in my daily life.

I would like to give my thanks to all the jury members, Dr. Ahmed Naitabdi, Dr. Zhanshan Wang, Dr. Fei Ma and Dr. Xiaoli Fan, for accepting the invitation of evaluating my work.

I would like to thank Ian Vickridge and Didier Schmaus of Institut des NanoSciences de Paris (INSP) for allowing me to work on the SAFIR platform. Thanks also to them for the useful discussions in finishing the project.

Thanks for the financial supports provided by the Erasmus+ mobility scholarship and the China Scholarship Council -SU doctoral program.

I would like to thank all my friends and colleagues in our lab: Christopher, Aladine, Meiyi, Mostafa, Hang, Athony, Atoine, Marie, Sevan, Xuan, Lucia, etc.

I would like to thank my family: they support me all the time until finishing my Ph.D.

Jiaping

Paris, April 2019

Contents

Chapter 1: Introduction

1.1 Carbon/carbon composites

Carbon can be considered as an excellent high temperature material. It can form many allotropes. Among them, diamond (carbon atoms bonded in a tetrahedral lattice arrangement) and graphite (carbon atoms bonded in sheets of a hexagonal lattice) are the two most representative ones. Compared with traditional alloys (Ni-based or Nb-based alloys), graphite has no melting point and its sublimation temperature is up to 3620°C [1]. Based on these unique properties, graphite is suitable for use in thermal protection systems at high temperature. Unfortunately, its poor mechanical properties limit its applications. To overcome the obstacles, carbon/carbon (C/C) composites were developed. C/C composites, consist of carbon fibers reinforcement embedded in a carbonaceous matrix, as shown in Figure 1-1. It could combine the good mechanical performances of the carbon fibers and the excellent high temperature properties of the carbon matrix.

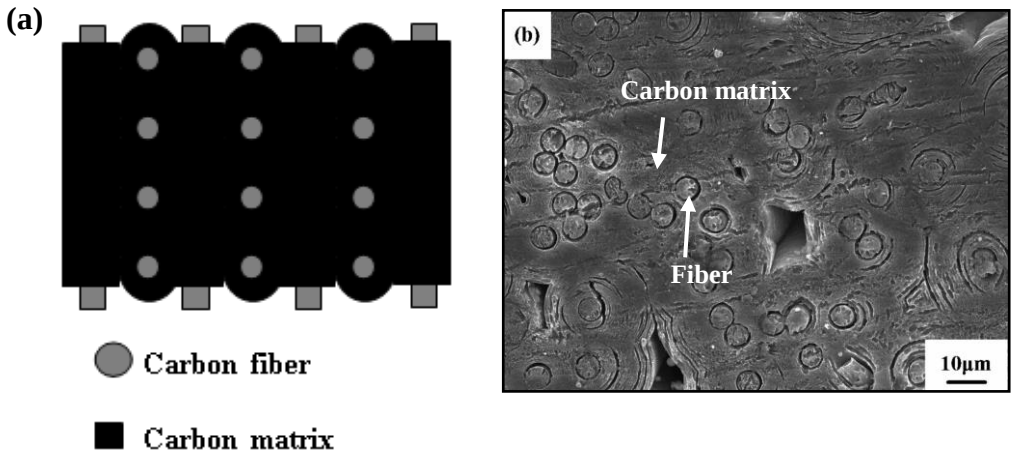

Figure 1-1. Schematic illustration (a) and microstructure (b) of C/C composites.

The preparation process of C/C composites is mainly composed of two steps: manufacturing carbon fiber reinforcements and carbon matrix densification. Polyacrylonitrile (PAN)-based and pitch-based carbon fibers are the two typical ones used in carbon reinforcements [2, 3]. Fibers are usually woven in appropriate directions to tailor specific properties [4, 5]. According to the structure differences, the carbon fiber reinforcements can be divided into stacked non-woven layers, needled carbon fiber felts and carbon fiber textiles. For the densification process, chemical vapor infiltration (CVI) and liquid impregnation and

carbonization are the two common methods, which could fill the pores in the carbon fiber reinforcements. Hydrocarbon gases are used as the precursor of CVI. Because of its easy supply and good diffusion rate in carbon fibers reinforcement, methane is the most common used gas in this process [2]. At temperatures of 1000-1400°C, methane could convert into a carbonaceous solid medium (called as pyrocarbon) according to the following reaction (1-1), which could fill the pores of the fiber reinforcements.

$$CH_4\,(g) \rightarrow C\,(s) + 2\,H_2(g) \qquad (1\text{-}1)$$

As for the liquid impregnation and carbonization, the fiber preform is firstly impregnated into a resin (or pitch) and then carbonized at high temperatures for several cycles to reduce its porosity. Phenolic resin is commonly used owing to its low price and relatively higher yield of carbon during decomposition at high temperature [3].

1.2 Application of carbon/carbon composites

C/C composites possess many unique properties, such as low-density (< 2.0 g/cm^3), high specific strength/modulus, low coefficient of thermal expansion, good friction property, excellent thermal shock resistance and so on. Figure 1-2 displays the high-temperature mechanical properties of different materials. Compared with other materials, C/C composites have higher retention of mechanical properties at high temperatures, which ensure them to be the promising candidates for the fabrication of thermal-structural components at extreme temperatures [2-7]. So C/C composites have been used as the structural materials in vehicle heat shields, rocket nozzles and aircraft brakes. Additionally, properties such as biocompatibility, chemical inertness and good mechanical property also ensure them to be used in medicine and industry.

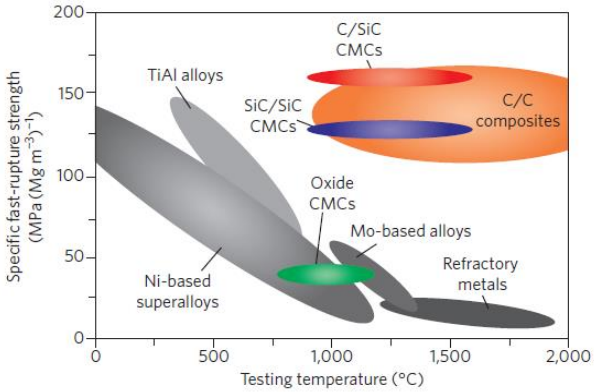

Figure 1-2. High-temperature mechanical properties of various materials, specific fast-rupture strength as a function of the temperature of various metals and composites [8].

However, there exists fiber/matrix interface, micro-pores, micro-cracks, crystal defects, residual stress and impurity particles in C/C [2, 3]. They could act as the active pots of oxidation. The oxidation reaction can be performed according to the following reaction:

$$2\,C\,(s) + O_2\,(g) \rightarrow 2\,CO\,(g) \qquad (1\text{-}2)$$

The reaction has a large driving force because of its negative value of Gibbs free energy change. In actual environment, the oxidation rate of C/C is complicated because it is determined not by the chemical reaction itself, but also by the transport of the gaseous species. In generally, at lower temperatures (below 600-800°C), oxidation is controlled by the reaction of oxygen with active sites on the carbon surface. At higher temperatures, the oxidation rate is determined by the diffusion of oxygen through the boundary layer at the C/C surface. Compared with oxidation (usually performed in static air at high temperatures) [6, 9, 10], ablation represents the phenomenon that materials are subjected to thermo-mechanical, thermo-chemical and thermo-physical erosions from a heat source at high temperature, pressure and velocity. For C/C, during ablation, appreciable amounts of the heat flux are converted to an outward mass flux through the oxidation consumption, leading to a mass loss. So, although the composites could meet the mechanical requirements, rapid oxidation of carbon fiber and carbon matrix in an oxidizing environment severely limits their wide applications. Coating technology and carbon matrix modification are regarded as the two effective ways to enhance the oxidation/ablation resistance of C/C composites.

1.3 Coating technology

The aim of coating technology is to isolate C/C from the oxidizing environments. The requirements for a protective coating system are shown in Figure 1-3, which are listed as follow:

(1) chemical compatibility with the C/C substrate, especially to prevent outward diffusion of carbon and avoid the reaction of the substrate and the coating.

(2) thermo-physical compatibility, mainly representing the thermal expansion coefficient match.

(3) diffusion stability when in contact with chemical compounds.

(5) low oxygen permeability to prevent the inward diffusion of oxidized species.

(6) low volatility to prevent excessive ablation in high-velocity gas streams.

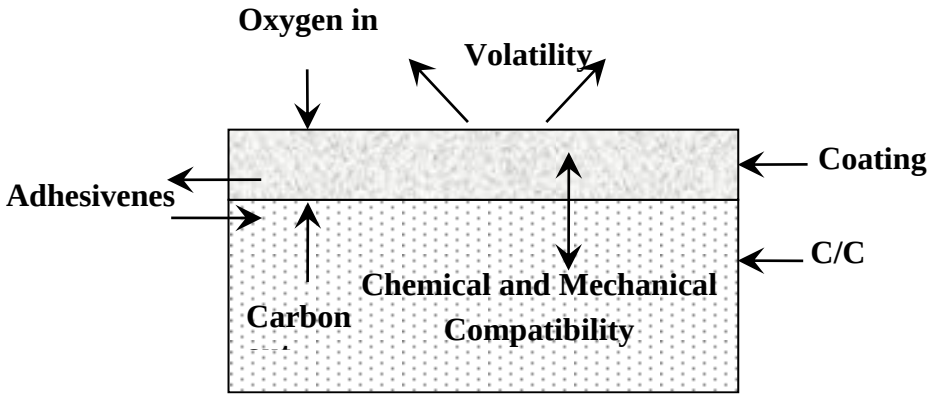

Figure 1-3. Requirements for the coating on the surface of C/C composites [2, 11].

Many methods have been performed to prepare protective coating on the surface of C/C composites. Si-based ceramics (such as SiC and $MoSi_2$) and ultra-high-temperature ceramics (UHTCs) or a combination of them are commonly used as the coating materials. The selection of Si-based ceramics can be mainly attributed to the self-sealing performance of the formed glassy SiO_2 (the oxidation product of Si-based ceramics) at high temperature. UHTCs representing the carbides, nitrides and borides of refractory metals, are used because of their high-melting points, good mechanical properties, oxidation performances and ablation resistances [12-16]. Table 1-1 shows the basic physical properties of C/C, SiC, $MoSi_2$ and some typical UHTCs. Many methods have been developed to fabricate the protective coating on the surface of C/C. The most commonly used ones are pack cementation, chemical vapor deposition and plasma spraying. Each method is briefly described, as follow.

Table 1-1. Properties of SiC, $MoSi_2$ and some typical UHTCs [17-20]. CTE is the coefficient of thermal expansion.

Property	C/C	SiC	$MoSi_2$	HfC	ZrC	TaC	HfB_2	ZrB_2
Density (g/cm^3)	1.75	3.2	6.26	12.7	6.6	14.5	11.2	6.10
Melting point (°C)	-	2700	2030	3890	3540	3880	3380	3245
CTE ($10^{-6}/K$)	1-2	4.3	8.25	6.8	7.3	6.6	6.3	5.9

(1) Pack cementation

During pack cementation, C/C composites are immersed into the mixed powders of the coating materials and then heat-treated at high temperature. The molten coating materials will infiltrate into C/C or react with carbon matrix to form the ceramic coatings. Ren et al. [21] adopted this method to prepare SiC coating on the surface of C/C, as shown in Figure 1-4. The prepared coating showed a good adhesive strength with the C/C substrate.

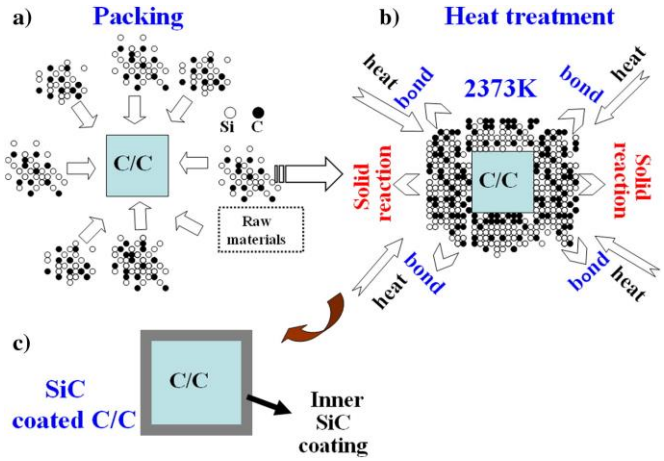

Figure 1-4. Schematic diagram of the SiC coating prepared by pack cementation [21].

(2) Chemical vapor deposition (CVD)

CVD is a deposition method used to produce high quality, high-performance solid materials. The process mainly consists of the dissociation and/or chemical reactions of gaseous reactants and the deposition of a stable solid product. HfC coating was successfully prepared by this method [22], as shown in Figure 1-5. The prepared coating shows a dense structure. However, due to the low deposition rates, the processing times of CVD are long, resulting in the increase of manufacturing cost.

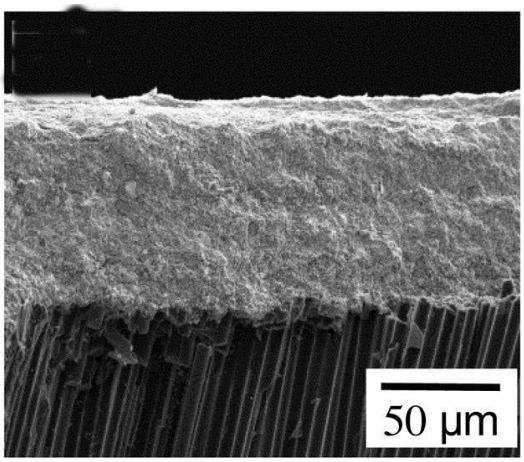

Figure 1-5. Cross-sectional image of a HfC coating obtained by CVD [22].

(3) Plasma spray

Plasma spray technology is a simple way to prepare refractory coatings with high melting points. Diverse materials, such as metal and ceramics, can be applied as the spray materials, as shown in Figure 1-6. Material in the form of powder is injected into a very high temperature plasma flame, where it is rapidly heated and accelerated to a high velocity. The hot material impacts on the substrate surface and rapidly cools forming a coating. However,

various defects, such as high porosity, poor bonding strength, high surface roughness and lamellar stacking characteristics, could also form. So subsequent processing needs to be performed to eliminate the above defects.

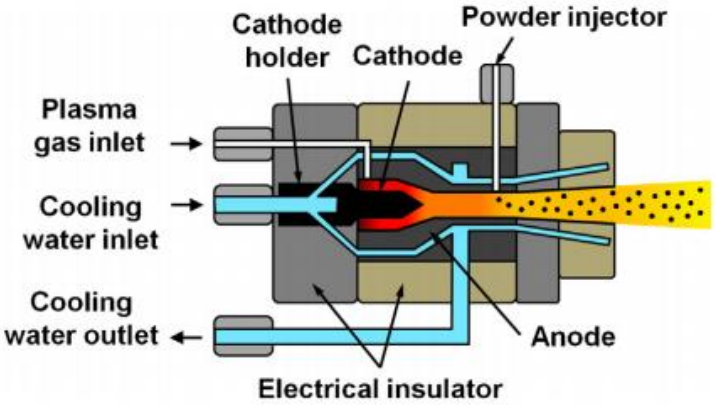

Figure 1-6. Schematic of a plasma spray process [23].

1.4 Matrix modification

Another promising approach is to modify C/C composites with UHTCs or Si-based ceramics. Instead of fabricating the protective coating on the surface of C/C, the aim of matrix modification is to introduce the ceramics into the C/C matrix, which could couple the excellent oxidation/ablation resistance of UHTCs or Si-based ceramics with the good fracture toughness of C/C [24, 25]. Processing methods have been carried out on the fabrication of C/C-UHTCs, such as chemical liquid-vapor deposition [26], chemical vapor infiltration [27], precursor infiltration and pyrolysis [28], carbo-thermal reduction reaction [14], slurry infiltration [24, 29, 30], hot pressing [31], microwave hydrothermal [32] and reactive melt infiltration [33]. In addition, two or more methods (see above) are often combined to facilitate the preparation of the modified C/C composites. Among these preparation methods, chemical vapor infiltration, precursor infiltration and pyrolysis, reactive melt infiltration and slurry infiltration are often used, which are described as follow.

(1) Chemical vapor infiltration (CVI)

This process involves complex physico-chemical phenomena, such as the transport of precursors, carriers, and by-product gases in the reactor [34]. The prepared composite possesses well-controlled composition and microstructure, good mechanical and anti-ablation properties. By using $TaCl_5$-CH_4-H_2-Ar, $HfCl_4$-$TaCl_5$-CH_4-H_2-Ar and $HfCl_4$-$TaCl_4$-CH_4-H_2-Ar as the gas sources, C/HfC, C/TaC and C/HfC/TaC composites were fabricated [27]. Although this method could prepare high-quality materials, it is expensive and time-consuming.

(2) Precursor infiltration and pyrolysis

Precursor infiltration and pyrolysis (PIP) is the method used in the preparation of ceramic matrix composites, which comprises an infiltration of a low viscosity polymer into the fiber preforms followed by pyrolysis: heating the polymer precursor in the absence of oxygen when it decomposes and converts into a ceramic. It could introduce variable kinds of ceramics and benefit for achieving near net shape manufacturing. Based on this method, C/C-HfC [35], C/C-ZrB_2-SiC [36] and C/C-ZrC-SiC [37] were successfully prepared. The major disadvantage of PIP is time-consuming, and that matrix is easy to shrink during pyrolysis, which may result in formation of cracks and pores.

(3) Reactive melt infiltration

Reactive melt infiltration (RMI) is used to introduce carbide or boride ceramics into composites through the reaction between molten metal mixtures and C/C composites. With respect to CVI and PIP, it is a cost-effective and time-saving method. For example, Wang et al. used $Si_{0.87}Zr_{0.13}$ alloy as the raw material. When heat-treated at high temperatures, the molten $Si_{0.87}Zr_{0.13}$ alloy was infiltrated into the C/C to form C/C–SiC–ZrC composites [38]. But the inevitable reactions between the molten mixture and carbon fibers resulted in the mechanical property degradation.

(4) Slurry infiltration

In slurry infiltration (SI), the precursor is a slurry which could infiltrate into fiber preforms. It is also convenient to introduce different ceramics into C/C according to requirements. Sun et al. used this method to introduce $ZrSiO_4$ into C/C [39]. However, the agglomeration of ceramics particles usually blocks the `pores of fiber preforms and then makes it more difficult for the subsequent densification.

1.5 Purpose of this study

As discussed above, coating technology and matrix modification are the two efficient methods to enhance the oxidation and ablation performances of C/C. They are also the focuses of our work. The novelty of our study is described as follow and compared to the reported literature.

For the coating technology, up to now, many different types of protective coatings, such as Si-Mo-Cr [40], mullite/SiC [10], $AlPO_4$/SiC [41], BN/SiC/Si_3N_4-ZrO_2-SiO_2 [42], ZrB_2-SiC/SiC [43], have been developed. However, the CTE (coefficient of thermal expansion) mismatch (see Table 1-1) between the coating and C/C substrate easily results in the

generation of cracks during high-low temperature cycles, which would provide the entrance channels for oxygen [44]. Evans et al. [45] have discussed the interface degradation mechanism, indicating that the large CTE difference will lead to the increase of internal stress, resulting in the degradation. As a result, the CTE mismatch is the key factor that results in the coating performance degradation.

To relieve the CTE mismatch between the coating and substrate, many attempts have been performed. The introduction of a second phase into the coating is the most widely adopted strategy to tackle this problem so as to improve the toughness of the coating considerably, where carbon nanotubes (CNTs) and SiC nanowires have been used [46, 47]. The introduction of a second phase proves to be ineffective for the improvement of the coating/substrate interface. Feng et al. [48] use low-density C/C composites (1.2 g/cm^3) to make use of their porous structures, which could provide the diffusion paths to the coating raw materials and then contribute to the increase coating/substrate interfaces. These interfaces could promote the oxidation performance of the produced coating. However, to ensure the thermal-structural components with favorable mechanical performances, C/C composites with enough density (>1.7 g/cm^3) and low porosity are required. Thus, this method is difficult to adopt in practical applications. In light of this problem, as an alternative method, pre-oxidation treatment of C/C was developed to construct a preferential interlocking transition coating/substrate interface [49]. The results showed that the oxidation treated region of C/C composites was difficult to control, and the treatment time was relatively longer, resulting in the inevitable damage of the mechanical performance of C/C [50].

As a result, finding a simpler, faster and more efficient way to construct an interlocking coating/substrate interface on high-density C/C (in the premise of minimum mechanical property loss) is becoming particularly important. So, in this study, blasting treatment of C/C is proposed. In addition, in actual environment, a non-destructive method is very important for the coating structure characterization and its service reliability evaluation. So in this thesis, Kossel interferences of proton-induced X-ray emission combined with X-ray reflectivity measurement, as a novel characterization method, is developed.

For the matrix modification, based on the above fabrication methods (discussed in section 1.4), a series of composites, such as C/C-HfC [35], C/C-ZrC-ZrB_2-SiC [36], C/C-ZrC-SiC [51-53], and C/C-ZrB_2-SiC [54], have been successively developed. It is evident that although a considerable amount of studies have been performed on the development of C/C-UHTCs composites, much of them are focused on HfC and Zr-based ceramics, with little consideration of HfB_2 [55]. HfB_2 as one of the family of UHTCs, also possesses high melting

point (3250°C) and good oxidation/ablation resistance [56]. When the boron oxide layer (the oxidation product of HfB_2) is sufficiently fluid, it could also cover the surface and act as an efficient barrier to restrict the inward diffusion of oxygen. HfB_2 is thus a promising candidate to improve the ablation properties of C/C composites.

A. Paul et al. fabricated C/C-HfB_2 by slurry infiltration [24, 29, 30]. However, the agglomeration of the HfB_2 particles easily blocked the pores in the outer layer of the C/C preforms and then made it difficult for the successive densification. To ensure the service reliability of C/C-HfB_2 composites, it is of great significance to resolve the problem of agglomeration and find out the valid dispersion method of HfB_2. So in this study, PIP is adopted to introduce HfB_2 into C/C matrix. Compared with slurry infiltration, this method possesses a larger infiltration depth, which can be expected to improve the uniformity of HfB_2 and realize the net shape manufacturing.

According to the discussion above, the main contents of the PhD work are listed as follow:

(1) Effect of blasting treatment of the C/C composites on microstructure, adhesive strength, oxidation/ablation performance of the ceramic coating (chapter 3).

(2) C/C blasting treatment combined with a second phase introduction to enhance the oxidation/ablation performances of the ceramic coating (chapters 3 and 4).

(3) Feasibility of Kossel interferences of proton-induced X-ray emissions combined with X-ray reflectivity, as a novel non-destructive characterization method, where X-ray planar waveguides are designed (chapter 5).

(4) Preparation of HfB_2 and HfB_2-SiC modified C/C composites. Effect of HfB_2 and HfB_2-SiC on the oxidation/ablation performances of C/C composites are studied (chapter 6).

Chapter 2: Experimental methods

In this chapter, we will give a detailed description of the raw materials, fabrication apparatus and characterization methods used in this thesis.

2.1 Carbon/carbon composites

2D carbon fiber felt was used as the reinforcement for C/C composites, as shown in Figure 2-1. The preform is made up of 90° weftless ply, short-cut fibre web and 0° weftless ply (see Figure 2-1 (a)). They are alternatively stacked with a needle punching technique (Figure 2-1 (b-c)). The fiber volume content of the preform is about 20–25%. C/C composites are prepared through the densification of the carbon fiber preform by thermal gradient chemical vapor infiltration (TCVI). During this process, CH_4 is used as the precursor with a flow rate of 4-8 L/min. The deposition time, temperature and pressure were 100-120 h, 1050-1150^{o}C and 5-10 kPa, respectively. The final density of the C/C composites was about 1.69-1.75g/cm^3. Morphology and phase composition of the C/C are shown in Figure 2-2. They consist of a single carbon element (Figure 2-2 (b)), and carbon fiber is surrounded by pyrolytic carbon matrix (Figure 2-2 (a)).

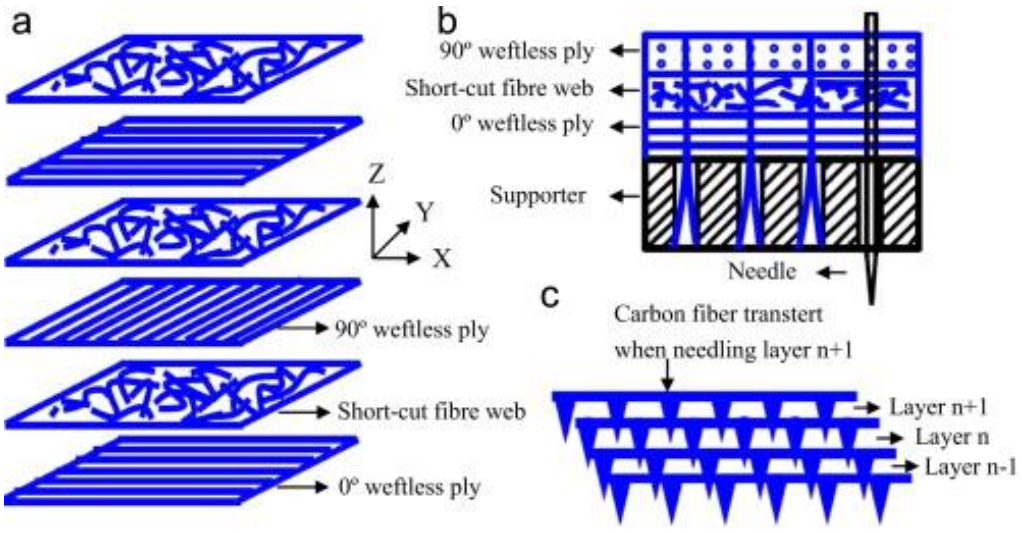

Figure 2-1. Schematic illustration of needled integral felts including a needling process: (a) position of weftless ply and short-cut fibre web; (b) detailed view of a Z-fibre bundle generated during the needling process; and (c) needling process [57].

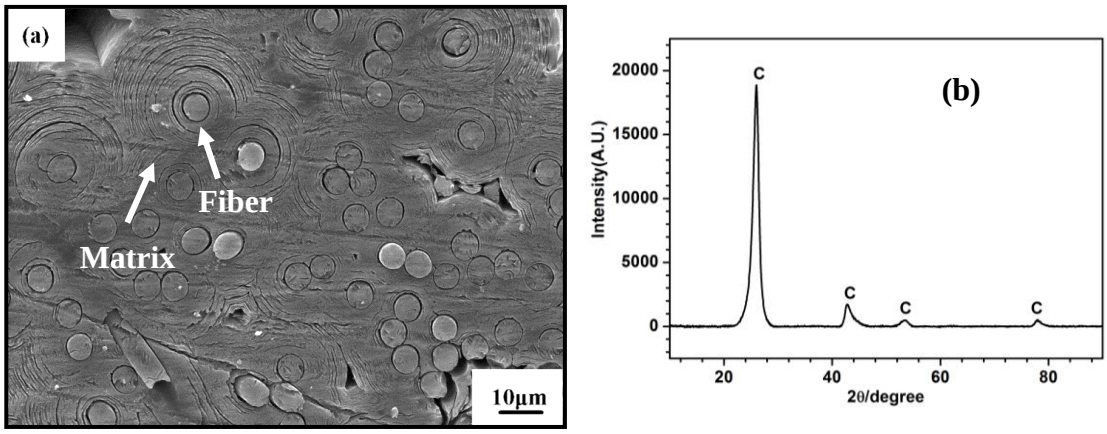

Figure 2-2. Microstructure (a) and phase composition (b) of the C/C composites.

2.2 Experimental apparatus

The experimental apparatuses, including the coating/film preparation and sample analysis, are listed as follow.

(1) High-temperature heat treated furnace: the maximum temperature is 2300 °C.
(2) Cutting machine: MODEL150.
(3) Ball mill: PM-4L, rotation speed <600 rpm.
(4) Supersonic cleaner: KQ-100A.
(5) Drying oven: 101A-2, the maximum temperature is 200 °C.
(6) Analytical balance: TG328B, accuracy ±0.0001 g.
(7) Universal mechanical test machine: CMT5304-30 kN.
(8) Thermal expansion test: DIL402C and DIL402E Dilatometer.
(9) Infrared radiation thermometer: Raytek MR1SCSF, accuracy of 0.75%.
(10) X-ray diffraction (XRD): Philips X'Pert MPD diffractometer.
(11) Thermal analysis: Mettler Toledo Star TGA/SDTA 851.
(12) Confocal laser scanning microscope : C130, Lasertec Corp., Yokohama, Japan.
(13) Scanning electron microscopy (SEM): VEGA 755136XM.
(14) Thermal cycling and ablation test: OA-Ⅲ oxyacetylene ablation machine.
(15) Film deposition: magnetron sputtering.
(16) Système d'Analyse par Faisceaux d'Ions Rapides (analysis system with high speed ion beams) platform in Sorbonne University.
(17) ANDOR iKon-M energy dispersive CCD camera.

2.3 Sample fabrication

2.3.1 Blasting treatment of C/C composites to construct a porous surface

Cylinder specimens (Ø10 mm × 10 mm) used as substrates were cut from the prepared C/C composites (described in section 2.1). They were hand-abraded with 100 and 400 grit SiC papers in turn, then cleaned ultrasonically with ethanol and dried at about 80°C for 2 h. A porous surface of C/C was achieved rapidly through blasting treatment using oxyacetylene torch. The flame was vertical to the C/C, as shown in Figure 2-3. In our study, C/C was treated in three different heat fluxes (2.38, 3.2 and 4.18 MW/m^2) [58]. The parameters are listed in Table 2-1. During blasting treatment, the gas pressures of O_2 and C_2H_2 were kept constant, and the heat flux of the oxyacetylene torch was adjusted through changing the flow ratio of O_2 and C_2H_2. The treatment time was 20-30 s.

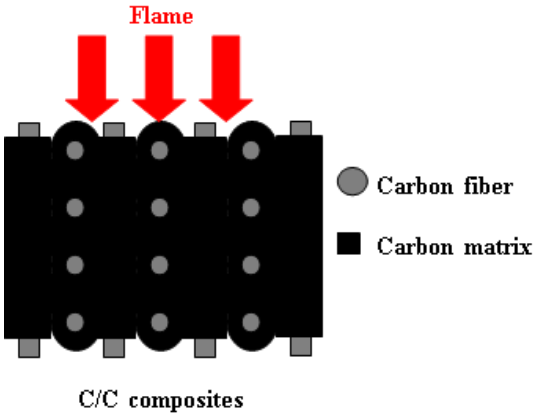

Figure 2-3. Schematic illustration of blasting treatment of C/C using oxyacetylene torch.

Table 2-1. Blasting treatment parameters of the oxyacetylene torch [58].

C_2H_2 (m^3/h)	O_2 (m^3/h)	Heat fluxes (MW/m^2)
0.65	0.88	2.38
0.83	1.12	3.20
1.12	1.51	4.18

2.3.2 Coating preparation on blasting-treated C/C composites

(1) SiC coating

To investigate the effect of blasting treatment, SiC coating was prepared on the treated C/C (obtained in section 2.3.1) by pressure-less reaction sintering. Powder compositions were as follows: 65-80 wt.% Si (300 mesh), 10-25 wt.% graphite (325 mesh) and 5-15 wt.% Al_2O_3 (300 mesh). The role of Al_2O_3 was used to increase the rate of diffusing reaction at high temperature. The powders were mixed together in an agate vial and stirred for 8 h in a ball mill (PM-4L) with the speed of 500 rpm. Then the mixed powders and the treated C/C

specimens were put in a graphite crucible and heated to 1750-2100°C and held at that temperature for 1-3 h in argon atmosphere.

(2) Si-Mo-Cr coating

Figure 2-4 shows the process of blasting treatment and preparation of Si-Mo-Cr coating. Firstly, blasting treatment of C/C composites was conducted (described in section 2.3.1). Then, Si-Mo-Cr coating was prepared by pressure-less reactive sintering. Powder compositions were as follows: 45-60 wt.% Si (300 mesh), 25-30 wt.% $MoSi_2$ (200 mesh), 5-15 wt.% Cr (200 mesh) and 8-15 wt.% graphite (200 mesh). The powder mixtures and C/C specimens were mixed together and in turn put in a graphite crucible, and then heat treated at 1750-2100°C for 1-3 h in argon atmosphere.

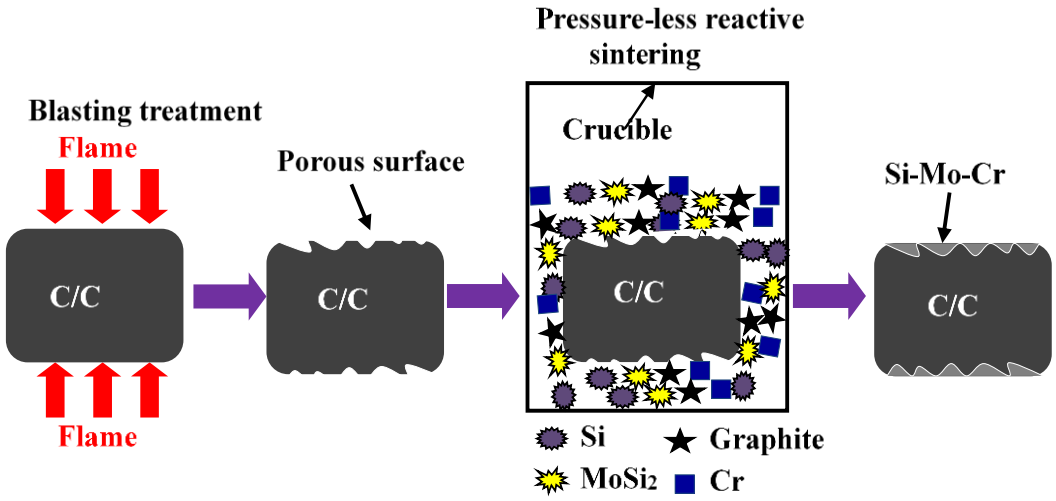

Figure 2-4. Schematic illustration of blasting treatment of C/C and preparation of the Si-Mo-Cr coating.

(3) SiC nanowires toughened Si-Mo-Cr coating

Figure 2-5 shows the schematic illustration of blasting treatment of C/C, in situ grown SiC nanowires and preparation of Si-Mo-Cr coating. It was divided into three steps. The first step was to construct a porous surface on C/C via blasting treatment (details are in section 2.3.1). In the second step, in situ growth of SiC nanowires was prepared on the surface of the treated C/C composites by chemical vapor deposition (CVD). Mixed powders of SiO_2, Si and graphite were placed on the bottom of a crucible. Then, the treated C/C composites were placed above the mixed powders and heat treated in an argon atmosphere to form the SiC nanowires. Finally, Si-Mo-Cr coating was prepared by pressure-less reactive sintering (see in Figure 2-4).

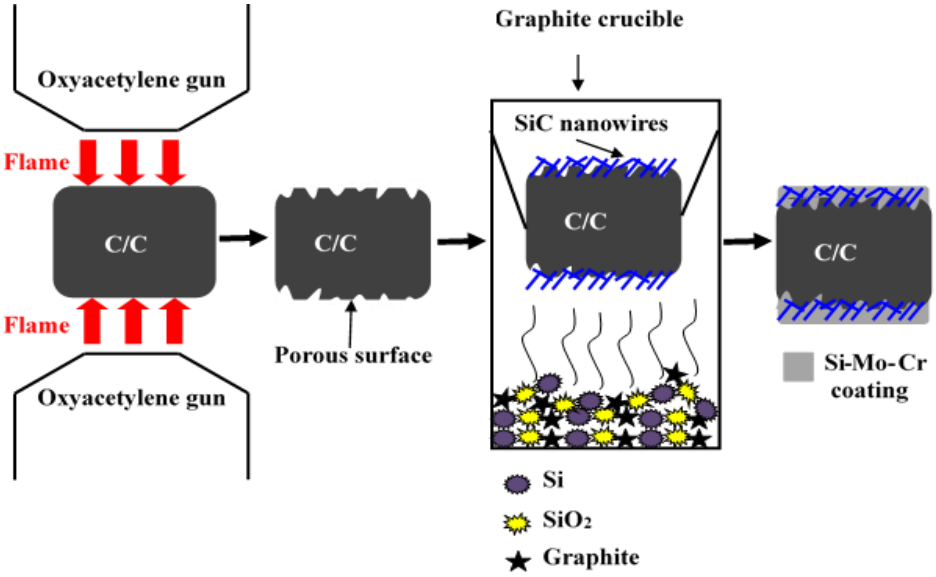

Figure 2-5. Schematic illustration of C/C blasting treatment, in situ grown SiC nanowires and preparation of Si-Mo-Cr coating.

(4) HfC-SiC coating

The procedure of constructing the porous surface on C/C composites and the preparation of HfC-SiC coating is shown in Figure 2-6.

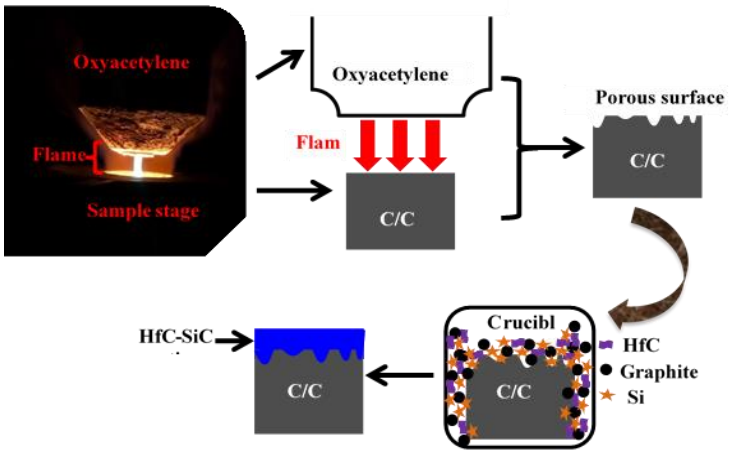

Figure 2-6. Schematic illustration of C/C blasting treatment and the preparation of HfC-SiC coating.

In the first step, a porous surface was constructed on C/C. Then the HfC-SiC coating was prepared on the pre-treated C/C composites by pressure-less reactive sintering. Powder compositions for pressure-less reactive sintering were as follows: 45-65 wt.% Si (300 mesh), 10-15 wt.% HfC (400 mesh) and 8-30 wt.% graphite (300 mesh). The powders were mixed uniformly in an agate vial after being stirred for 12 h in PM-4L ball mill with a speed of 500

rpm. Then, the obtained powder mixtures and the pre-treated C/C specimens were put in a graphite crucible, which were heated to 1800-2300ºC and held for 1-4 h in an argon atmosphere.

(5) ZrB_2-SiC coating

The procedure of constructing the porous surface on C/C and the preparation of ZrB_2-SiC coating is shown in Figure 2-7. The process is the same as that of HfC-SiC coating. ZrB_2-SiC coating was prepared on the pre-treated C/C composites by pressure-less reactive sintering. Powder composition was as follow: 45-65 wt.% Si (300 mesh), 10-15 wt.% ZrB_2 (300 mesh) and 8-30 wt.% graphite (300 mesh).

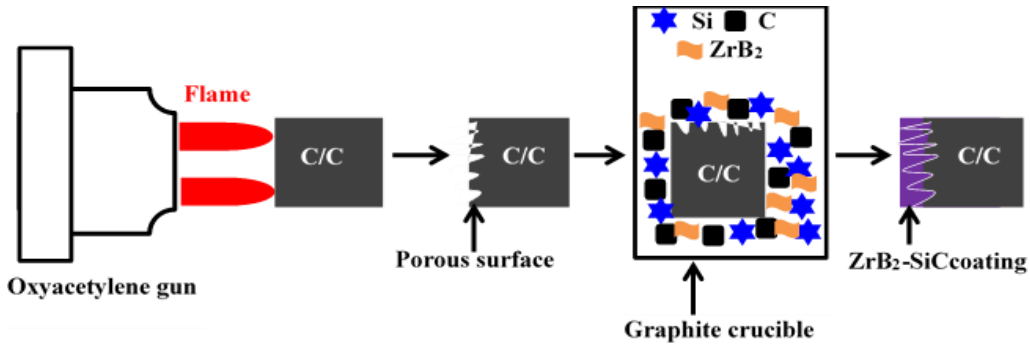

Figure 2-7. Schematic diagram of C/C blasting treatment and introducing ZrB_2 into SiC coating by pressure-less reactive sintering.

2.3.3 Thin film waveguides preparation on Si substrate

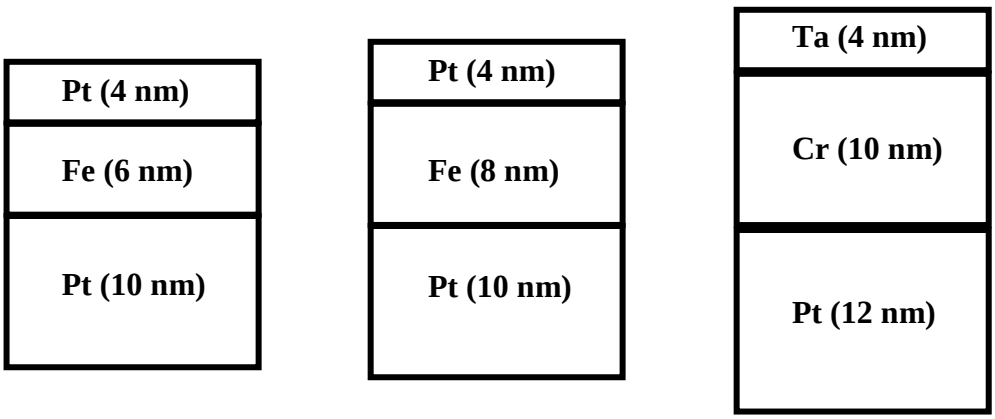

Figure 2-8. Schematic diagram of the designed waveguides.

Three thin films waveguides were designed: Pt(4 nm)/Fe(6 nm)/Pt(10 nm)/Si, Pt(4 nm)/Fe(8 nm)/Pt(10 nm)/Si and Ta(4 nm)/Cr(10 nm)/Pt(12 nm)/Si, as shown in Figure 2-8. The designed thin films were deposited at room temperature on a Si (100) substrate by

magnetron sputtering, as shown in Figure 2-9. The power applied on the sputtering targets was 10 W, the base pressure was 10^{-8} mbar, and the sputtering gas was argon at the working pressure of 5×10^{-2} mbar. The sputtering rates of Pt, Fe, Cr and Ta were 0.066, 0.024, 0.024 and 0.035 nm/s, respectively, as measured by a quartz microbalance.

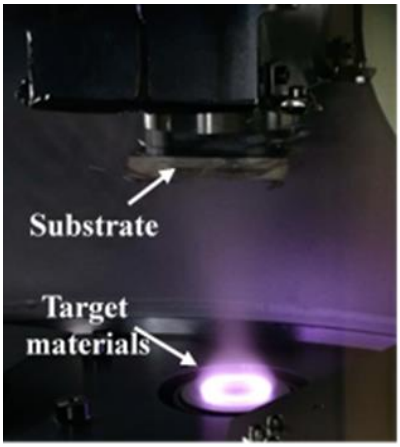

Figure 2-9. Experimental setup of the magnetron sputtering.

2.3.4 HfB_2 and HfB_2-SiC modified C/C composites

(1) Preparation of C/C-HfB_2 composites

Precursor infiltration and pyrolysis (PIP) is a common method to introduce ceramics into C/C preforms. It usually consists of two processes: infiltration of a low viscosity precursor and pyrolysis at high temperature. In our study, C/C-HfB_2 was prepared by PIP, as shown in Figure 2-10. In the first step, the carbon fiber felt (described in section 2.1) was densified to 1.0-1.1 g/cm^3 by isothermal chemical vapor infiltration (ICVI) process. The ICVI temperature and time were set at 1000-1150°C and 30-40 h, respectively. Then HfB_2 was introduced into C/C composites by PIP. Details of PIP are given in Figure 2-11. A solution of organic hafnium boride polymer and xylene was used as the precursor. The obtained low-density C/C composites in the first step were put in an airtight container. The container was evacuated (pressure lower than 6 kPa). Because of the pressure difference inside and outside of the container, the liquid precursor was inhaled and immersed the prepared C/C samples for 1-2 h. Then the samples were dried at 90 -100°C in air for 24 h. After that, the samples were put in a graphite crucible and held at 1500-1800^{o}C for 1-4 h in argon atmosphere (shown in Figure 2-10). The above process was repeated until the density increased to 1.3-1.4 g/cm^3. After that, the obtained samples were further densified by pyrolysis carbon through TCVI. During this process, CH_4 was used as the carbon source. Finally, the prepared composites were graphitized at 2100-2300^{o}C for 2 h in argon atmosphere. The density of the prepared C/C-

HfB_2 composites was about 1.77-1.84 g/cm^3.

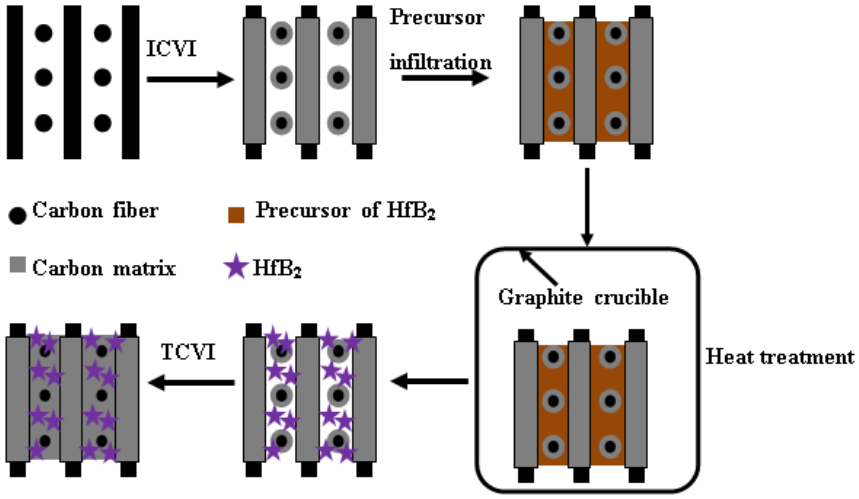

Figure 2-10. Schematic illustration of the preparation of C/C-HfB_2 composites.

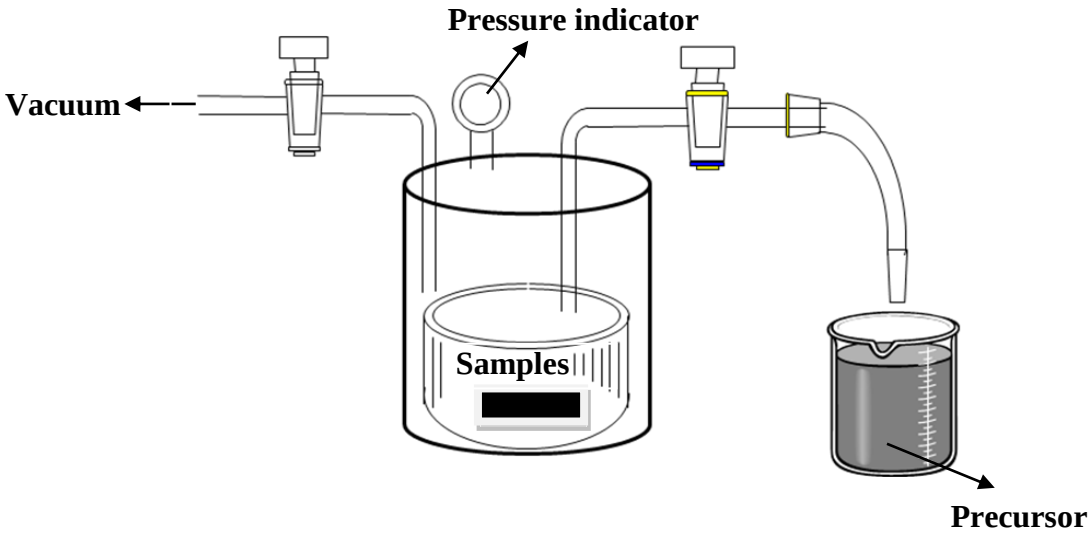

Figure 2-11. Schematic of the vacuum infiltration device [39].

(2) Preparation of C/C-HfB_2-SiC composites

The preparation process of C/C-HfB_2-SiC composites is similar to that of C/C-HfB_2. The main difference is the sample shape and the PIP precursor. In the first step, the carbon fiber felt (described in section 2.1) was densified to 1.0-1.1 g/cm^3 by ICVI. Then the composites were machined into nose shape to simulate the thermal-structural components used in actual environment, as is shown in Figure 2-12 (a-b). The nose-shaped sample is made up of two parts: a hemisphere (the radius is 8 mm) and a cylinder (the diameter is 12 mm and the height is 6 mm). Then a mixed solution of organic hafnium boride polymer and polycarbosilane was

prepared, which was dispersed in dimethylbenzene with a weight ratio of 1:1. The solution was used as the precursor to introduce HfB_2-SiC into C/C. The final density of the composites was 1.94-2.03 g/cm^3 after ten PIP cycles.

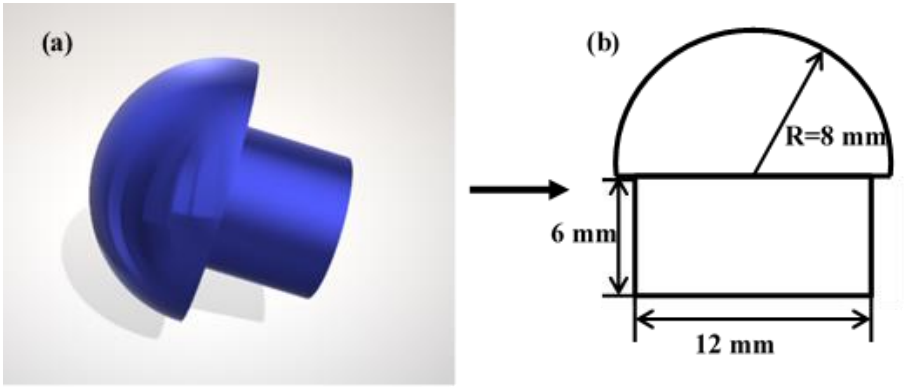

Figure 2-12. Schematic diagram of the prepared nose-shaped C/C-HfB_2-SiC composite (a) and the corresponding dimensions (b).

2.4 Characterization

2.4.1 Ablation test

(1) Single ablation test

Ablation behavior was investigated using oxyacetylene torch. The experiment setup consisted of oxygen and acetylene tanks, an oxyacetylene gun, a control cabinet and a sample stage. The inner diameter of the oxyacetylene gun tip was 2 mm, and the corresponding distance to the sample was 10 mm. Two different heat fluxes (2.38 and 4.18 MW/m^2) were used. Detailed parameters of the heat flux were described in section 2.3.1. During ablation, surface temperature was measured by a two-color pyrometer (Raytek MR1SCSF, accuracy of 0.75%). The linear and mass ablation rates of the specimens were obtained according to the formula (2-1) and (2-2)

$$R_l = \frac{\Delta d}{t} = \frac{d_1 - d_2}{t} \qquad (2\text{-}1)$$

$$R_m = \frac{\Delta m}{t} = \frac{m_1 - m_2}{t} \qquad (2\text{-}2)$$

where R_l is the linear ablation rate; d_1, d_2 are the thickness of the sample center before and after ablation; R_m is the mass ablation rate; m_1, m_2 are the sample mass before and after ablation; t is the ablation time. The final ablation value is the average of the measurements over three specimens.

(2) Cyclic ablation test

Cyclic ablation was conducted using vertical and parallel oxyacetylene torch, as shown in Figures 2-13 and 2-14. Surface temperature of the sample was measured by the Raytek MR1SCSF thermometer. In our study, two cyclic ablation tests (1600^{o}C to room temperature and 1750^{o}C to room temperature) were performed. Gas fluxes of O_2 and C_2H_2 were 0.88 and 0.65 m^3/h. The ablation temperature was controlled through the adjustment of the distance between the oxyacetylene torch and the sample.

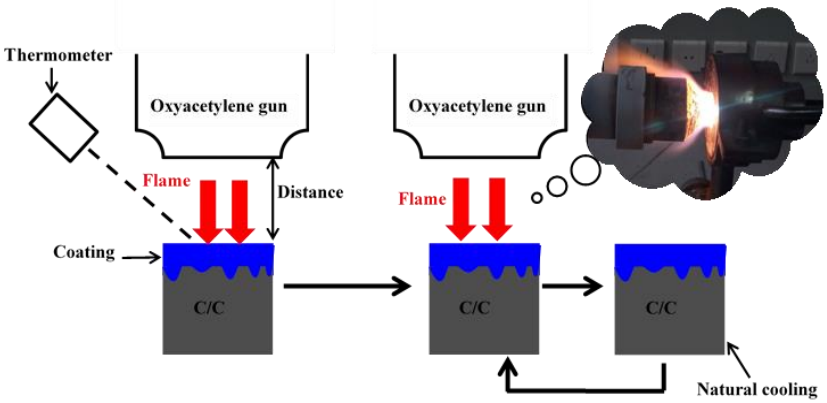

Figure 2-13. Schematic illustration of cyclic ablation test using vertical oxyacetylene torch.

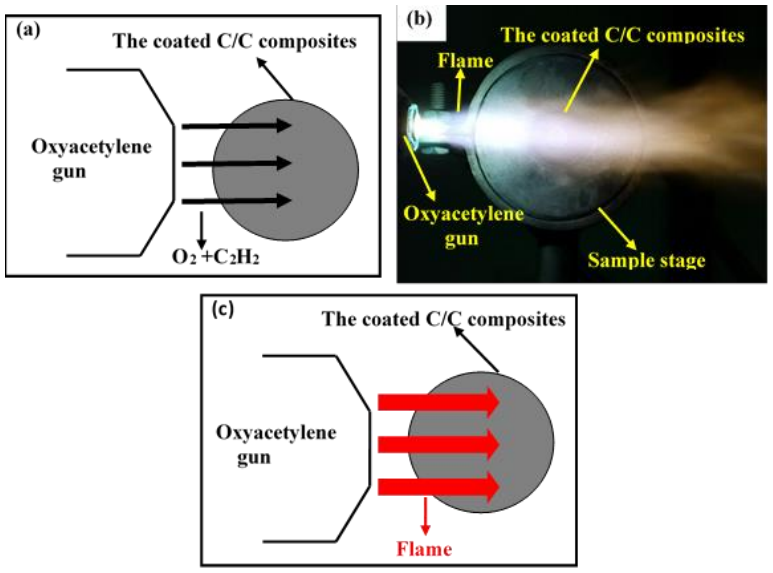

Figure 2-14. The cyclic ablation test using parallel oxyacetylene torch, (a) Schematic illustration of the experimental setup before test, (b) Experimental setup during test, (c) Schematic illustration of (b).

To better study the cyclic ablation performance of the coating, the mass loss per unit area in each thermal cycle was obtained according to the formula (2-3). Detailed descriptions of

the cyclic ablation test are as follow. Firstly, the mixture of O_2 and C_2H_2 was ignited, and then the distance between oxyacetylene gun and the sample was adjusted so as to make the surface temperature reaching 1600 or 1750°C. Then the cyclic ablation test was carried out. The ablation time in each cycle was set as 5, 10, 20 s according to the requirement. After that, the oxyacetylene flame went out, and the sample was cooled down naturally before the next thermal cycle.

$$\Delta W = \frac{m_0 - m_1}{A} \qquad (2\text{-}3)$$

where ΔW is the mass loss per unit area; m_0, m_1 are the sample mass before and after cyclic ablation test, respectively; A is the area of ablation surface. The final mass loss per unit area is the average of the measurements over three specimens.

2.4.2 Adhesive strength test

The adhesive strength between the coating and C/C was measured using adhesive method. A schematic of the test device is shown in Figure 2-15. Cylindrical stainless-steel rods are used as matching parts. Specimens are bonded with the end surface of matching parts by a modified acrylate adhesive. After being positioned for 10–15 min and solidified for 24 h at room temperature, the specimens are measured by a universal test machine (detail given in section 2.2), and the largest force of each specimen is recorded. The adhesive strength (σ) is calculated according to the following formula (2-4):

$$\sigma = \frac{F}{S} \qquad (2\text{-}4)$$

where F is the largest force recorded by the universal testing machine and S is the cross-sectional area of the coated specimens.

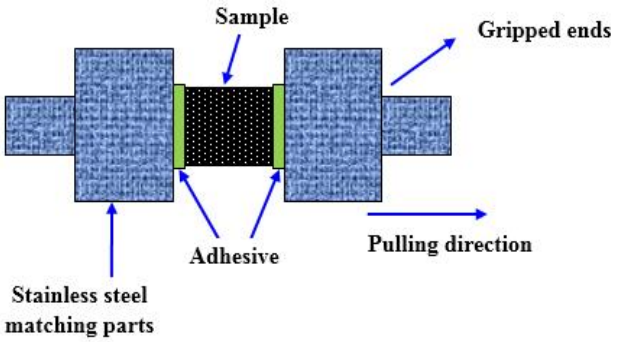

Figure 2-15. Schematic of the testing device used for the adhesive strength.

2.4.3 PIXE-Kossel experiment

The proton beam we work with is provided by the SAFIR (Système d'Analyse par Faisceaux d'Ions Rapides) platform of Sorbonne University in Paris, France. This research platform is based on a type AN-2000 electrostatic Van de Graaff particle accelerator associated with beamlines and experimental chambers. The principle of the accelerator is to impart kinetic energy to charged particles. The different ionizable gases (H, He, ...) are stored in the upper part of the accelerator. They are ionized by a radiofrequency field of the order of 100 MHz and then magnetically focused in the axis of the extraction channel. The accelerator is capable of generating ion beam of H^+, D^+, He^+, C^+, N^+, O^+ with a small divergence of 0.5 mrad and an energy up to 2.5 MeV. Spot size of the beam can be adjusted down to 1 mm^2. The plarform could carry out the following tests, Rutherford backscattering spectrometry (RBS), particle induced X-ray emission (PIXE), nuclear reaction analysis (NRA), elastic recoil detection analysis (ERDA) and particle channelization in single crystals. The schematic diagram of our PIXE-Kossel experiment is shown in Figure 2-16.

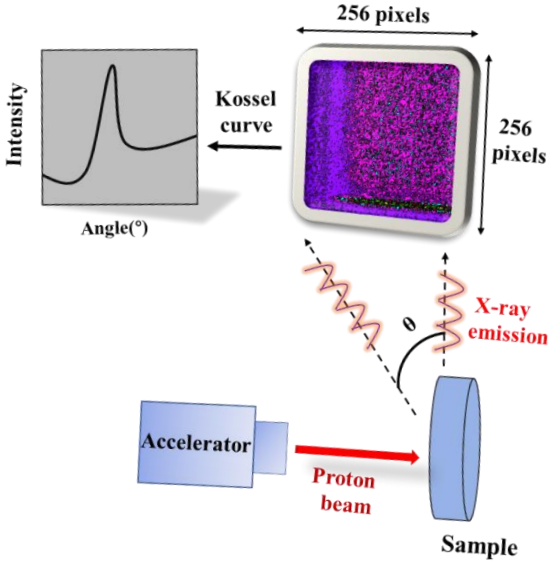

Figure 2-16. Scheme of the experimental setup for the PIXE-Kossel experiment.

A 1.6 MeV proton beam generated by the Van de Graaff accelerator of the SAFIR platform, was incident normal to the sample surface. An ANDOR iKon-M energy dispersive CCD camera equipped with a 1024×1024 sensor array and 13×13 μm pixels, was used to record the generated X-ray emissions. This CCD camera produces an x-ray spectrum for each of its pixels. Each column of pixels corresponds to a detection angle. To facilitate the data acquisition and subsequent data processing, a 4×4 binning is selected to obtain 256×256 pixel

images (as shown in Figure 2-16). The angular acceptance of the camera is 2.71°, as determined in [59]. As shown in Figure 2-16, when the proton beam irradiates the sample, we first obtain a picture on the CCD camera, where the intensity of a pixel depends on the total number of x-rays collected in this pixel. After the energy calibration of the spectrum, a region of interest (ROI) is selected around a characteristic line, to obtain a 256×256 filtered spectral image. Then, this image is integrated in the vertical direction so as to obtain a 256 channel scan, representing the intensity of the given line as a function of the detection angle (grazing exit angle θ), i.e. the Kossel curve.

2.4.4 X-ray reflectivity measurement

To know the actual thickness and roughness of the deposited stacks, X-ray reflectivity (XRR) measurement is conducted. XRR is widely employed to study thin films and multilayers. In this study, the XRR measurements were performed at the 0.1542 nm wavelength on a Rigaku five-circle diffractometer. Then with the help of the IMD software [60] and the optical constants of the CXRO [61], the measured XRR curves were fitted to determine the thickness, roughness and density of the various layers.

2.4.5 Microstructure and phase composition

The microstructures and morphologies of the samples are analyzed by scanning electron microscopy, equipped with energy dispersive spectrometry (EDS). The phases are analyzed by X-ray diffraction with a Cu Kα radiation (λ=0.1542 nm) from an x-ray tube operating at 40 kV and 35 mA. With the help of a confocal laser scanning microscope, the average surface roughness (Ra) of C/C before and after blasting operation was measured.

2.4.6 Thermophysical analysis

Thermogravimetric analysis was carried out in air condition by thermal analysis apparatus. Coefficient of thermal expansion (CTE) was measured by a dilatometer (see section 2.2).

Chapter 3: The effects of C/C blasting treatment

3.1 Introduction

A preferential interlocking transition layer is beneficial for relieving the CTE mismatch and enhancing the adhesive strength between the coating and the substrate [48, 49, 62]. In this chapter, to efficiently achieve a porous surface of C/C, blasting treatment using oxyacetylene torch is proposed. Because of its good physical and chemical adaptability with the C/C substrate [10, 41, 43, 63-65], SiC and Si-Mo-Cr coatings are then prepared on the surface of C/C to investigate the effect of blasting treatment.

3.2 Surface modification of C/C via blasting treatment

Details of the blasting treatment of C/C are described in chapter 2. In this section, for the convenience of discussion, C/C without pre-blasting treatment is marked as S-0, and C/C composites with blasting treatment in the heat fluxes of (2.38, 3.2 and 4.18 MW/m^2) are noted S-1, S-2 and S-3, respectively. Figure 3-1 presents the surface morphologies of C/C composites after blasting treatment, from which a distinct change is observed. On the surface of S-0 (Figure 3-1 (a)), no obvious interface gap is found between the carbon fiber and carbon matrix, and pyrolysis carbon surrounds the circle carbon fibers tightly. As for S-1 (shown in Figure 3-1 (b)), needle-like carbon fibers are observed, indicating the C/C substrate suffered obvious erosion. In addition, interface gaps could be found between carbon matrix and carbon fibers. During blasting treatment, oxidation took place preferentially at the fiber/matrix interface and the oxidizing gas diffused into the substrate gradually, resulting in the formation of needle-like fibers and interface gaps. Figure 3-1 (c) shows the surface morphologies of S-2. Compared with S-1 (Figure 3-1 (b)), needle-like feature of carbon fibers becomes more apparent, and the interface gaps between carbon fibers and carbon matrix grow wider and deeper. Compared with the surface morphology of S-1 and S-2 (Figure 3-1 (b-c)), the surface of S-3 suffers more serious erosion and only a little carbon fiber could be observed, indicating that most of the carbon fibers is consumed by the oxyacetylene torch (Figure 3-1 (d)). The interface gaps between carbon fibers and carbon matrix are further enlarged, resulting in the formation of micro-holes. In addition, debonding of the pyrolytic carbon (surrounded the carbon fiber) is also observed on the surface, which can be mainly attributed to the thermal conductivity difference of pyrolytic carbon in radial and axial direction. It has been reported

that the radial thermal conductivity of pyrolytic carbon (about 3.5-50 W/(m·K)) is much lower than that in the fiber axial direction (about 25.6–174W/(m·K)) [66]. The as-received coarse and porous structure (seen in Figure 3-1 (b-d)) is expected to provide diffusion paths for the coating materials to infiltrate into the C/C substrate and form an inlaid coating/substrate interface.

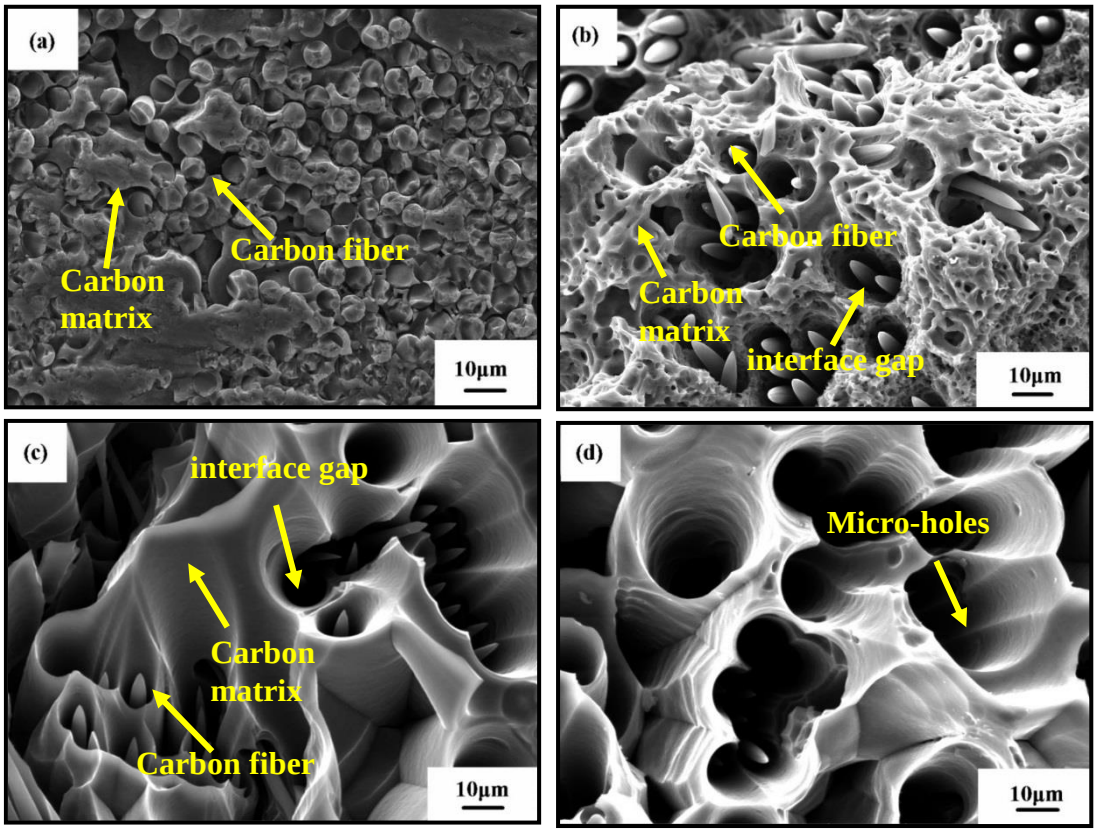

Figure 3-1. SEM micrograph of the C/C composites after blasting treatment in different heat fluxes using oxyacetylene torch: (a) S-0, (b) S-1, (c) S-2, (d) S-3.

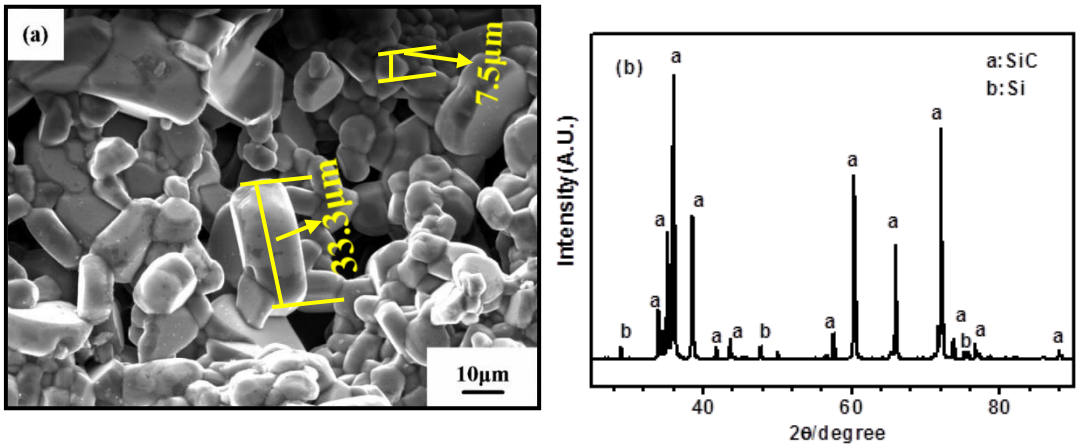

Figure 3-2. Typical surface morphology (a) and XRD pattern (b) of the prepared SiC coating by pressure-less reactive sintering.

SiC coating is then prepared on the treated C/C to study the effect of blasting treatment. Surface morphology and phase compositions of the as-prepared SiC coating are shown in Figure 3-2. As seen in Figure 3-2 (a), SiC shows different grain sizes. The main phases of the SiC coating are SiC and Si (see in Figure 3-2 (b)). During pressure-less reactive sintering, SiC is formed by the reaction of Si and C. To ensure the complete consumption of the C, an excess of Si is chosen. The content of Si and SiC could be adjusted through the ratio of Si and C in the powders [67]. As a result, a little amount of Si is detected (seen in Figure 3-2 (b)).

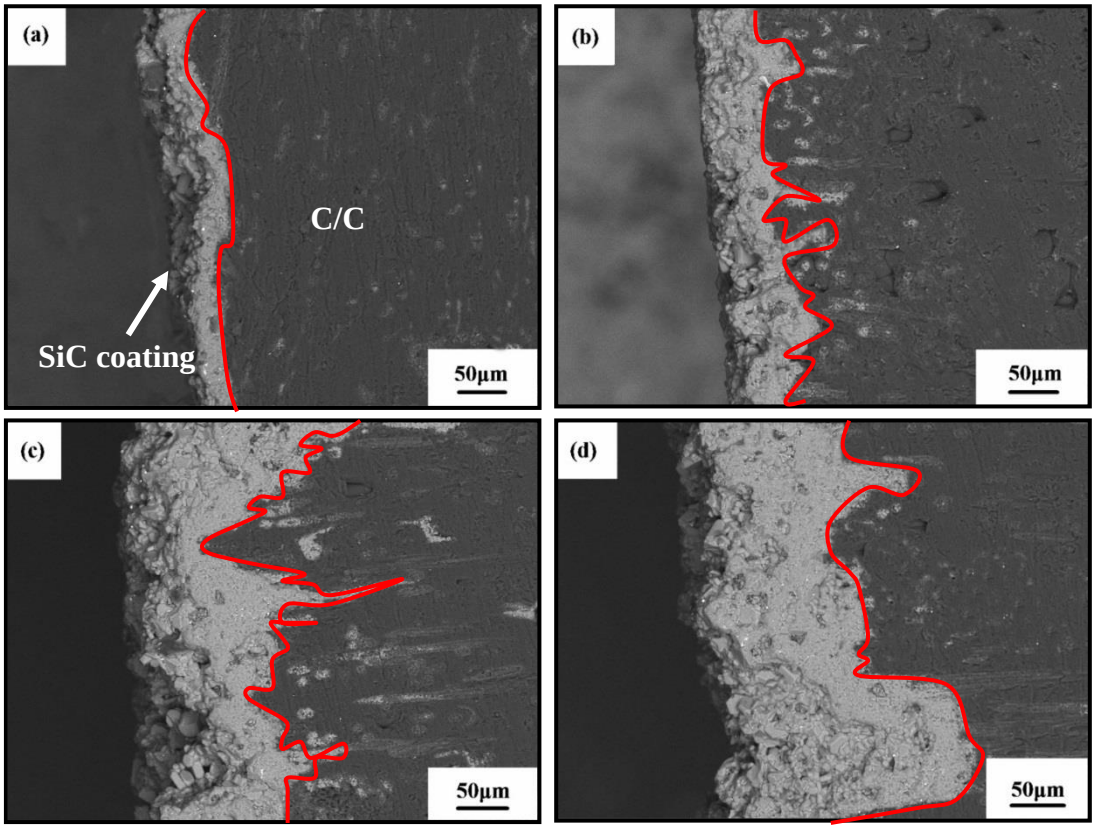

Figure 3-3. Cross-section micrograph of the SiC coated C/C with blasting treatment in different heat fluxes under the oxyacetylene torch: (a) S-0, (b) S-1, (c) S-2, (d) S-3.

Figure 3-3 shows the cross-section micrograph of the prepared SiC coating. The interfaces between SiC coating and C/C substrate are emphasized by a red line. From Figure 3-3, significant differences can be found at the coating/substrate interface, and the thickness of the as-received coatings ranges from 50 to about 210 μm. For the coated C/C without blasting treatment (Figure 3-3 (a)), a straight interface structure is formed, and only little amounts of coating materials are infiltrated into the C/C substrate with the coating thickness of 50 μm. Figure 3-3 (b-d) presents the interface structure of the SiC coating with blasting treatment. Compared with the interface structure of S-0 (Figure 3-3 (a)), an inlaid

coating/substrate interface is formed, indicating that the as-received porous and coarse surface (Figure 3-1 (b-d)) produced by blasting treatment is beneficial to form a transition layer. During pressure-less reactive sintering, the fiber/matrix interface gaps (Figure 3-1 (b-d)) provided the diffusion channels for the coating materials into C/C substrate. As for S-1 (Figure 3-3 (b)), it can be found that the amount of coating material infiltrating into the C/C substrate increases with the coating thickness of 80 μm. As for S-2 (Figure 3-3 (c)), the infiltration depth as well as the infiltration amount of coating materials increases, and the coating thickness reaches about 130 μm. With respect to the interface structure in Figure 3-3 (b), an obvious interlock interface is formed. As for S-3 (Figure 3-3 (d)), the infiltration amount of coating materials further increases, resulting in the coating thickness increasing to about 210 μm (Figure 3-3 (d)). The above results indicate that the formed micro-holes (Figure 3-1 (d)) produced by blasting treatment is filled with the coating materials through the flow of liquid Si during pressure-less reactive sintering.

Figure 3-4 reveals the adhesive strengths of the SiC coated C/C composites, from which it can be found that blasting treatment can improve the coating/substrate adhesive strength efficiently. Compared with the coated C/C without blasting treatment (S-0), the maximum adhesive strength is increased by about 43% (S-2).

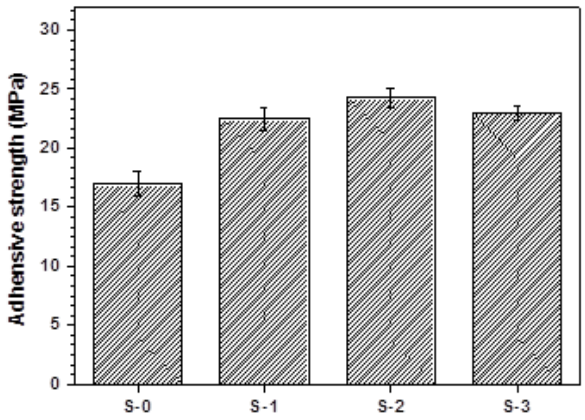

Figure 3-4. Adhesive strengths of the prepared SiC coating.

3.3 Blasting treatment on the cyclic ablation performance of Si-Mo-Cr coating

Owing to the formed protective glass layer of SiO_2 and Cr_2O_3 which possesses high resistance to volatilization and oxygen diffusion at high temperature, Si-Mo-Cr coating is proved to be a promising coating material [68, 69]. According to the results obtained in previous section, C/C is firstly blasting treated and then Si-Mo-Cr coating is prepared. Effect of blasting treatment on the cyclic ablation performance of Si-Mo-Cr coating is studied. For

the convenience of discussion, the Si-Mo-Cr coated C/C composites without and with blasting treatment are noted SMC-1 and SMC-2, respectively. Figure 3-5 shows the surface temperature curve of the sample in one thermal cycle. The ablation time in one cycle is set as 5 s. After that, the sample is cooled to room temperature and then tested again for the next cycle According to Figure 3-5, the ablation at 1600 °C is about 2 s. Each sample is tested for 25 cycles.

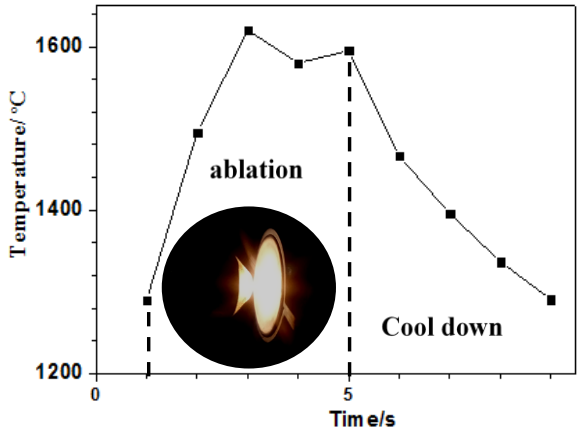

Figure 3-5. Typical surface temperature curve of the sample in one thermal cycle.

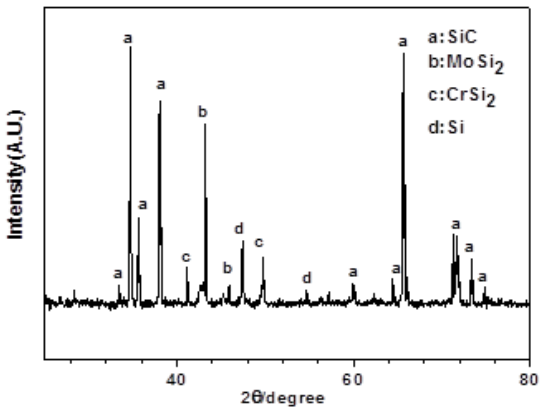

Figure 3-6. XRD pattern of the coating prepared by pressure-less reactive sintering.

Figure 3-6 shows the XRD pattern of the Si-Mo-Cr coating. The main phases are SiC, $MoSi_2$, $CrSi_2$ and Si. The backscattering micrograph of the coating is given in Figure 3-7. Three phases can be clearly observed. Combined the XRD pattern (Figure 3-6) and the EDS analysis (Figure 3-7 (c-e)), the obtained three phases can be distinguished as the mixture of $MoSi_2$ and $CrSi_2$ (noted as A), SiC (noted as B) and Si (noted as C) respectively. In addition, as seen in Figure 3-7 (a) and (b), micro-crack is found on the surface. When cooled from the preparation temperature to room temperature, the CTE mismatch between the coating and the

C/C substrate resulted in the formation of the micro-crack. Compared with that of SMC-1, the size of micro-crack of SMC-2 is obviously decreased, implying that blasting treatment has a positive effect on relieving the CTE mismatch between the coating and the C/C substrate. Cross-section micrographs of the coatings are shown in Figure 3-8. The coating/substrate interfaces are distinguished by a red line. For SMC-1, a straight interface is observed, and only a little coating material is infiltrated into the C/C substrate. In contrast, an interlock coating/substrate interface is found for SMC-2.

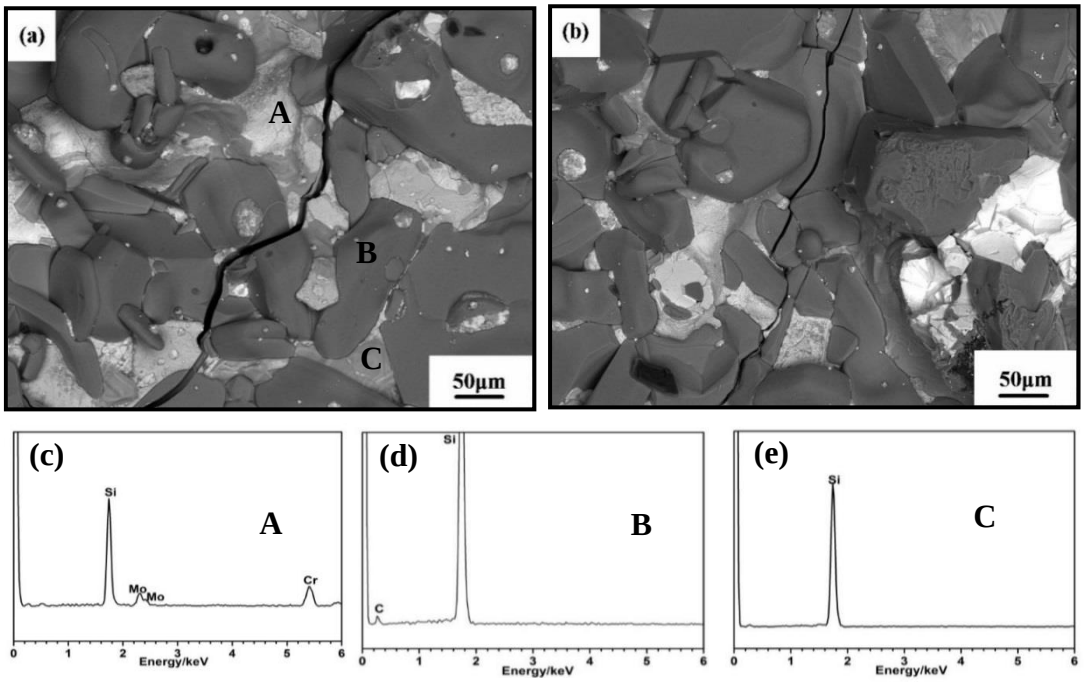

Figure 3-7. Backscattered electrons micrograph and the spot EDS analysis of the Si-Mo-Cr coating, (a) SMC-1, (b) SMC-2, (c) EDS of Spot A, (d) EDS of Spot B, (e) EDS of Spot C.

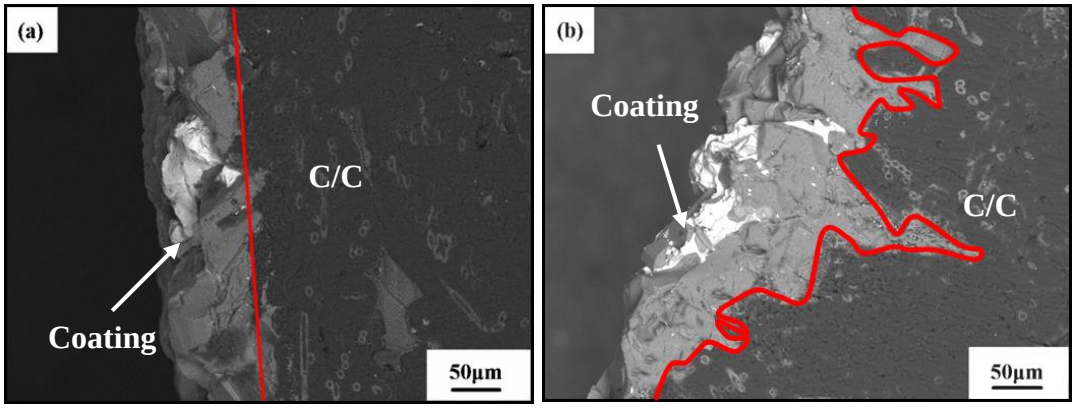

Figure 3-8. Cross-section micrographs of the Si-Mo-Cr coatings, (a) SMC-1, (b) SMC-2.

Figure 3-9 presents the adhesive strengths of the Si-Mo-Cr coating. With respect to SMC-1, the coating/substrate adhesive strength of SMC-2 is increased to about 26 MPa.

Figure 3-10 shows the XRD patterns of the Si-Mo-Cr coating after thermal cycling test. For SMC-2 (Figure 3-10 (b)), the phases are SiC, $MoSi_2$, SiO_2 and Cr_2O_3. As for SMC-1 (Figure 3-10 (a)), the diffraction peak of C is detected, indicating the debonding of the coating and the exposure of C/C substrate. Surface micrograph of the coated C/C after thermal cycling test is given in Figure 3-11. After thermal cycling test, a glassy layer is formed on the surface. Combined with the XRD pattern (Figure 3-10), it can be deduced that the received glassy layer is $SiO_2 + Cr_2O_3$, which is good for hindering the oxidized species from attacking the C/C substrate due to its low oxygen diffusion coefficient [68]. Some micro-cracks can be observed on the surface of SMC-2 (Figure 3-11 (b)). The micro-cracks are formed due to the thermal stress caused by the mismatch of CTE between the coating and the C/C during thermal cycling test. With respect to SMC-2, the $SiO_2 + Cr_2O_3$ glassy layer of SMC-1 is partially peeled off with the exposure of C/C substrates, where bare carbon fibers could be clearly observed (Figure 3-11 (a)).

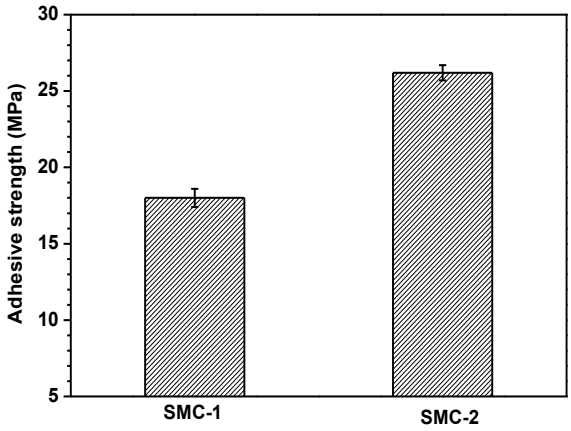

Figure 3-9. Adhesive strengths of the Si-Mo-Cr coated C/C composites.

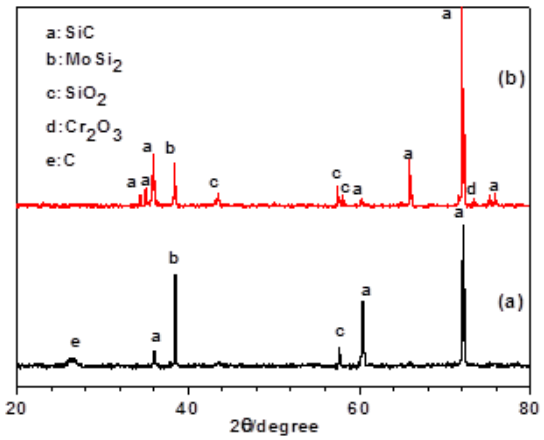

Figure 3-10. XRD pattern of the coating after thermal cycling test, (a) SMC-1, (b) SMC-2.

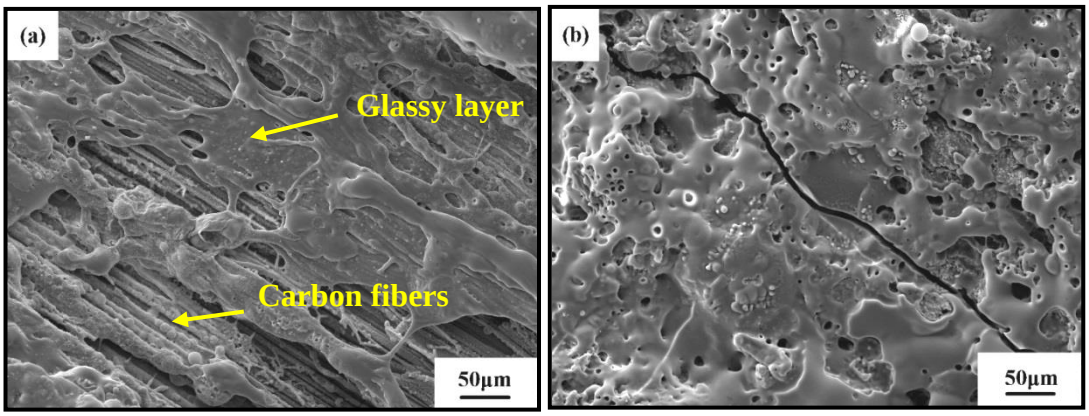

Figure 3-11. Surface morphology after cyclic ablation test, (a) SMC-1, (b) SMC-2.

CTE of bare C/C and the coated C/C composites are shown in Figure 3-12. Compared with the bare C/C composites, CTE of the coated C/C increases after applying the Si-Mo-Cr coating. In addition, it can also be seen that the CTE of SMC-2 is closer to that of bare C/C, indicating that the modified coating/substrate interface is beneficial for restricting the expansion of the coating materials as the temperature increases, thereby contributing to the CTE alleviation. This could explain why the size of surface micro-crack of SMC-2 is smaller than that of SMC-1 after the preparation of the Si-Mo-Cr coating (Figure 3-7). Combining the thermal cycling test results (Figure 3-11), the performance improvement of SMC-2 can be ascribed to the adhesive strength improvement and the CTE mismatch relief, thus improving its resistance to the erosion of the combustion gas.

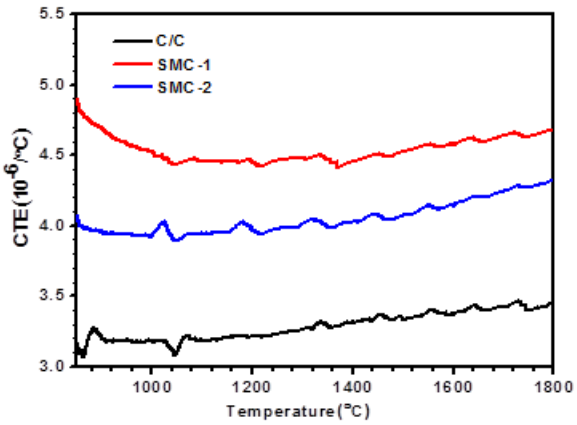

Figure 3-12. Coefficients of thermal expansion of the C/C and the Si-Mo-Cr coated C/C.

3.4 Blasting treatment combined with SiC nanowires to enhance the cyclic ablation performance of Si-Mo-Cr coating

In section 3.3, we find that although the construction of inlaid coating/substrate interface could improve the adhesive strength and thermal cycling performance of Si-Mo-Cr coating. But micro-cracks are still clearly observed on the coating after thermal cycling test. The introduction of a second phase into the Si-Mo-Cr coating is the mostly widely adopted strategy to tackle this problem so as to improve the toughness of the coating considerably. SiC nanowires are suitable to be used as the reinforcing materials due to their small size, high strength and toughness [70, 71]. In particular, SiC nanowires can impede the propagation of the micro-cracks, and then avoid the formation of penetration cracks [71]. In this section, coating/substrate interface modification and SiC nanowires introduction are combined to improve the performance of Si-Mo-Cr coating. In addition, to obtain a further understanding of the service reliability of the Si-Mo-Cr coating, the thermal cycling performance is studied using parallel oxyacetylene torch. For better comparison, in this section, the coated C/C composites with blasting treatment only are noted as SMC. The coated C/C composites with blasting treatment and in-situ grown SiC nanowires are noted as SMCnw.

3.4.1 Microstructure and cyclic ablation test

Figure 3-13 shows the surface morphology and XRD pattern of the as-prepared SiC nanowires. It is seen that SiC nanowires grow randomly and form a porous structure on the blasting treated C/C composites. From Figure 3-13 (b), C diffraction peak, corresponding to the C/C substrate, can be observed. The appearance of C peak further indicates that the prepared SiC nanowires layer is porous. During the preparation of the Si-Mo-Cr coating, the porous structure is beneficial for the diffusion of the coating materials into the C/C composites. The introduction of SiC nanowires is expected to improve the toughness of the coating, especially to decrease the occurrence tendency of micro-cracks. Figure 3-14 shows the surface morphology of the coating. Three phases (as seen in Figure 3-14 (b)) presenting white (A), dark grey (B) and grey (C) color can be distinguished as the mixture of $MoSi_2$ and $CrSi_2$, SiC and Si respectively (has been described in section 3.3). In addition, micro-crack is observed on the surface of the coating. However, it can be observed that the size of micro-crack of SMCnw is reduced significantly.

Figure 3-15 shows the cross-section micrograph of the coating. With respect to SMC, an inlaid coating/substrate interface is also obtained in SMCnw, further confirming that the coating materials could diffuse through the porous SiC porous layer (Figure 3-13).

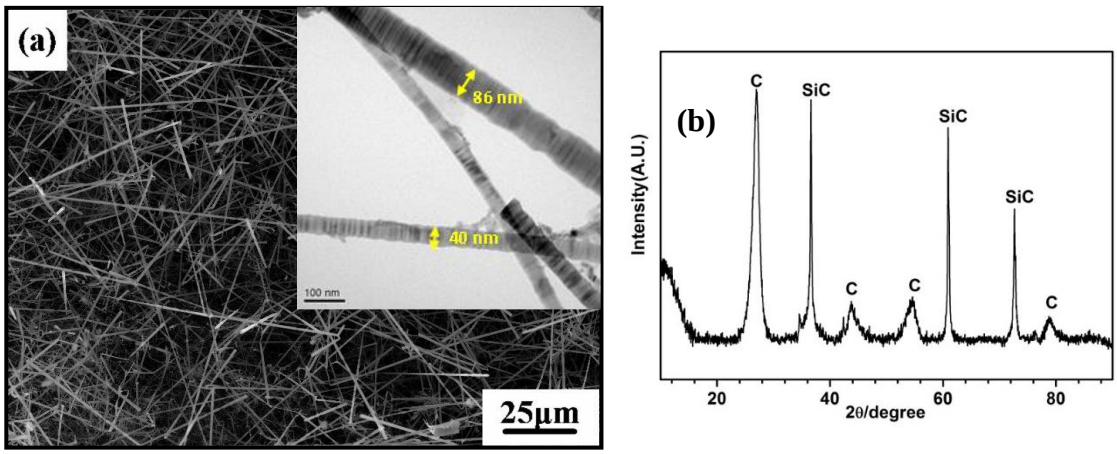

Figure 3-13. Surface morphology (a) and XRD pattern (b) of the SiC nanowires by CVD on the surface of the C/C composites with blasting treatment.

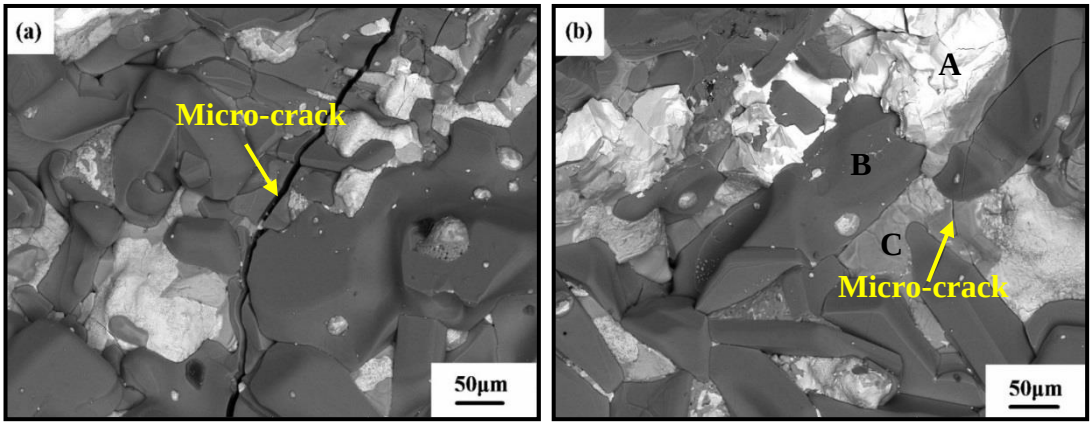

Figure 3-14. Typical morphology of the prepared coating, (a) SMC, (b) SMCnw.

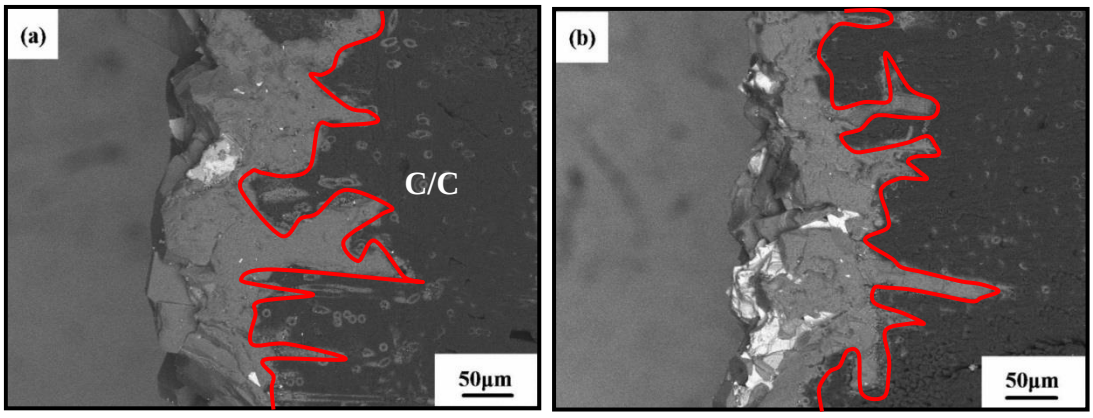

Figure 3-15. Cross-section micrograph of the Si-Mo-Cr coating, (a) SMC, (b) SMCnw.

Cycling ablation test of the coated C/C composites from 1600 °C to room temperature is performed using parallel oxyacetylene torch (as described in Chapter 2). The mass loss per unit area is shown in Figure 3-16. The time of each cycle is set as 5 s. After 30 thermal

cycles, the mass loss per unit area of SMC is about 28 mg·cm^{-2}. In contrast, the mass loss per unit area of SMCnw is about 15 mg·cm^{-2}. Therefore, it can be deduced that the combination of blasting treatment and in-situ grown SiC nanowires can improve the thermal cycling performance of Si-Mo-Cr coating more effectively. According to the trend of the curve, the mass loss curve can be divided into three stages, marked as S_1, S_2 and S_3 respectively. The cyclic ablation behavior of the coating will be discussed according to the noted three stages later.

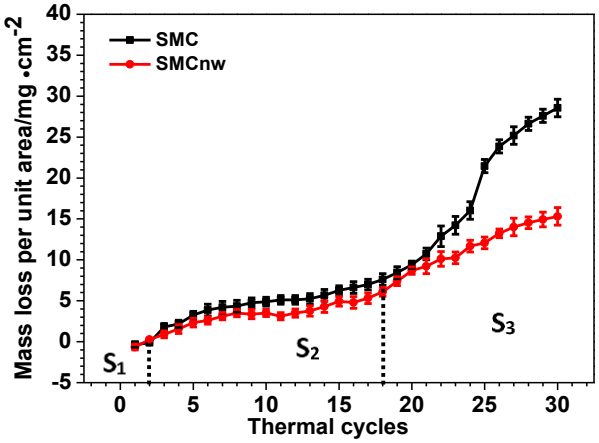

Figure 3-16. Mass loss per unit area of the Si-Mo-Cr coated C/C composites during thermal cycling test using oxyacetylene torch.

Figure 3-17 shows the surface morphology and EDS analysis of the sample after cyclic ablation test. It can be observed that a glassy layer, deduced as SiO_2 + Cr_2O_3 (Figure 3-17 (c)), is formed. In addition, micro-crack is observed on the surface of both SMC and SMCnw after cyclic ablation test. The micro-crack can provide the entrance channel for the oxyacetylene torch, and the protective ability of the formed SiO_2+Cr_2O_3 glassy protective layer will be degraded due to the shear action of oxyacetylene torch. With respect to the surface morphology of SMC (Figure 3-17 (a)), the size of micro-crack on the surface of S-2 reduces considerably after cyclic ablation test (Figure 3-17 (b)). Cross-section images of the sample after 30 thermal cycles are shown in Figure 3-18. It is found that penetrating crack is formed in the coating of SMC (Figure 3-18 (a)). In addition to the thickness decrease, the coating of SMCnw remains intact and no penetration crack is found (Figure 3-18 (b)).

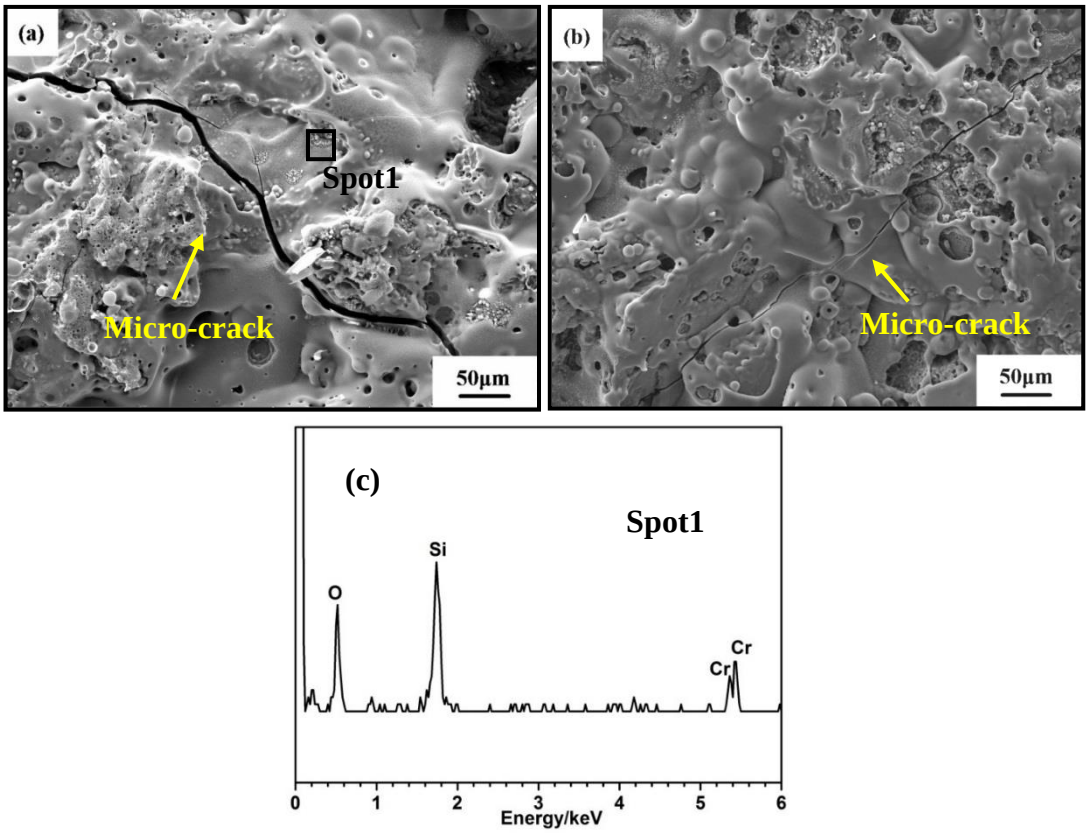

Figure 3-17. Surface morphology of the Si-Mo-Cr coated C/C composites after thermal cycling test, (a) SMC, (b) SMCnw, (c) EDS analysis of Spot1.

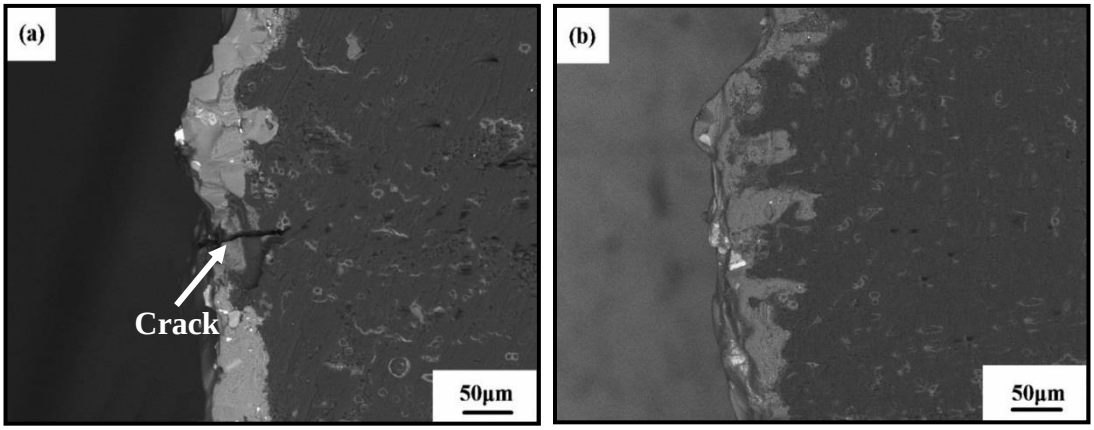

Figure 3-18. Cross-section micrograph after cyclic ablation test, (a) SMC, (b) SMCnw.

3.4.2 Ablation mechanism

The gas environment of oxyacetylene torch is oxygen-rich. During the thermal cycling test, the following reactions will occur [72, 73]:

$$SiC\,(s) + 2O_2\,(g) \rightarrow SiO_2(s) + CO_2\,(g) \qquad (3\text{-}1)$$

$$2SiC\,(s) + 3O_2\,(g) \rightarrow 2SiO_2\,(s) + 2CO\,(g) \qquad (3\text{-}2)$$

$$Si\,(s) + O_2(g) \rightarrow SiO_2(s) \quad (3\text{-}3)$$

$$4CrSi_2(s) + 11O_2(g) \rightarrow 8SiO_2(s) + 2Cr_2O_3\ (g) \quad (3\text{-}4)$$

$$CrSi_2(s) + 3O_2(g) \rightarrow 2SiO_2(s) + CrO_2\ (g) \quad (3\text{-}5)$$

$$2MoSi_2(s) + 7O_2(g) \rightarrow 4SiO_2(s) + 2MoO_3\ (g) \quad (3\text{-}6)$$

Based on the above reactions, the oxidation of SiC, Si and $CrSi_2$ (reaction (3-1)-reaction (3-5)) is a mass gain process, while the oxidation of $MoSi_2$ (reaction (3-6)) is a mass loss process. From Figure 3-16, at the initial stage of the cyclic ablation test (S_1), the ablation of the coating gains mass. It is demonstrated that the oxidation of $MoSi_2$ (reaction (3-6)) in a short time has little impact on the mass change trend of the coating [73]. As a result, in this stage, the mass gain can be mainly attributed to the formation of SiO_2 and Cr_2O_3 (reaction (3-1)-reaction (3-5)). Then with the increase of thermal cycles, at the stage of S_2, the mass loss per unit area is relatively stable, indicating that the formed glassy layer of SiO_2 and Cr_2O_3 plays an effective role in resisting the attack of the oxyacetylene torch. At the stage of S_3, the mass loss per unit area rises quickly. Concerning the morphology before thermal cycling test (Figure 3-15), the thickness of both coatings is reduced after the test (Figure 3-18). During the conventional thermal cycling test in a high-temperature furnace, the coating thickness usually remains unchanged after thermal cycling test, and the corresponding mass loss is primarily attributed to the oxidation of C/C substrate. In this work, no obvious oxidation of C/C substrate can be found (as shown in Figure 3-18). Hence, at the stage of S_3, the increase of mass loss per unit area can be mainly attributed to the reduction of coating thickness caused by the mechanical erosion of oxyacetylene torch. In addition, it can be found that the mass loss per unit area of SMCnw changes slowly (Figure 3-16).

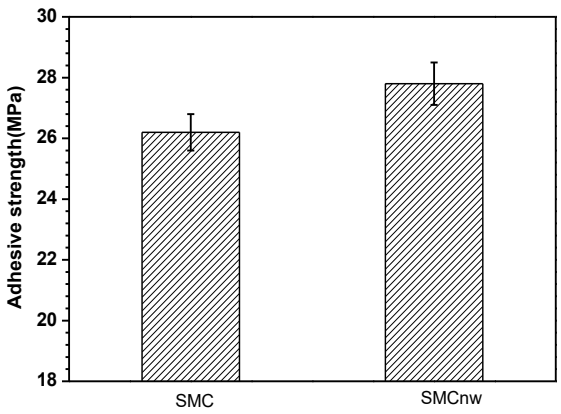

Figure 3-19. Adhesive strengths of Si-Mo-Cr coated C/C composites.

To illustrate the role of SiC nanowires, adhesive strength and CTE testing are conducted. Figure 3-19 shows the adhesive strengths of the coating, which illustrates that the combination of blasting treatment and in-situ grown SiC nanowires can better improve the adhesive strength of the coating. Figure 3-20 shows the fracture surface morphology of the SMCnw sample. Some pullout nanowires can be observed. The pullout of SiC nanowires can dissipate fracture energy, resulting in the improvement of adhesive strength.

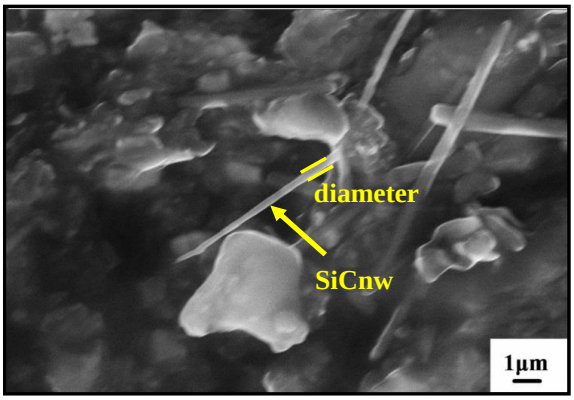

Figure 3-20. Coating fracture surface morphology of the SMCnw sample.

Figure 3-21 shows the CTE of bare C/C and the Si-Mo-Cr coated C/C. It can be found that the C/C substrates present the similar thermal expansion behavior with the coated C/C composites under the same conditions. As a result, the measured results can reflect the CTE difference of the prepared coating. We can see that SiC nanowires are beneficial for restricting the expansion of the coating materials as the temperature increases. During cyclic ablation test, the thermal stress (σ) can be described as follows [74]:

$$\sigma = \Delta T \Delta \alpha \frac{E}{1-\nu} \tag{3-7}$$

where ΔT is the difference between cooling temperature and zero stress temperature, $\Delta\alpha$ is the CTE difference between the coating and the substrate, E and ν are the Young's modulus and Poisson ratio of the coating, respectively. Zero stress temperature can be assumed as the preparation temperature of Si-Mo-Cr coating. From equation (3-7), it can be found that the CTE mismatch has an obvious effect on the thermal stress during cyclic ablation test. With respect to SMCnw, the weaker bonding strength and the mismatch of CTE have caused higher thermal stress of SMC during cyclic ablation test, resulting in the formation of micro-crack or even penetrating cracks (Figure 3-17 (a) and Figure 3-18 (a)). As a result, the protective ability of the formed protective layer of SiO_2 and Cr_2O_3 will be degraded. This could be the primary reason for the rapid mass loss of SMC at the stage of S_3 (Figure 3-16).

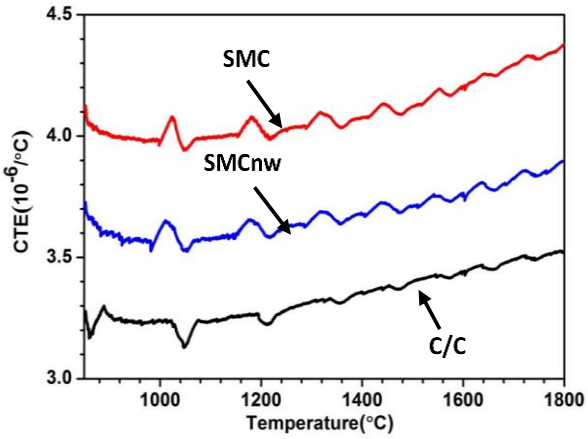

Figure 3-21. Coefficients of thermal expansion of the C/C and the Si-Mo-Cr coated C/C.

3.5 Conclusions

1. C/C composites were pre-blasting treated in different heat fluxes using oxyacetylene torch (0, 2.38, 3.2 and 4.18 MW/m^2). After blasting treatment, a rough and porous structure was achieved on the surface of C/C composites. SiC coating was prepared on the treated C/C composites by pack cementation, where an inlaid interface with different structures between SiC coating and C/C substrate was obtained. The formed inlaid interface can improve the coating/substrate adhesive strength efficiently. Compared with the coated C/C composites without blasting treatment, the maximum adhesive strength was increased by 43%.

2. Si-Mo-Cr coating was prepared on the surface of blasting-treated C/C. After 25 thermal cycles from 1600^{o}C to room temperature, due to the formed inlaid coating/substrate interface, the morphology of the coating was uniform with the formation of a glassy SiO_2 + Cr_2O_3 protective layer on the surface.

3. Blasting treatment of C/C composites and in situ grown SiC nanowires was proposed to further improve the thermal cycling performance of Si-Mo-Cr coating. Compared with the coated C/C composites with blasting treatment only, the coating/ substrate adhesive strength was increased by 5.7%. After 30 thermal cycles between 1600^{o}C and room temperature using parallel oxyacetylene torch, the mass loss per unit area of the coated C/C composites with blasting treatment only was up to 28 mg·cm^{-2} and penetrating crack was formed. In contrast, the mass loss per unit area of the coated C/C composites with the combination of blasting treatment and in-situ grown SiC nanowires was about 15 mg·cm^{-2}. The performance improvement can be attributed to the enhancement of adhesive strength and the efficient alleviation of thermal expansion coefficient mismatch between the substrate and the coating, thus decreasing the thermal stress during high-low temperature cycles.

Chapter 4: The effects of C/C blasting treatment and modifying SiC coating with SiC/HfC (ZrB_2)

4.1 Introduction

Due to instability of the formed SiO_2 glassy layer, Si-based ceramics coatings (for example, SiC and Si-Mo-Cr in chapter 3) are prone to be disabled at higher temperature (>1700°C), after longer oxidation durations or under high-speed combustion gas erosion [75]. UHTCs (Carbides, nitrides and borides of refractory metals) are aroused wide concern attributed to their high-melting points, good mechanical properties, oxidation performances and ablation resistances [12-16]. The addition of UHTCs into SiC coating is expected to improve its oxidation performance. In chapter 3, we find that the coating/substrate interface modification can improve the performance of Si-based ceramic coatings in combustion environment. But its performance is limited because of the rapid oxidation of SiC >1700°C. As a result, to enhance the cyclic ablation performance of SiC coating above 1700°C, in this chapter, blasting treatment of C/C and UHTCs additives are combined.

4.2 Blasting treatment and modifying SiC coating with SiC/HfC additive

As a typical UHTC, HfC is a potential candidate for thermal protection system due to its high melting point, retained strength at high temperature and good ablation resistance [24, 76-78]. As a result, the addition of HfC into SiC coating might be a good choice to improve its oxidation resistance above 1700°C [35, 79-81]. In this section, blasting treatment of C/C and HfC addition are combined to enhance the cyclic ablation performance of SiC coating. Cyclic ablation test from 1750°C to room temperature is conducted. Detailed descriptions of the cyclic ablation test are shown in chapter 2. In each cycle, the ablation duration is set as 10 s. Each sample is tested for 8 cycles. For convenience, the samples without and with blasting treatment are noted as H-S-1 and H-S-2, respectively.

4.2.1 Microstructure and cyclic ablation test

Figure 4-1 shows the typical surface morphology of the prepared coating after pressure-less reactive sintering. Two phases presented as white and grey colors can be distinguished as HfC and SiC respectively. The corresponding cross-section micrographs are shown in Figure 4-2, in which the interface between the coating and the C/C substrate is marked by a red line.

It is found that an inlaid interface structure is constructed for H-S-2 (Figure 4-2 (b)). As for H-S-1, the interface between the coating and C/C substrate exhibits a straight structure (Figure 4-2 (a)). The results are the same as discussed in chapter 3.

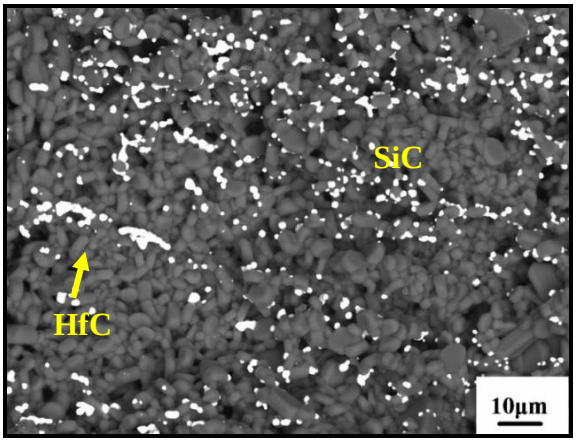

Figure 4-1. Typical surface morphology of the prepared HfC-SiC coating by pressure-less reactive sintering.

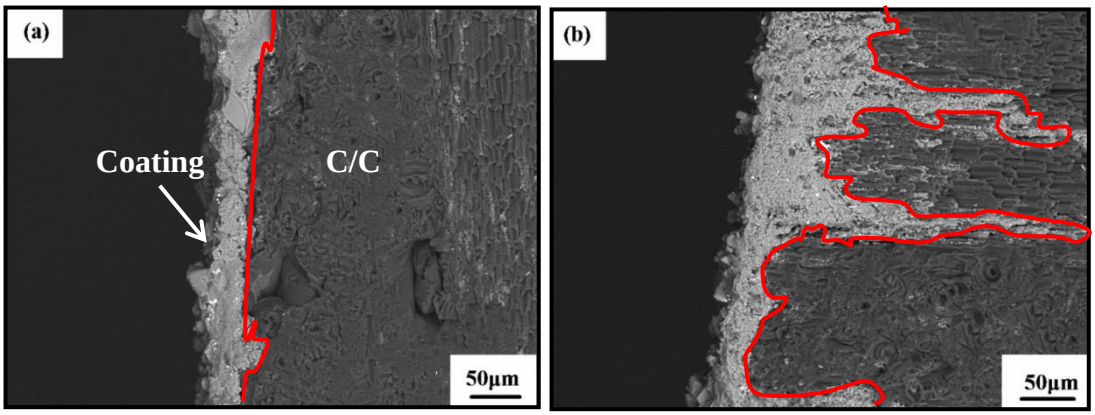

Figure 4-2. Cross-section micrograph of the HfC-SiC coating for C/C, (a) H-S-1, (b) H-S-2. The red line shows the substrate/coating interface.

Figure 4-3 shows the typical surface temperature curve in one thermal cycle. It could be found that the ablation time at maximum temperature (1750°C) is about 6 s. Figure 4-4 presents the mass loss per unit area of the sample during cyclic ablation test. Compared with H-S-1, after 8 thermal cycles from 1750°C to room temperature, the mass loss per unit area of H-S-2 is decreased obviously, which is about 36 $mg \cdot cm^{-2}$. Compared with the cyclic ablation test about SiC coating [82], the addition of HfC indeed improved the oxidation resistance of SiC coating in the combustion environment.

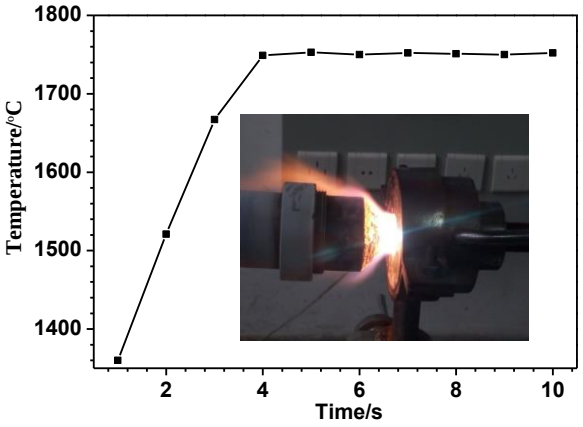

Figure 4-3. Surface temperature curve of the sample in one thermal cycle.

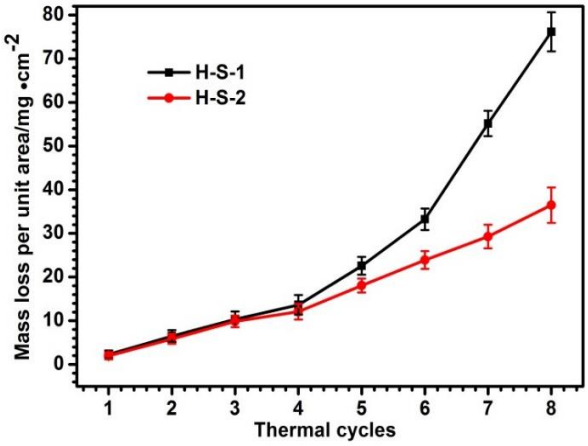

Figure 4-4. Variation in mass loss per unit area with the number of thermal cycles of the HfC-SiC coated C/C composites.

The corresponding surface morphologies after cyclic ablation test are shown in Figure 4-5. It can be found that the coating of H-S-1 is partially peeled off with the formation of many cracks (Figure 4-5 (a)). As seen in the enlarged view of Figure 4-5 (a), carbon fibers can be clearly observed, indicating the exposure of C/C substrate (Figure 4-5 (b)). The formation of the cracks can be mainly attributed to CTE difference between the coating and C/C substrate. During cyclic ablation test, the cracks will provide diffusion channels for the oxyacetylene torch, thereby resulting the debonding of the coating. This could be the reason why the mass loss per unit area increases quickly (Figure 4-4). As for H-S-2, the surface morphology is uniform (Figure 4-5 (c)). By the EDS analysis (Figure 4-5 (d-e)), two phases deduced as HfO_2 and SiO_2 are formed on the surface. The test results demonstrate that the formed mixed layer of HfO_2 and SiO_2 can act as a good barrier to the denudation under the effect of oxyacetylene

torch. Cross-section images of H-S-1 and H-S-2 are shown in Figure 4-6. To H-S-1, it is observed that the coating is flaked off and the C/C substrate is subjected to erosion (Figure 4-6 (a)). As for H-S-2, although the morphology of C/C substrate still remains intact (Figure 4-6 (b)), the coating is almost consumed.

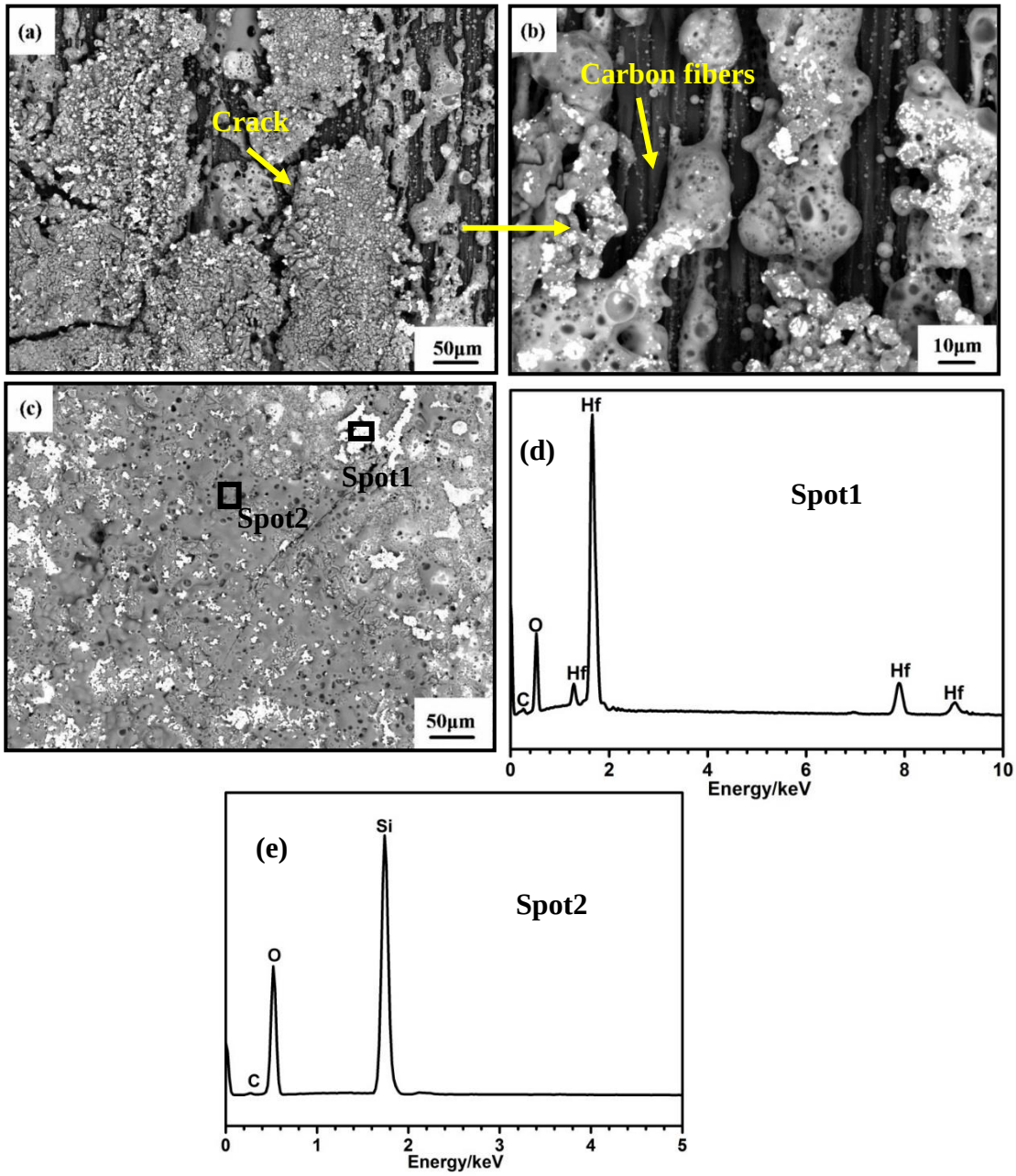

Figure 4-5. Surface morphology of the HfC-SiC coated C/C composites after undergoing thermal cycling for 8 times between 1750°C and room temperature, (a) H-S-1, (b) Enlarged view of (a), (c) H-S-2, (d) EDS analysis of Spot1, (e) EDS analysis of Spot2.

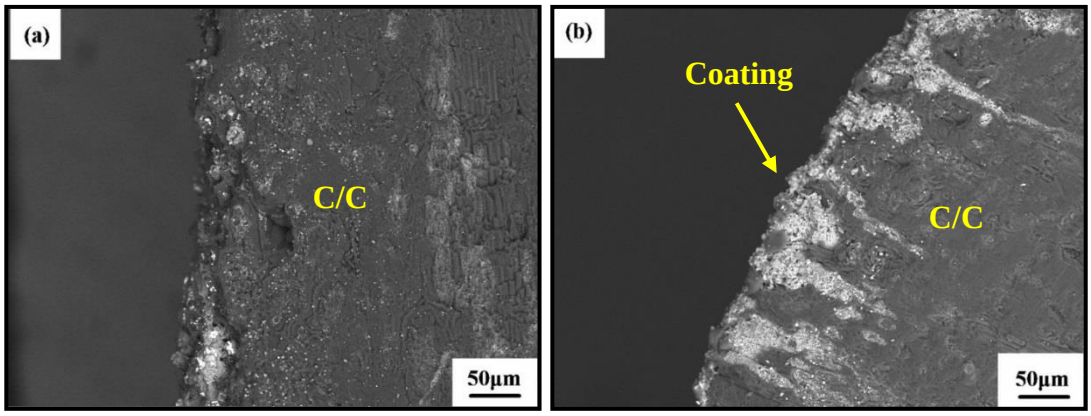

Figure 4-6. Cross-section micrograph of the HfC-SiC coated C/C after undergoing thermal cycling between 1750°C and room temperature, (a) H-S-1, (b) H-S-2.

4.2.2 Ablation mechanism

Since the oxyacetylene torch is oxygen-rich, the following reactions will take place [80, 83] during the cyclic ablation test using oxyacetylene torch.

$$\frac{1}{2}HfC\ (s) + O_2(g) = \frac{1}{2}HfO_2(s) + \frac{1}{2}CO_2(g) \quad (4\text{-}1)$$

$$\frac{2}{3}HfC\ (s) + O_2(g) = \frac{2}{3}HfO_2(s) + \frac{2}{3}CO(g) \quad (4\text{-}2)$$

$$\frac{1}{2}SiC\ (s) + O_2(g) = \frac{1}{2}SiO_2(l) + \frac{1}{2}CO_2(g) \quad (4\text{-}3)$$

$$\frac{2}{3}SiC\ (s) + O_2(g) = \frac{2}{3}SiO_2(l) + \frac{2}{3}CO(g) \quad (4\text{-}4)$$

The corresponding standard Gibbs free energy changes of the reactions were calculated by HSC software, as is shown in Figure 4-7. The lower the standard Gibbs free energy is the greater tendency of a chemical reaction to occur [83]. According to Figure 4-7, the mentioned chemical reactions (reactions (4-2) and (4-4)) play the leading roles. Based on the calculations of standard Gibbs free energies (Figure 4-7), the analysis of mass loss curves (Figure 4-4) and the observation of surface morphologies (Figure 4-5), the performance enhancement of HfC-SiC coating can be primary attributed to the formed mixed layer of HfO_2 and SiO_2, which possesses better stability than SiO_2 at 1750°C under oxyacetylene torch. In addition, compared with H-S-1, the ablation performance of H-S-2 can be mainly attributed to the formed inlaid coating/substrate interface.

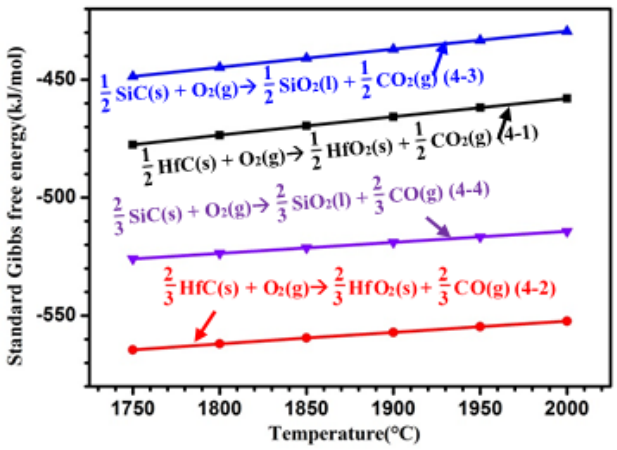

Figure 4-7. Changes of standard Gibbs free energies of reactions (4-1)-(4-4) at different temperatures calculated by HSC software [83-85].

4.3 Blasting treatment and modifying SiC coating with SiC/ZrB_2 additive

In section 4.2, HfC is introduced into SiC coating by pressure-less reactive sintering so as to promote the thermal stability of the SiO_2 glass. However, when the ablation time further extended, the performance enhancement is restricted due to the coating brittleness caused by its limited sintering performance, which affected the thermal stability of the formed HfO_2-SiO_2 protective layer to the attack of oxyacetylene torch and then resulted in the performance degradation. So it is recognized that pretreatment of the substrate and structure optimization of the coating should be combined. ZrB_2, as one of UHTCs, is also regarded as a promising material for thermal protection system because of its sufficient retained strength at high temperature and high melting point [9, 86-89]. It has been reported that ZrB_2 addition is beneficial for reducing the SiO_2 consumption [9, 87, 88], and the glass formed by B_2O_3 and SiO_2 (the oxidation products of ZrB_2 and SiC) also possesses good self-sealing performance in a larger temperature range. Furthermore, the CTE difference between ZrB_2 and SiC is smaller than that of HfC and SiC ($\alpha_{ZrB2}=5.9\times10^{-6}/K$ [18], $\alpha_{SiC}=4.5\times10^{-6}/K$ [90], $\alpha_{HfC}=6.6\times10^{-6}/K$ [91]), which could benefit for the improvement of sintering performance and then make it easier for the coating preparation. So, interface modification combined ZrB_2 additive is expected to possess a better application prospect to promote the performances of SiC coating under the condition of combustion gas corrosion. In addition, whether the inlaid interface can improve the oxidation properties of the prepared coating still needs to be studied, which is not discussed before. For the convenience of discussion, in this section, the samples without and with blasting treatment are noted as Z-S-1 and Z-S-2, respectively.

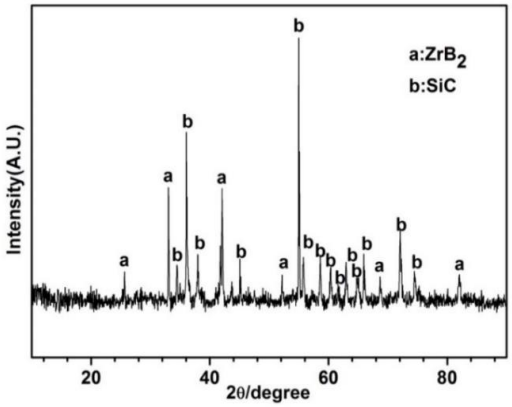

Figure 4-8. XRD spectra of the coating fabricated by pressure-less reactive sintering.

Figure 4-8 shows the XRD pattern of the prepared coating, peaks of ZrB_2 and SiC can be observed. Figure 4-9 presents the cross-section image of Z-S-1 and Z-S-2. For Z-S-2, the length of coating/substrate interfaces increase, and an inlaid interface structure is obtained (Figure 4-9 (b)). By contrast, for Z-S-1, a relatively smoothed coating/substrate interface structure is achieved because of the lack of a porous surface layer.

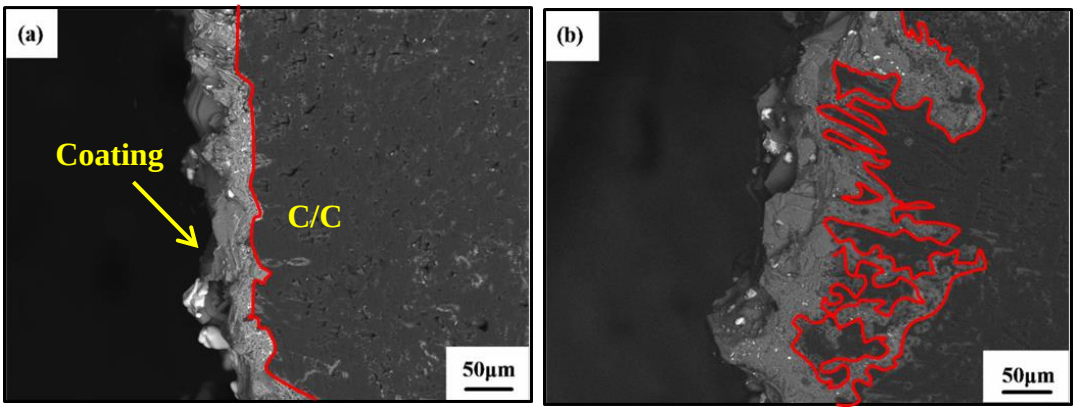

Figure 4-9. Cross-section morphologies of the coating, (a) Z-S-1, (b) Z-S-2.

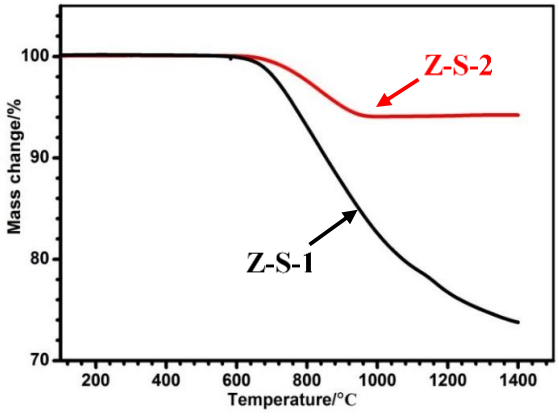

Figure 4-10. Thermal gravimetric analyses in air of the fabricated coating in air.

Figure 4-10 presents the TGA curves of Z-S-1 and Z-S-2 in air. The results show that as temperature increases, the mass loss of Z-S-1 increases gradually. As the testing temperature approaches 1400°C, its mass loss is about 26%. In comparison, the mass loss of Z-S-2 is decreasing, demonstrating that the increased coating/substrate interfaces could promote the oxidation performance of the coating efficiently. Figure 4-11 shows the experimental setup and temperature curve, which is the same to that of HfC-SiC coating, as discussed in section 4.2. The difference is that the ablation time of each cycle is set as 20 s. The sample is tested for 5 cycles. Figure 4-12 displays the mass loss of the prepared coating during cyclic ablation test. Compared with the tested results of the HfC-SiC coating (shown in Figure 4-4), Z-S-2 shows better cyclic ablation performance, after ablation for the same time, its mass loss per unit area is about 14 mg·cm^{-2}. With respect to Z-S-1, after 5 thermal cycles, the mass loss of Z-S-2 is reduced significantly, which is about 42 mg·cm^{-2}.

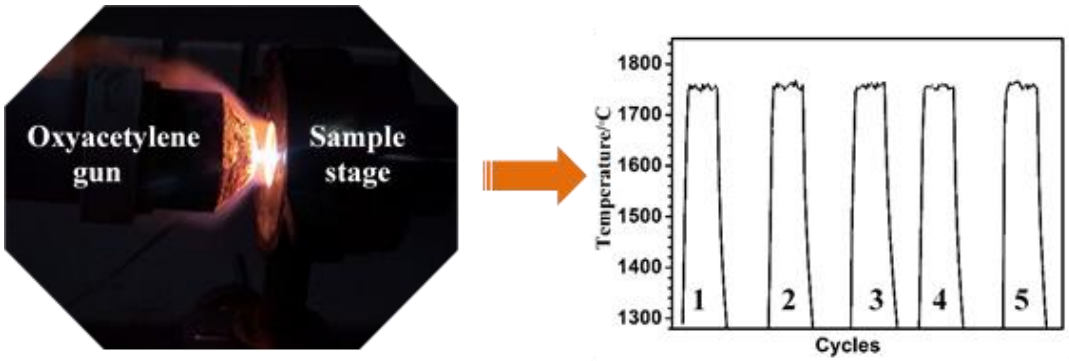

Figure 4-11. Experimental setup for cyclic ablation test (right) and the increasing temperature curve of the tested sample during ablation (left).

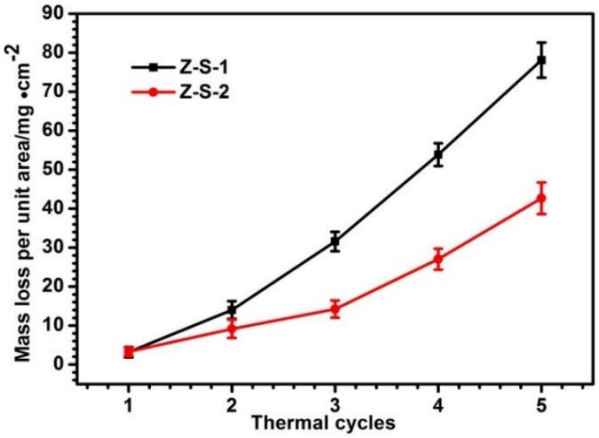

Figure 4-12. The mass loss with the increase of thermal cycle of the fabricated coating.

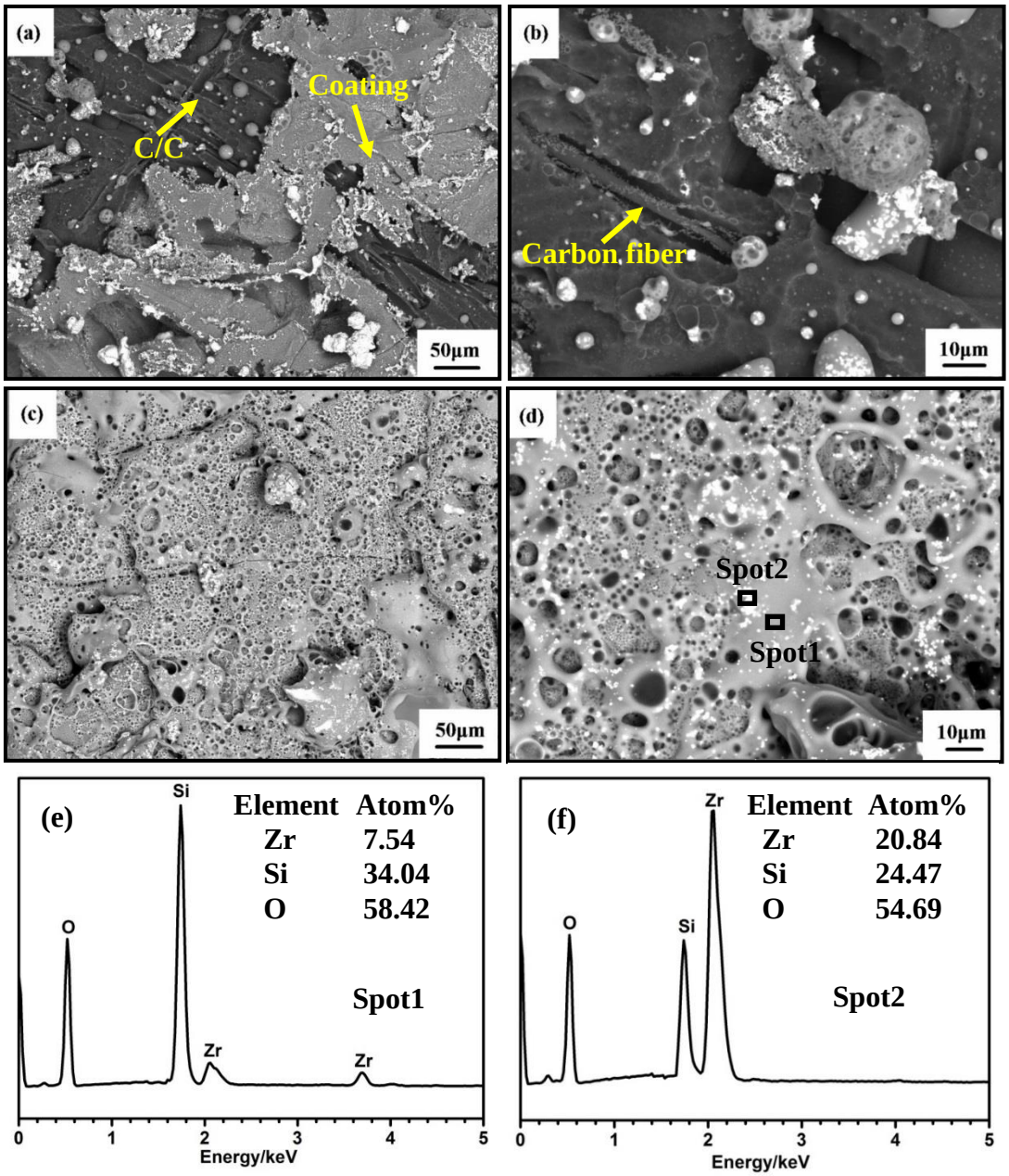

Figure 4-13. SEM images of the fabricated coating after cyclic ablation test using oxyacetylene torch from 1750°C to room temperature (ablation at 1750°C for 80 s in total), (a) Z-S-1,(b) the magnified image of (a), (c) Z-S-2, (d) the enlarged image of (c), (e) EDS of Spot1, (f) EDS of Spot2.

Surface morphologies of Z-S-1 and Z-S-2 after cyclic ablation test using oxyacetylene torch are exhibited in Figure 4-13. From Figure 4-13 (a-b), the coating of Z-S-1 is partially peeled off, leading to the erosion of C/C substrate. Some defects (cracks and holes) are observed on the surface. The formed defects can act as the diffusion paths to the oxyacetylene torch and enhance its denudation. In contrast, the surface of Z-S-2 is uniform and covered by a glassy layer (Figure 4-13 (c-d)). As a result of the evaporation of the generated gaseous

oxidation products, some micro-pores can be observed on the glassy layer. With the help of EDS analysis (Figure 4-13 (e-f)), the white phase is rich in element of Zr and the grey phase is rich in element of Si. The formed Zr-O-Si glassy layer can resist the denudation of the oxyacetylene torch during cyclic ablation test. Compared with Z-S-1(Figure 4-13 (a-b)), the better performance of Z-S-2 can be mainly result from the thermal stability improvement of the Zr-O-Si protective layer which resists the attack of the oxyacetylene torch. Figure 4-14 shows the corresponding cross-section images of Z-S-1 and Z-S-2 after cyclic ablation test. Despite the reduced thickness of the coating, C/C substrate of Z-S-2 is still uniform, further illustrating its good ablation performance (Figure 4-14 (b)). As for Z-S-1, the coating is flaked off and the C/C substrate suffers severe erosion (Figure 4-14 (a)).

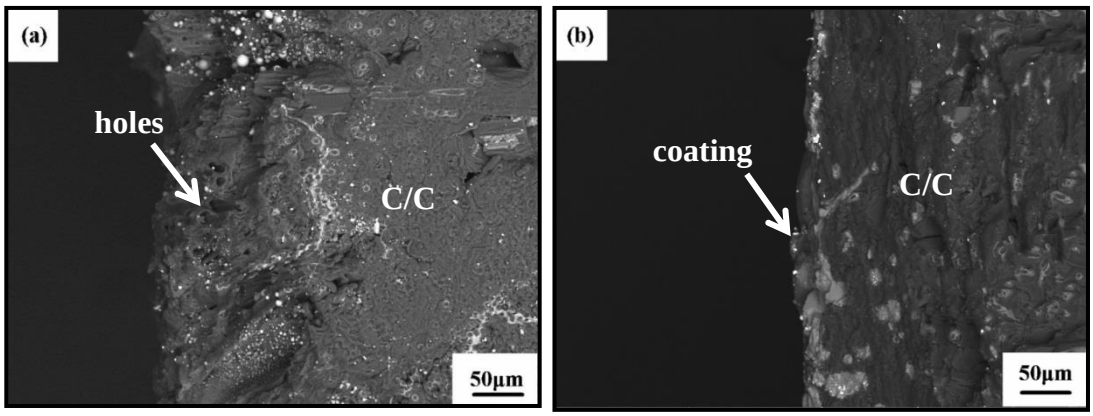

Figure 4-14. Cross-section morphologies of the fabricated coating after cyclic ablation test, (a) Z-S-1, (b) Z-S-2.

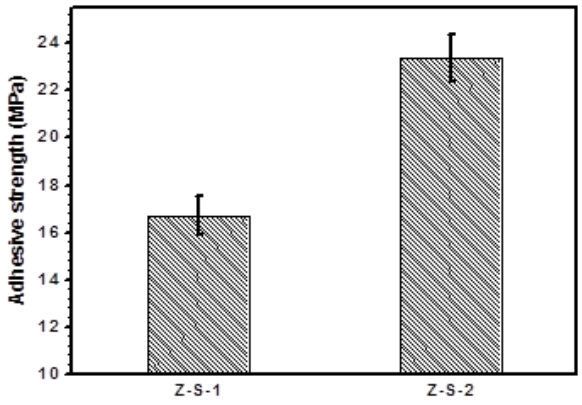

Figure 4-15. Adhesive strength of the fabricated coating before cyclic ablation test.

The results of adhesive strength measurement are shown in Figure 4-15. The adhesive strength of Z-S-2, compared with Z-S-1, is improved. In the cyclic ablation test of HfC-SiC coating (as reported in section 4.2), we found that when the ablation time further increased,

effect of the increased coating/substrate interfaces was restricted by the coating brittleness derived from its limited sintering performance. However, the prepared coating, compared with the HfC-SiC coating (as discussed in section 4.2), presents better sintering performance, which efficiently contributes to improve the thermal stability of the formed Zr-O-Si glassy layer.

4.4 Conclusions

1. To enhance the cyclic ablation performance of SiC coating from 1750ºC to room temperature under vertical oxyacetylene torch, blasting treatment of C/C composites and HfC additive were proposed. Cyclic ablation test results showed that because of the inlaid coating/substrate interface and the formed mixed layer of HfO_2 and SiO_2, the ablation performance of SiC coating at 1750ºC under oxyacetylene torch was improved by the addition of HfC.
2. Instead of HfC, blasting treatment of C/C and ZrB_2 additive were combined to improve the performance of SiC coating. Thermogravimetric analysis results obtained in air showed that due to the increased coating/substrate interfaces, the mass loss was reduced significantly. Cyclic ablation test using oxyacetylene torch from 1750°C to room temperature showed that the ablation properties of SiC coating were enhanced efficiently. After 5 thermal cycles including ablation at 1750°C for 80 s, the mass loss per unit area was about 42 $mg \cdot cm^{-2}$. The formed Zr-O-Si glassy protective layer showed good thermal stability which could withstand the denudation of oxyacetylene torch efficiently. The good sintering performance and the inlaid interfaces were beneficial for improving the adhesive strength and relieving the thermal mismatch, thereby reducing the thermal stress and enhancing the thermal stability of the Zr-O-Si glassy protective layer during cyclic ablation test.

Chapter 5: Develop a non-destructive characterization method for multilayer ceramic coating

5.1 Introduction

In chapter 4, the addition of UHTCs (HfC and ZrB_2) into SiC coating can enhance the ablation performance of SiC coating at 1750°C. However, after longer ablation, the performance of SiC coating decreases obviously, thereby limiting its performance. How to meet the requirements for operating in much higher temperature and stronger combustion gas erosion? Two methods might be a chosen. The first one is to prepare multi-layer ceramic coating, where UHTCs can act as the outer layer to resist the extremely high temperature. The other one is to introduce UHTCs into the C/C matrix (this will be discussed in chapter 6). To facilitate the design and performance analysis of multi-layer ceramic coating, it is important for us to develop a dedicated characterization method. In this chapter, particle-induced X-ray emission (PIXE) combined with Kossel diffraction is proposed. The feasibility of this method is firstly investigated in film waveguides made up of single metals. Then simulations regarding the HfC/SiC/HfC multilayer for C/C composites are given.

5.2 Particle-induced X-ray emissions (PIXE)

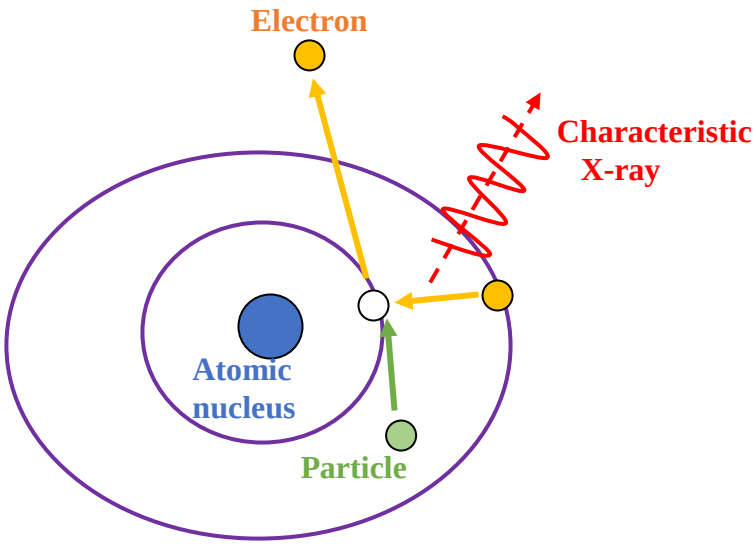

Figure 5-1. Schematic diagram of PIXE.

PIXE analysis is a very sensible ion beam analytical method for elemental composition study. It possesses a good sensitivity to measure the characteristic radiation emitted when electron state changes without destruction of the sample [92, 93]. Figure 5-1 displays the process of PIXE. In the first step, due to the incident energetic charged particle, the atom is ionized by removing an electron from an inner electronic shell. Then this inner shell vacancy is filled by an electron from an outer shell. The electron transition generates the emission of characteristic X-rays at energy corresponding to the binding energy difference of the inner and outer atomic shells.

5.3 Kossel interferences

Kossel interferences, evidenced by Walther Kossel in 1935 [94], are the typical diffraction patterns of the characteristic X-rays emitted within a crystalline structure and sensitive to the structure itself. Since 1970s, it has been applied as a tool to investigate the crystallographic orientations and lattice parameters [95-97]. The observation of Kossel interferences requires two necessary steps. Firstly, characteristic X-ray emissions are produced. Then the produced X-ray emissions are diffracted by the periodic structure itself. The ionization source can be energetic electrons [98-100], X-ray photons [101, 102], charged particles including protons or ions [92, 103]. Kossel diffraction associated to X-rays is related to the grazing exit x-ray fluorescence technique [95, 104].

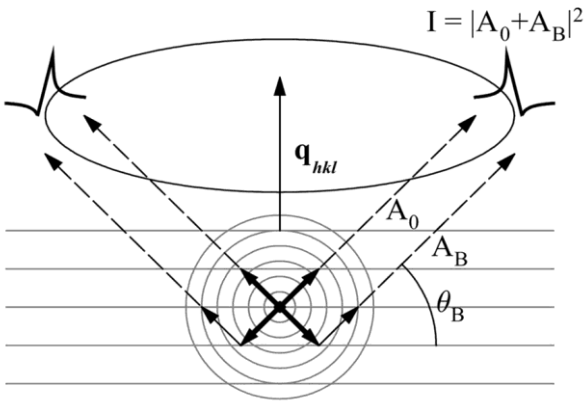

Figure 5-2. Scheme of the formation of Kossel lines [105]. Arrows indicate relevant direct (thick arrows) and reflected (thin arrows) plane-wave components of the X-ray emission.

Figure 5-2 displays the schematic diagram of the Kossel diffraction. The X-ray radiation emitted by the atoms (A_0) in the sample interferes with its Bragg reflection (A_B), resulting in the strong intensity modulations ($I = |A_0 + A_B|^2$) in the vicinity of cones. The cones are

defined by the normal to the diffracting plane (hkl) for a crystal or to the surface for a multilayer and the Bragg angle (θ_B). Yet Kossel diffraction possesses its unique advantages: the ionization source (used to generate the X-ray emission) can be introduced from any directions. In our study, with the help of a spatially resolved X-ray color camera, the whole experimental setup can be fixed.

5.4 X-ray waveguides

In this section, the theoretical background of X-ray waveguide is presented. The simplest structure of a waveguide can be regarded as layered system, as shown in Figure 5-3. The waveguide consists of two different materials with different index of refraction (n_1, n_2). When X-ray passes through matter, absorption (which reduces transmission) and dispersion or refraction (wavelength dependency of the propagation velocity) occur. So n, the optical index, can be written as the following formula,

$$n= 1- \delta + i\beta \qquad (5\text{-}1)$$

where δ is the refractive index decrement and β is the absorption index. For each material used in this thesis, the complex refractive index as a function of the energy/wavelength of the electromagnetic wave is taken from the CXRO X-ray database [61].

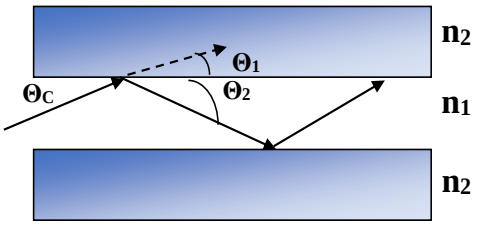

Figure 5-3. Principle of the waveguide.

For the waveguide, one thin layer of the material with the smaller δ is sandwiched in-between two layers of the material with a higher δ. The center layer is the guiding layer and the external ones are the cladding layers (as shown in Figure 5-3). It could support the propagation of electromagnetic waves with a certain field distribution. The refraction at the boundaries can be described by Snell's law:

$$n_1 \cos\theta_1 = n_2 \cos\theta_2 \qquad (5\text{-}2)$$

A critical angle exists and is defined by $\cos\theta_C = n_2/n_1$. Above this value the rays enter the cladding ($\theta > \theta_C$); below this angle the radiation is reflected at the interface ($\theta < \theta_C$).

An electromagnetic wave transmitted through a waveguide has two field components that oscillate mutually perpendicular to each other. One is the electric filed and the other is the magnetic field. Modes in planar waveguides can be mainly classified in TE (transverse electric) and TM (transverse magnetic) modes. In TE mode, the electric field component is totally transverse to the direction of wave propagation whereas magnetic field is not totally transverse to the direction of wave propagation. In TM mode, the magnetic field component is totally transverse to the direction of wave propagation while the electric field is not totally transverse to the direction of wave propagation. Figure 5-4 displays an example of the field distribution for TE modes in the waveguide according to the reflectivity curve. When θ is lower than $\theta_{C,}$ different θ is corresponding to different TE mode. When the intensity of the electromagnetic field is maximum in the guiding layer, the corresponding reflectivity is a minimum value, indicating that the incident X-ray reaches the transmission window. Thus, the waveguide structure is convenient to concentrate the electric field of a specific X-ray emission in the guiding layer.

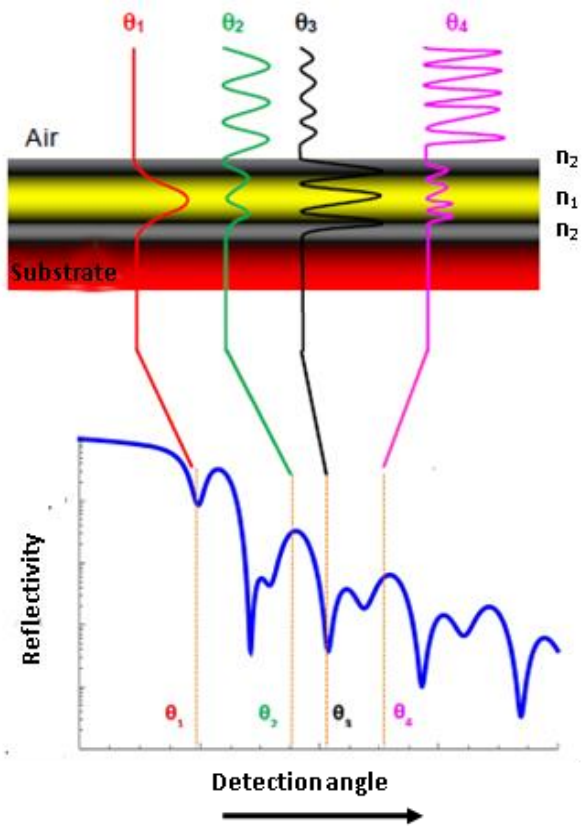

Figure 5-4. Field distribution for TE guided modes in the waveguide according to the reflectivity curve.

5.5 PIXE-Kossel to study thin film waveguides

In [59, 104, 106], a methodology, that is particle-induced X-ray emission (PIXE) combined with Kossel diffraction, is developed to study the structure of nano-scale Cr/Sc and Pd/Y periodic multilayers. The generated X-ray emission is recorded in Kossel geometry to obtain what we call the Kossel curve, which is the intensity of characteristic X-ray emission as a function of the detection angle. The obtained PIXE-Kossel curves with their shapes are sensitive to the structures of the corresponding multilayers. The results confirm that Kossel curves are convenient to study the interfacial environment in multilayers made of a periodic alternation of nanometer-thick films.

The aim of this study is to check the feasibility of this method when used in non-periodic stacks consisting in only a few layers. To observe well-contrasted Kossel curves, the stack is an X-ray planar waveguide formed of three layers. Here, Pt/Fe/Pt and Ta/Cr/Pt samples are designed, deposited on Si substrate and then investigated by the PIXE-Kossel method. The experimental and simulated Kossel curves are compared in order to obtain the description of the actual stack.

5.5.1 Design of the thin film waveguides

In this study, in the process for designing planar X-ray waveguide, we first performed electric field distribution simulations to optimize the structural parameters (including elements and thickness) using IMD software [60]. Interfacial and substrate roughness were assumed to be zero. Three thin films waveguides were designed:

- Pt(4 nm)/Fe(6 nm)/Pt(10 nm)/Si, noted PFP-1;
- Pt(4 nm)/Fe(8 nm)/Pt(10 nm)/Si, noted PFP-2;
- Ta(4 nm)/Cr(10 nm)/Pt(12 nm)/Si, noted TCP;

As an example, Figure 5-5 (a) and (b) show the simulated depth and angular distribution of the electric field in the PFP-1 stack at the photon energies of the Fe Kα and Pt Lα emissions, respectively. It is clearly seen that waveguide modes are formed in the Fe layer (guiding layer) at glancing angles close to 0.6° and 0.4° for the Fe Kα and Pt Lα emissions, respectively. This means that when the angle of detection is equal to these angles, an intensity maximum is expected for the corresponding Kossel curve. Any shift of the positions of the Fe or Pt atoms from the designed layers should give different position and amplitude of their features in the PIXE-Kossel curve.

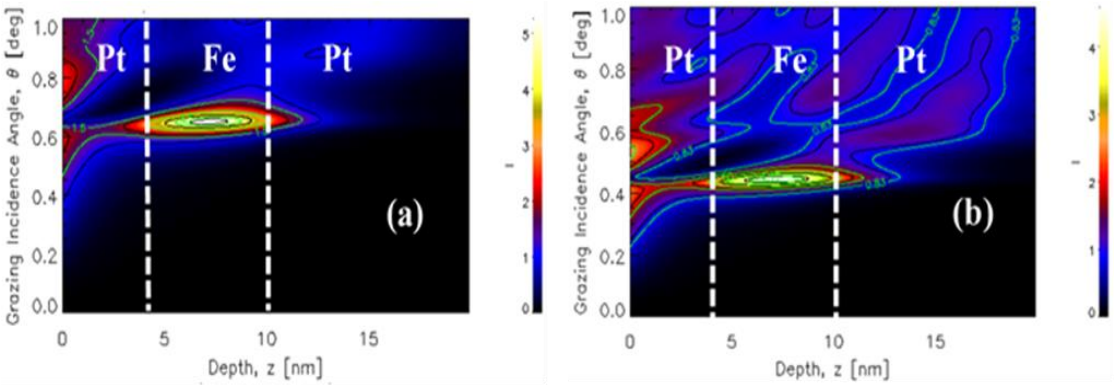

Figure 5-5. Simulated depth and angular distribution of the electric field in the planar PFP-1 X-ray waveguide at the photon energy corresponding to (a) the Fe Kα emission (6403 eV) and (b) the Pt Lα emission (9442 eV). The vertical color bar gives the intensity scale of the electric field.

5.5.2 Results and discussion

5.5.2.1 Analysis of Pt (4 nm)/Fe (6 nm)/Pt (10 nm) film waveguide

The XRR curve of the PFP-1 sample is shown in Figure 5-6. It displays the scattered X-ray intensity (in logarithmic scale) against the glancing angle. For the fitting procedure, no interfacial compound is firstly considered. The values of thickness and roughness of each layer obtained from the fitting results are listed in Table 5-1.

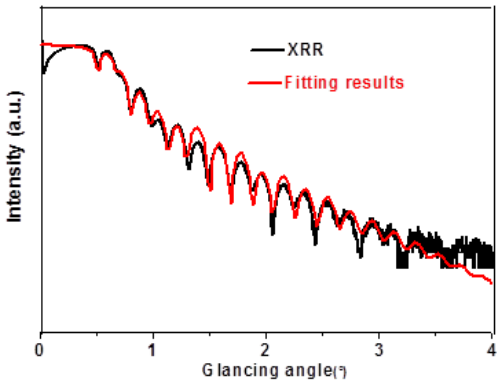

Figure 5-6. Measured (black line) and fitted (red line) XRR curves of the PFP-1 stack.

Table 5-1. Fitted values from XRR measurements of thickness, roughness and density of the different layers in the PFP-1 stack (listed from the top layer to the substrate).

	Thickness/Roughness (nm) (±0.05 nm)	Density
Pt	4.62/0.60	bulk
Fe	6.65/0.80	bulk
Pt	11.06/0.77	bulk
Si substrate	bulk/0.42	bulk

The densities, determined with an uncertainty of 10%, are close to those of the bulks. The above structural parameters (density, thickness and roughness of the layers) are then applied to the calculation of Kossel curves. The simulation is performed with the FLUORT code [107]. Details of the Kossel curve simulation are described in the Annex. It calculates the electric field generated within the stack by the emitted radiation according to the reciprocity theorem. In the calculation, all parameters (thicknesses of the layers and roughness of each interface) determined from XRR fitting are applied.

We then carry out the PIXE experiment and obtain the overall X-ray emission spectrum (intensity in logarithmic scale), as shown in Figure 5-7. The spectrum is the sum of the spectra obtained over all the pixels of the CCD camera. The energy calibration of the spectrum is performed from the position of the Fe Kα, Fe Kβ, Pt Lα and Pt Lβ emissions. Fe Kα and Pt Lα Kossel curves are discussed here.

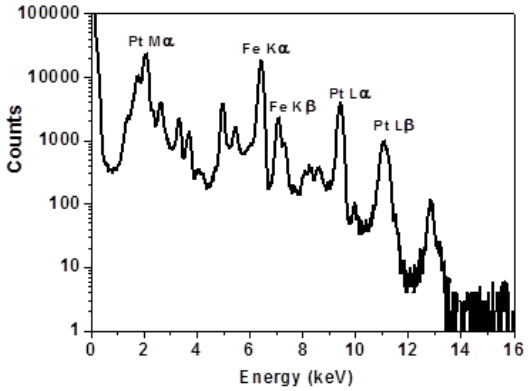

Figure 5-7. X-ray emission spectrum of the PFP-1 stack summed over all the pixels of the CCD camera.

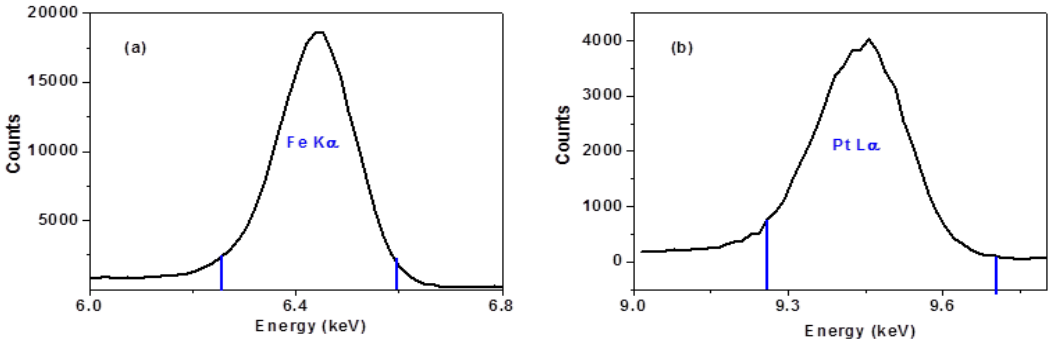

Figure 5-8. Fe Kα (a) and Pt Lα (b) ROI selected on the X-ray emission spectrum of the PFP-1 stack.

To extract the Fe Kα and Pt Lα Kossel curves, we select a ROI in the overall spectrum (shown in Figure 5-8). The ROI range is chosen to minimize the influence of neighboring

lines. The data processing is conducted in PyMCA software [108]. Based on the selected ROI, the Kossel curves are obtained, as shown in Figure 5-9 for Fe and Figure 5-10 for Pt. The generated signals deviate a little from the vertical direction (10 pixels from top to the bottom of the image).

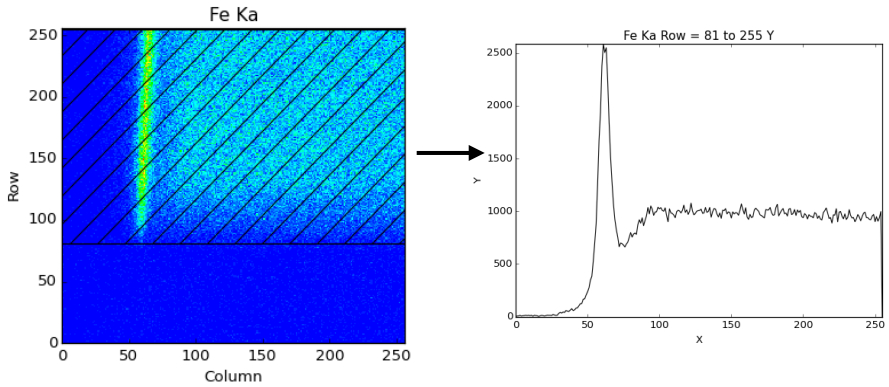

Figure 5-9. Intensity map (left) and the generated Kossel curve (right) of Fe Kα.

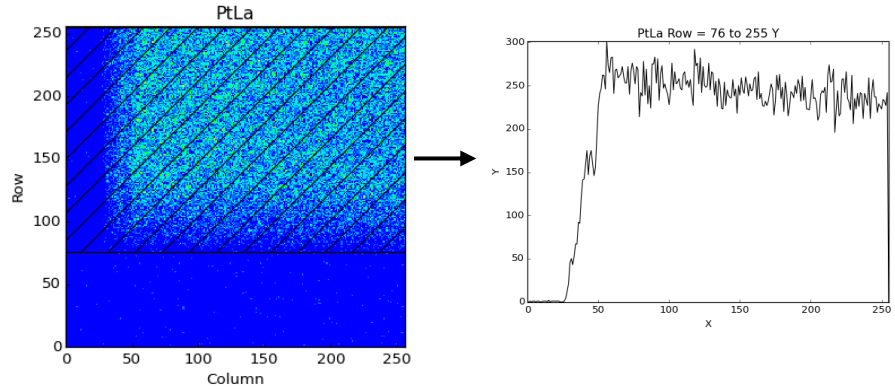

Figure 5-10. Intensity map (left) and the generated Kossel curve (right) of Pt Lα.

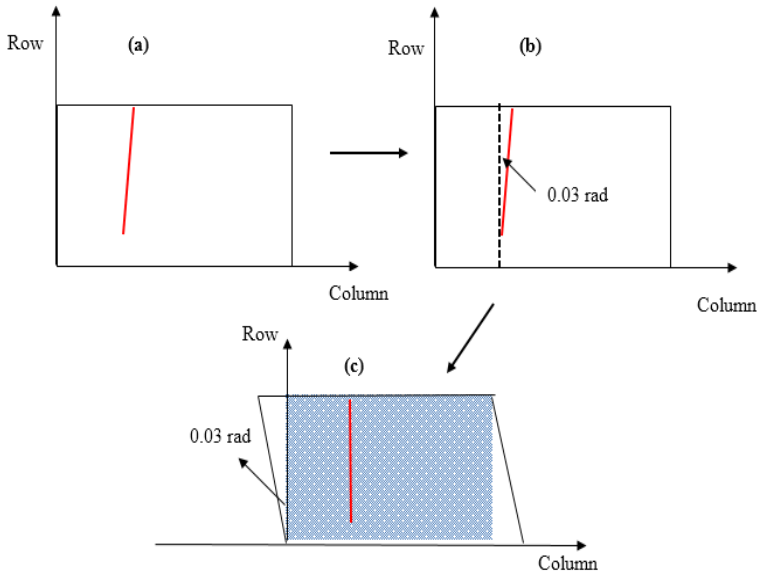

Figure 5-11. Data treatment diagram of the generated signals.

So we make an adjustment of the signals. The process is shown in Figure 5-11. The deviation angle is firstly measured and then we make a coordinate transform using a specially written Python program (see the Annex). The marked regions (as shown in the bottom of Figure 5-11) are chosen for generating the Kossel curves. The experimental Kossel curves with and without angle corrections are shown in Figure 5-12. The correction procedure increases the intensity of the maximum peak. In addition, as exhibited in Figure 5-12 (a), the correction also narrows the FWHM of the Fe Kα peak (about 10.1 pixels before and 8.15 after). The data treatment is applied for all the stacks.

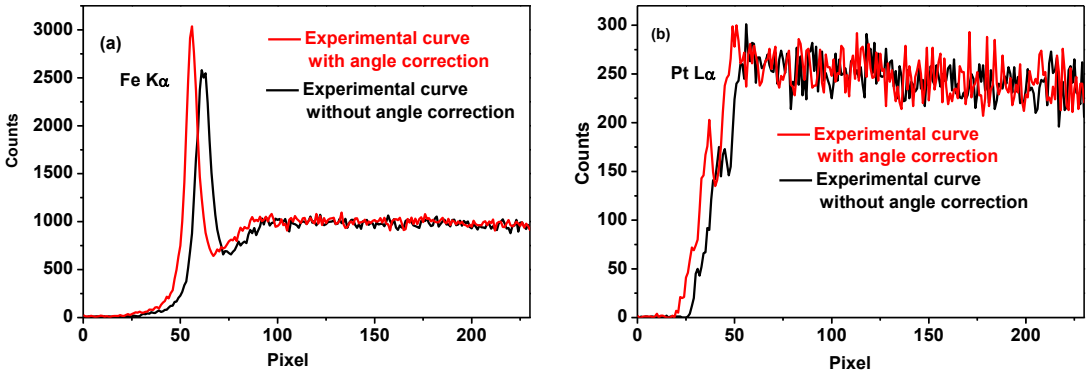

Figure 5-12. Experimental Kossel curves before and after correction, (a) Fe Kα, (b) Pt Lα.

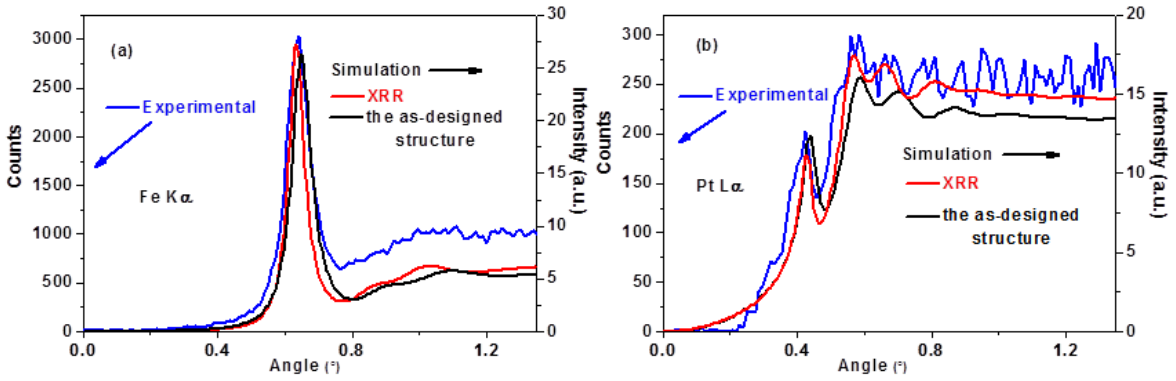

Figure 5-13. Comparison of the experimental (blue line) and simulated Fe Kα (a) and Pt Lα (b) Kossel curves of the PFP-1 stack. Simulated curves are obtained with the parameters both from the designed structure and from the structure fitting the XRR measurements (Table 5-1).

As an angular calibration is missing, we shift one experimental Kossel curve so that its main peak is at the same angle as the simulated one. The same shift is applied for all the other Kossel curves. The simulated Kossel curves of the as-designed structure Pt(4 nm)/Fe(6 nm)/Pt(10 nm), and of that having the structure given in Table 5-1 are shown in Figure 5-13. For Fe Kα, the curves present one main peak while the simulated curves of Pt Lα show two main peaks. It is noticed that the main peaks of Fe Kα and Pt Lα Kossel curves appear at

about 0.6° and 0.4° respectively, which are corresponding to the waveguide modes (as shown in Figure 5-5). Small shifts of the main peaks are observed between the two simulations. We find that the main experimental features are almost reproduced by the simulated XRR curves. However, for the Fe Kα Kossel curve, the intensity toward higher angles has obvious difference, indicating that the description of the stack should be modified. The above results demonstrate that it is not enough to characterize the stack only according to the XRR fitting result: the elemental distribution of the emitting elements should also be considered.

Composition variation of the stack is then considered to improve the fit. In Ref. [109], magneto-optical spectra of Pt/Fe multilayers were investigated. The comparison of the simulation and the experiment confirmed the formation of $Pt_{69}Fe_{31}$ alloy layer at the Pt-Fe interface. As a result, to improve the fitting result for the PFP-1 stack, the presence of the interfacial compound $Pt_{69}Fe_{31}$ is taken into account at both Pt-on-Fe and Fe-on-Pt interfaces. The reflectivity curve and corresponding fit are presented in Figure 5-14.

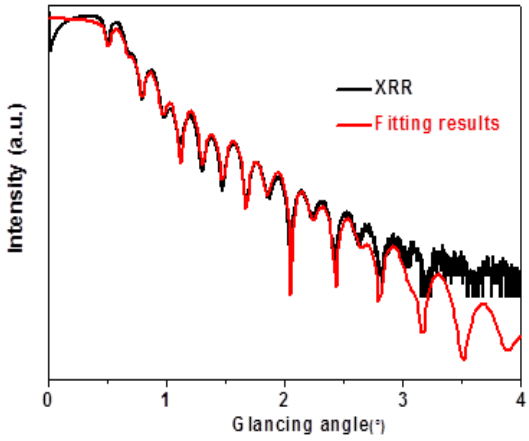

Figure 5-14. Measured (black line) and fitted (red line) XRR curves of the PFP-1 stack accounting for the presence of $Pt_{69}Fe_{31}$ interlayers at both interfaces.

The geometrical information of the stack obtained from the modified fit is listed in Table 5-2. It is also noticed that the thickness and roughness of $Pt_{69}Fe_{31}$ at the Pt-on-Fe interface are different to those at the Fe-on-Pt interface, indicating that the interfaces are asymmetrical. Based on the obtained structure information (Table 5-2), the Fe Kα and Pt Lα Kossel lines are simulated and then compared with the experimental ones. Figure 5-15 shows the revised PIXE-Kossel simulations. The simulated XRR curves with the introduction of $Pt_{69}Fe_{31}$ interlayers show a better agreement with the experimental ones than the previous simulations (Figure 5-13).

Table 5-2. Fitted values from XRR measurements of thickness, roughness and density of the different layers in the PFP-1 stack (listed from the top layer to the substrate) accounting for the presence of $Pt_{69}Fe_{31}$ interlayers at both interfaces.

	Thickness/Roughness (nm) (±0.05 nm)	Density (g/cm^3)
Pt	3.83/0.57	bulk
$Pt_{69}Fe_{31}$	1.62/0.90	16±2
Fe	5.19/1.20	bulk
$Pt_{69}Fe_{31}$	1.41/0.79	16±2
Pt	10.25/0.39	bulk
Si substrate	bulk/0.50	bulk

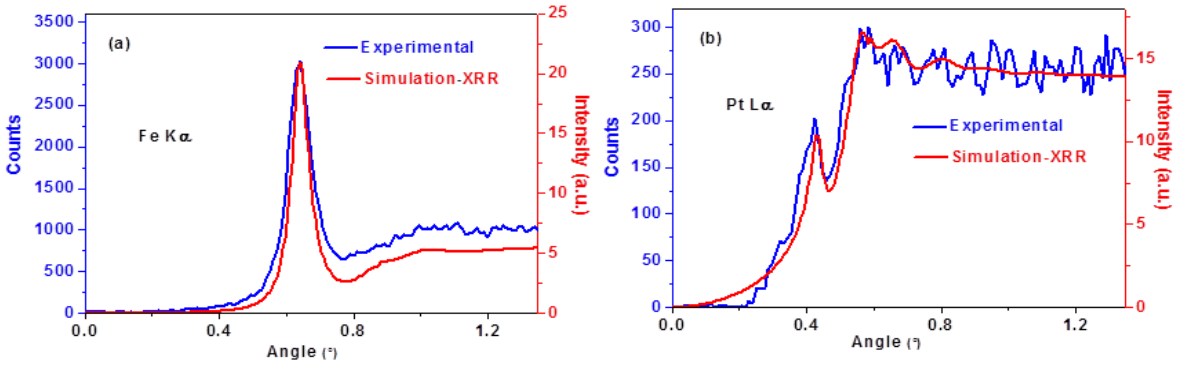

Figure 5-15. Comparison of the experimental and revised simulated Fe Kα (a) and Pt Lα (b) Kossel curves of the PFP-1 stack.

5.5.2.2 Analysis of Pt (4 nm)/Fe (8 nm)/Pt (10 nm) film waveguide

As discussed in previous section, based on the comparison of the experimental Kossel curves and the simulated ones, we find that interfacial compound is formed in the PFP-1 stack. Hence $Pt_{69}Fe_{31}$ is also considered in the XRR fit of PFP-2 stack. The measured and fitting XRR curves are shown in Figure 5-16. The fitting curve matches well with the measured one. The corresponding information obtained from the fitting process is displayed in Table 5-3. With respect to the previous sample, a departure of the Fe density from bulk has to be considered. According to the fitted thicknesses (shown in Table 5-3), the $Pt_{69}Fe_{31}$ interlayers on Pt-Fe and Fe-Pt interfaces are also different, indicating the two interfaces are asymmetrical. With respect to PFP-1 stack, the thickness difference of $Pt_{69}Fe_{31}$ interlayers on Pt-Fe and Fe-Pt interfaces increases.

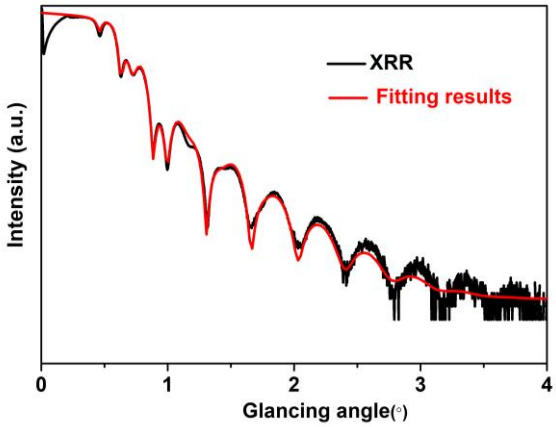

Figure 5-16. Measured (black line) and fitted (red line) XRR curves of the PFP-2 stack accounting for the presence of $Pt_{69}Fe_{31}$ interlayers at both interfaces.

Table 5-3. Fitted thicknesses, roughnesses and densities of the films in the PFP-2 stack (listed from the top layer to the substrate).

	Thickness/Roughness (nm) (±0.05 nm)	Density (g/cm^3)
Pt	4.20/1.29	Bulk
$Pt_{69}Fe_{31}$	2.06/0.92	16±2
Fe	7.89/1.72	6.6±1
$Pt_{69}Fe_{31}$	0.57/0.42	16±2
Pt	10.79/0.83	Bulk
Si substrate	0.67	Bulk

Then we perform the PIXE-Kossel experiment to obtain the Kossel curve. The X-ray emission spectrum, energy calibration and ROI selection are similar to the one of the PFP-1 stack. Figure 5-17 displays the comparison of the experimental and simulated Fe Kα and Pt Lα Kossel curves. Similar to PFP-1, the curves present one main peak for Fe Kα and two main peaks for Pt Lα. For both Kossel curves, the main features are well reproduced. However, there is still a discrepancy regarding their relative intensities. With respect to PFP-1 stack, the shapes of the Kossel curves are basically consistent. Due to the Fe density variation and thickness difference of $Pt_{69}Fe_{31}$ interlayer from the XRR fit, the relative peak-back intensity of PFP-2 stack differs a little compared to PFP-1 stack. From Figure 5-15 and 5-17, for the PFP-1 and PFP-2 stacks, differences still exist between Fe experimental and simulated Kossel curves at higher angles, which derive from the density and composition of Pt_xFe_y intermixing layers. It is difficult to define the exact composition and density of the formed Pt_xFe_y intermixing layer without an efficient fitting code of Kossel curves. However, in XRR

measurements of PFP-1 and PFP-2 stack, the spectra are acquired by varying the incident angle in the grazing incidence regime while detecting the specular reflected X-ray beam. This technique uses the average electron density of a layer and thus cannot provide information on the elemental composition. By the combination of XRR and PIXE-Kossel, it is convenient to know whether intermixing occurs.

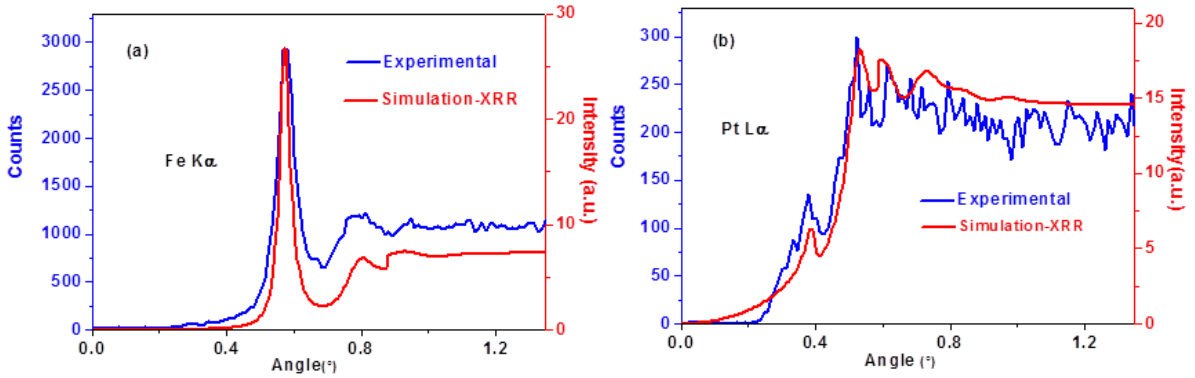

Figure 5-17. Comparison of the experimental and simulated Fe Kα (a) and Pt Lα (b) Kossel curves of the PFP-2 stack.

5.5.2.3 Analysis of Ta(4 nm)/Cr(10 nm)/Pt (12 nm) waveguide

Figure 5-18 shows the measured and fitted XRR curves of the TCP stack. It is difficult to obtain a good fit if no oxidation of the designed structure (Ta/Cr/Pt) is considered. Owing to the protective ability of Ta_2O_5 compound against oxidization [110, 111], the Ta_2O_5/Cr/Pt structure is firstly considered. Again, fitting remains difficult if no oxidation of Cr is considered. It is reported that Cr_2O_3 (the oxidation product of Cr) also possesses good corrosion resistance, which is usually used for the protection of components operating in harsh chemical environments [112].

So the Ta_2O_5/Cr_2O_3/Cr/Pt structure is then taken into consideration. It is observed that although some intensity discrepancies exist, the fit is well aligned with the measured XRR data. The obtained structural parameters of the stack are listed in Table 5-4. The fitted thickness of Ta_2O_5 layer is almost two times higher than that of the original Ta layer. This can be attributed to its lower density (bulk densities of Ta and Ta_2O_5 are 16.65 [61] and 8.2 g/cm^3 [113] respectively). Compared with Cr (bulk density of 7.19 g/cm^3), the bulk density Cr_2O_3 (5.21 g/cm^3 [61]) does not change too much. As a result, the sum of the fitted thicknesses of Cr_2O_3 and Cr layers is almost equal to the designed Cr layer thickness. From the fitted results,

we note that the oxidation of the stack is major (total for Ta and partial for Cr), so that the studied stack differs substantially from the designed structure.

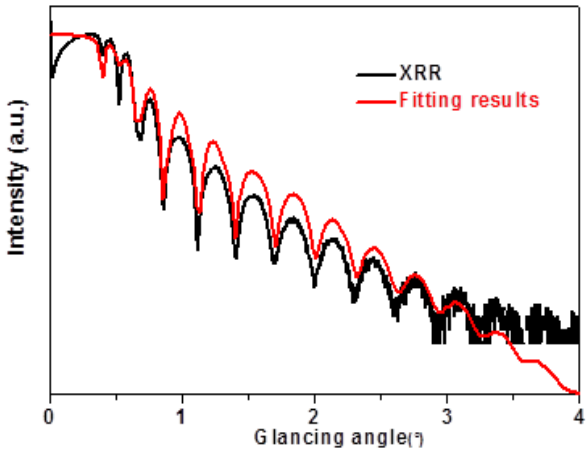

Figure 5-18. Measured (black line) and fitted (red line) XRR curves of the TCP stack.

Table 5-4. Fitted values from XRR measurements of thickness, roughness and density of the different layers in the TCP stack (listed from the top layer to the substrate).

	Thickness/Roughness (nm) (±0.05 nm)	Density
Ta_2O_5	7.87/1.09	bulk
Cr_2O_3	6.55/1.30	bulk
Cr	4.54/0.80	bulk
Pt	13.79/0.54	bulk
Si substrate	bulk/0.67	bulk

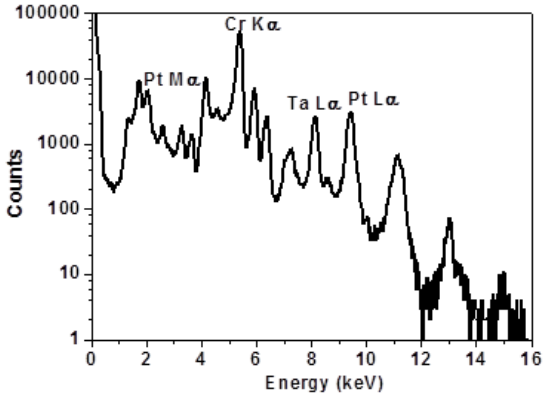

Figure 5-19. X-ray emission spectrum of the TCP stack summed over all the pixels of the CCD camera.

Figure 5-19 shows the overall X-ray emission spectrum. The photon energy is calibrated from the positions of the Cr Kα, Ta Lα and Pt Lα emissions. Other peaks can be ascribed to the fluorescence of the impurities inside the sample or of the experimental setup. To extract the Cr Kα, Ta Lα and Pt Lα Kossel curves, we select ROI on the overall spectrum (shown in Figure 5-20).

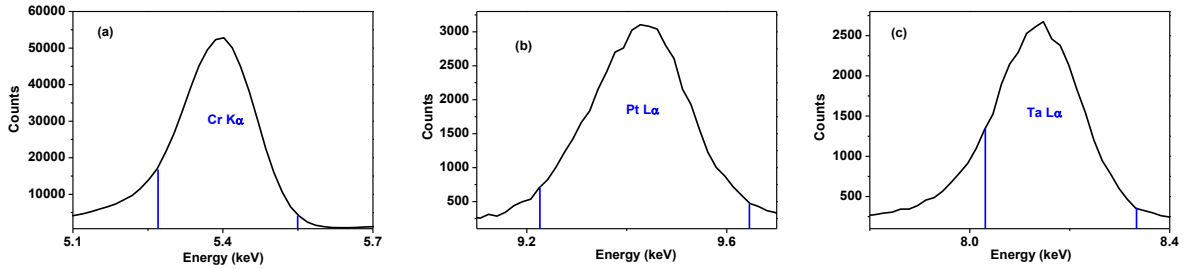

Figure 5-20. Cr Kα (a), Pt Lα (b) and Ta Lα (c) ROI selected on the X-ray emission spectrum of TCP stack.

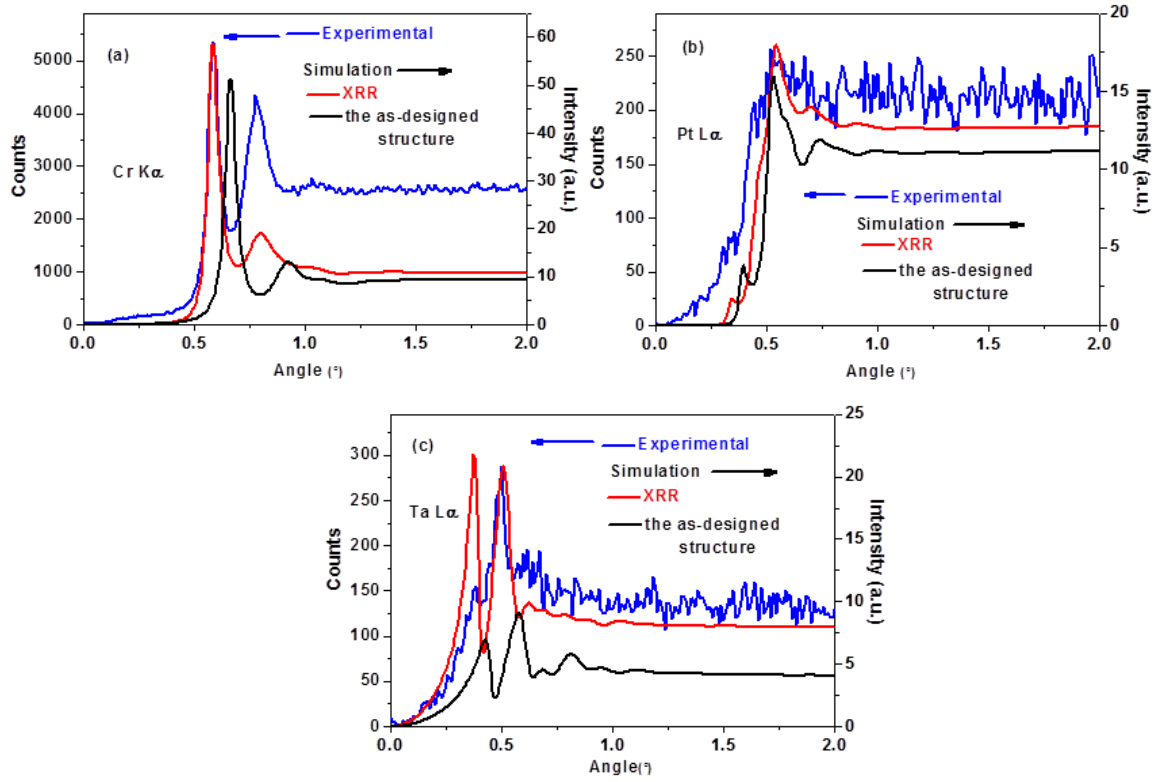

Figure 5-21. Comparison of the experimental and simulated (see Table 5-4) Cr Kα (a), Pt Lα (b) and Ta Lα (c) Kossel curves.

Based on the structure obtained from XRR (Table 5-4), Kossel curve simulations are performed (shown in Figure 5-21), which are also compared with the as-designed structure and the experiment. It is clearly seen that the as-designed structure cannot reproduce the

experiment since large angular shifts and intensity discrepancies exist. The experimental Pt Lα curve shows a reasonable agreement with the simulated one deduced from the XRR fit including oxidization effect. However, for the Cr Kα and Ta Lα curves, the relative intensities of the main features still exhibit obvious differences.

Since only introducing the oxidation of the stack does not allow fitting the experimental Kossel curves, we now study the possibility of compound formation. Due to the negative standard Gibbs energy of the reaction calculated with the HSC software [114] (Ta (s) + 2Cr (s) = $TaCr_2$ (s), ΔG = -26.83 kJ/mol at 25°C [84, 115]), we then assume that $TaCr_2$ is possibly formed between the Ta and Cr layers during the deposition process. Oxidation of the stack is then assumed when the sample is transferred in air. It has been reported that $CrTaO_4$ possesses good protective ability, which could decrease the oxidation rate of the underlying alloys [116, 117]. So the new stack description, $CrTaO_4/TaCr_2/Cr/Pt$, is applied in the XRR fitting process. The corresponding reflectivity curve and its fit are displayed in Figure 5-22.

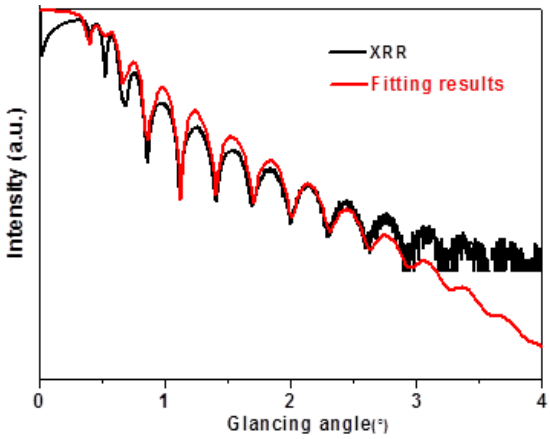

Figure 5-22. Measured (black line) and fitted (red line) XRR curves of the TCP stack accounting for the compound formation and subsequent oxidation.

The structure parameters of the stack extracted from the fit are shown in Table 5-5. The obtained structure differs greatly from the as-designed structure and also from the previously considered oxidized stack (Table 5-4). Compared with the as-designed structure, the stack thickness change (Table 5-5) can be explained by the density variation of the layers. Based on the conservation of mass, when the designed Ta layer is consumed totally for the $TaCr_2$ formation, the thickness of the $TaCr_2$ layer will be 13.1 nm and the residual thickness of the Cr layer will be 4.7 nm. So the total thickness of $TaCr_2$ and Cr will be 17.8 nm (if no oxidation is considered). When oxidation occurs, because the fitted density difference of

$CrTaO_4$ and $TaCr_2$ is small, the sum of the fitted thickness of $CrTaO_4$, $TaCr_2$ and Cr only changes a little, which is 18.7 nm.

Table 5-5. Fitted values from XRR measurements of thickness, roughness and density of the different layers in the TCP stack (listed from the top layer to the substrate) accounting for the compound formation and subsequent oxidation.

	Thickness/Roughness (nm) (±0.05 nm)	Density (g/cm^3)
$CrTaO_4$	10.75/1.10	6±1
$TaCr_2$	3.96/1.32	8±1
Cr	4.02/0.53	bulk
Pt	13.79/0.54	bulk
Si substrate	bulk/0.69	bulk

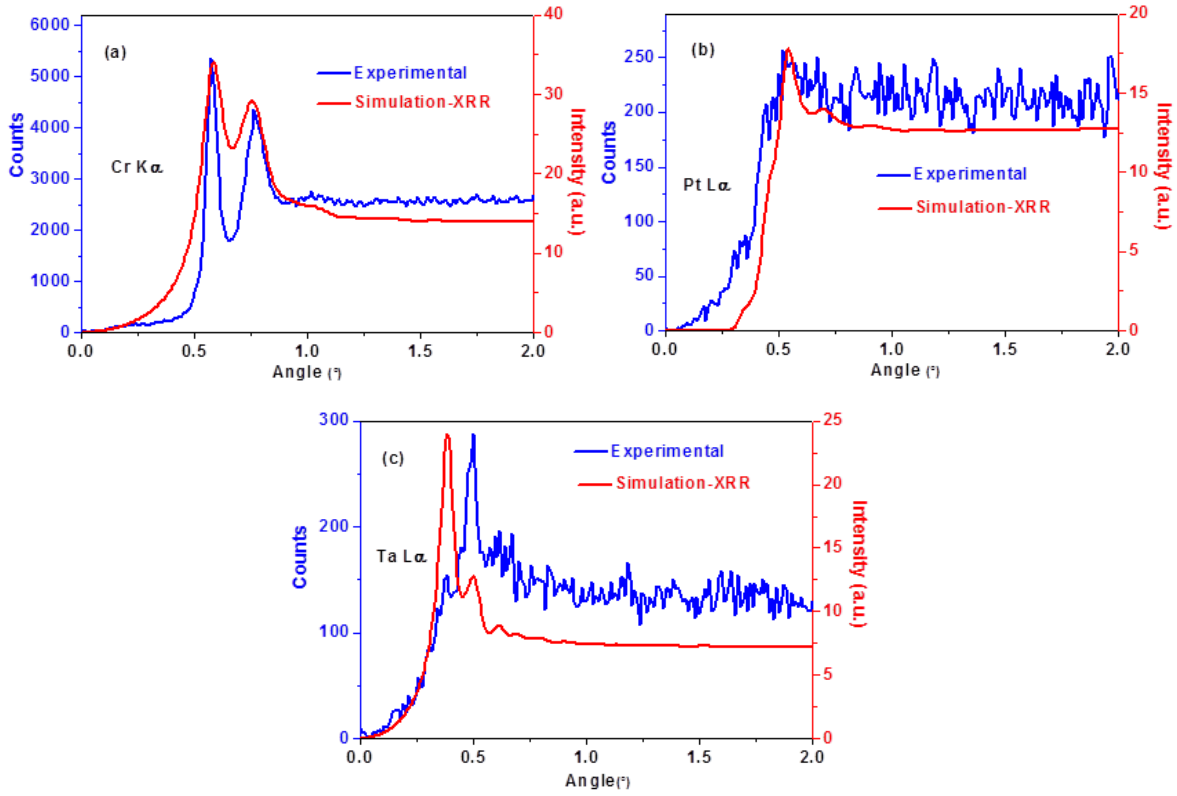

Figure 5-23. Comparison of the experimental and revised simulated (see Table 5-5) Cr Kα (a), Pt Lα (b) and Ta Lα (c) Kossel curves.

Figure 5-23 shows the revised PIXE-Kossel simulations, which improve significantly, compared with the simulation curves in Figure 5-21. Especially for Cr Kα, the relative intensities are much closer to the experimental ones. Hence, according to the XRR (Figure 5-22) and the Kossel (Figure 5-23) results, it is anticipated that the new designed structure is close to the real structure of the TCP stack. However, a refinement of this structure is still in

need to reach an even better fit of the Kossel curves. Particularly the large discrepancy for the Ta curve probably originates from a wrong number and depth distribution of the Ta atoms. The non-uniform Ta depth distribution makes it more difficult to improve the result. Precise definition of the angular calibration would be also helpful to decrease the uncertainty.

5.6 Design and simulation of the HfC/SiC/HfC multilayers

Owing to the successful implementation of the PIXE-Kossel methodology, we then build a waveguide made in multilayer ceramic coating. Instead of Si substrate, we use graphite (representing the C/C) the substrate. Because SiC and HfC possess a synergetic effect against oxidation, we try to see if it is possible to construct a waveguide mode in HfC/SiC/HfC. The results are shown in Figure 5-24.

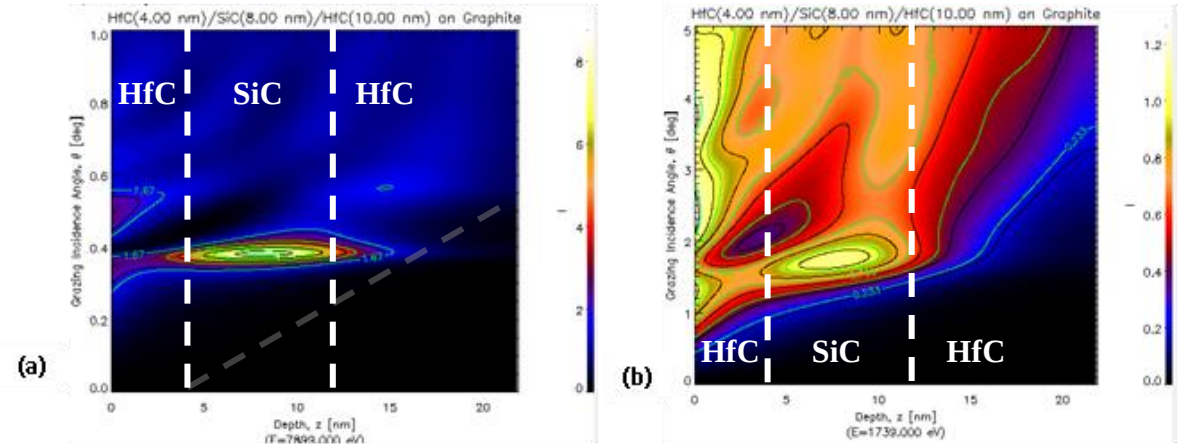

Figure 5-24. Simulated depth and angular distribution of the electric field in the HfC/SiC/HfC multi-layer at the photon energy corresponding to (a) the Hf Lα emission (7899 eV), (b) the Si Kα emission (1739 eV). The vertical color bar gives the intensity scale of the electric field.

It is clearly seen that waveguide modes are formed in the SiC layer (guiding layer) at glancing angles around 0.4° and 1.8° for the Hf Lα and Si Kα emissions. This means that when the angles of detection are equal to these angles, an intensity maximum is expected for the corresponding emission. So in actual application of the HfC/SiC/HfC multilayers, we could use the PIXE-Kossel method to evaluate its service reliability. When the microstructure of the stack changes, the Kossel curve will change accordingly. Take oxidation of the stack as an example, the Kossel curves before and after oxidation are shown in Figure 5-25. When oxidation occurs, the peak maxima shift a little toward low angles, and the intensity difference of peak-background increases. So in actual applications, based on the comparison of experimental/simulation Hf Lα and Si Kα Kossel-curves of the HfC/SiC/HfC stack, it is convenient to know its oxidation process and evaluate its service reliability.

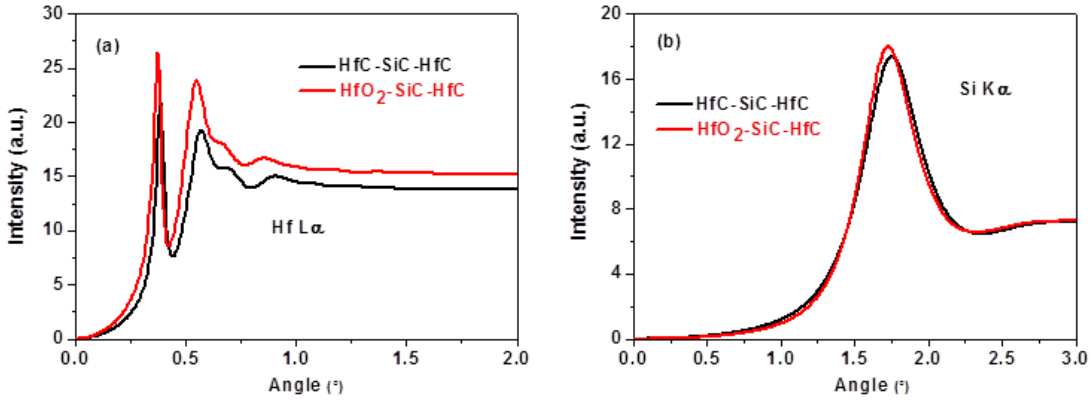

Figure 5-25. The simulated Kossel curves before and after oxidation, (a) Hf Lα, (b) Si Kα.

5.7 Conclusions

1. We have studied the feasibility of observing and exploiting proton-induced X-ray emission in Kossel geometry in stacks consisting of only a few layers. Here Pt/Fe/Pt and Ta/Cr/Pt nano-scale tri-layers were designed as X-ray planar waveguides. In the waveguide configuration, owing to the high sensitivity of the electric field versus the detection direction of the emitted radiation, PIXE-Kossel curves are sensitive to the depth distribution of the emitting atoms. In addition, the prepared stacks were also investigated by grazing incident X-ray reflectometry.

2. For all systems, the as-designed parameters (thickness, roughness and density of the layers) fail to simulate both XRR and PIXE-Kossel experimental curves. It is always possible to find a structure able to reproduce the XRR curve, by considering some oxidation or the formation of some interfacial compound for example, but then the PIXE-Kossel curve simulations still differ markedly from the experimental ones. To get a satisfying agreement between experiment and simulation for both XRR and PIXE-Kossel curves, we had to consider that interlayers form at the interfaces of the Pt/Fe/Pt waveguide, while in the Ta/Cr/Pt system, some intermixing takes place between the Ta and Cr layers to form a compound, which is subsequently partly oxidized. This work demonstrates the ability of the PIXE-Kossel methodology to characterize the stacks of nano-scale thin films.

3. We could build a waveguide mode in HfC/SiC/HfC multilayer for C/C composites, and significant changes can be observed on the Hf Lα and Si Kα Kossel curves when oxidation occurs on the stack. In future work, PIXE-Kossel methodology is promising to be used as a non-characterization method to evaluate the service reliability of the multilayer for C/C.

Chapter 6: HfB_2 and HfB_2-SiC modified C/C composites

Thermal protection systems, which are operated in the extreme environments above 2000°C, arise wide concerns [26, 27, 118]. Therefore, materials with outstanding thermo-mechanical and thermochemical properties are required. In such harsh conditions, traditional alloys and monolithic ceramics are difficult to meet the requirements [8]. In chapters 3 and 4, Si-based ceramic coatings (Si-Mo-Cr, HfC-SiC and ZrB_2-SiC) were prepared on the surface of blasting-treated C/C composites. Their cyclic ablation performances were efficiently improved due to the inlaid coating/substrate interface. However, because of the poor thermal stability of SiO_2 glass, the coatings easily failed at much higher temperature. Instead of preparing protective coating, the addition of UHTCs into C/C is a good approach to solve the problems. With the incorporation of UHTCs, the materials are expected to possess good chemical stability in oxidizing environment and sufficient thermal shock resistance in high-low cyclic temperature condition [14, 24, 29, 30]. So in this chapter, HfB_2 and HfB_2-SiC are introduced into C/C to enhance its oxidation/ablation performance.

6.1 HfB_2 modified C/C composites

6.1.1 Introduction

In this section, C/C-HfB_2 composites are firstly prepared by PIP, and then densified by pyrolysis carbon through CVI. Ablation behavior of the prepared C/C-HfB_2 (C/C-HB) composites is investigated using an oxyacetylene torch with different heat fluxes (2.38 and 4.18 MW/m^2). Ablation time was 90 s. For the convenience of discussion, C/C-HB composites ablated in the heat fluxes of 2.38 and 4.18 MW/m^2 are marked as C/C-HB-L and C/C-HB-H, respectively. Thermo-gravimetric (TG) analysis is carried out to illustrate the effect of HfB_2 addition on the oxidation resistant property of C/C composites.

6.1.2 Microstructure and ablation test

Figure 6-1 displays the morphology and XRD pattern of the formed ceramics from the HfB_2 precursor after heat treatment. It is found that the ceramics present a granular structure (Figure 6-1 (a)), and some micro-cracks as well as micro-pores owing to the shrinkage of ceramics when they cool down from heat-treatment temperature to room temperature. The main phase of the ceramics is HfB_2 with a little amount of HfC (Figure 6-1 (b)).

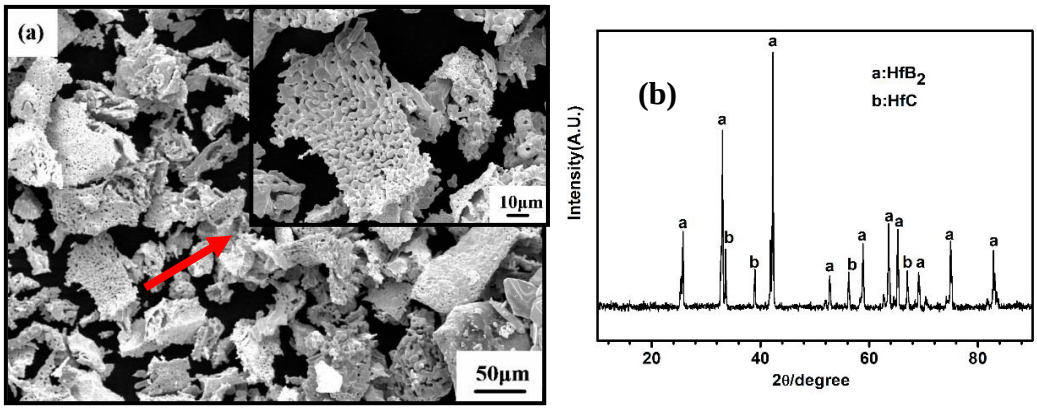

Figure 6-1. Surface morphology (a) and XRD pattern (b) of the formed HfB_2 ceramics from hafnium boride precursor.

Figure 6-2 shows the microstructure of the prepared C/C-HB composites after PIP. The HfB_2 ceramic particles (white and small particles) are successfully introduced into C/C composites, which mainly distribute in the short-cut fiber webs among the non-woven webs. The short-cut fiber webs consist of some micro-pores (Figure 6-2 (a)). As seen in the enlarged view of Figure 6-2 (a), some small gaps among carbon fibers can be also observed, and the HfB_2 particles mainly attach on the surface of pyrolysis carbon layer (Figure 6-2 (b)).

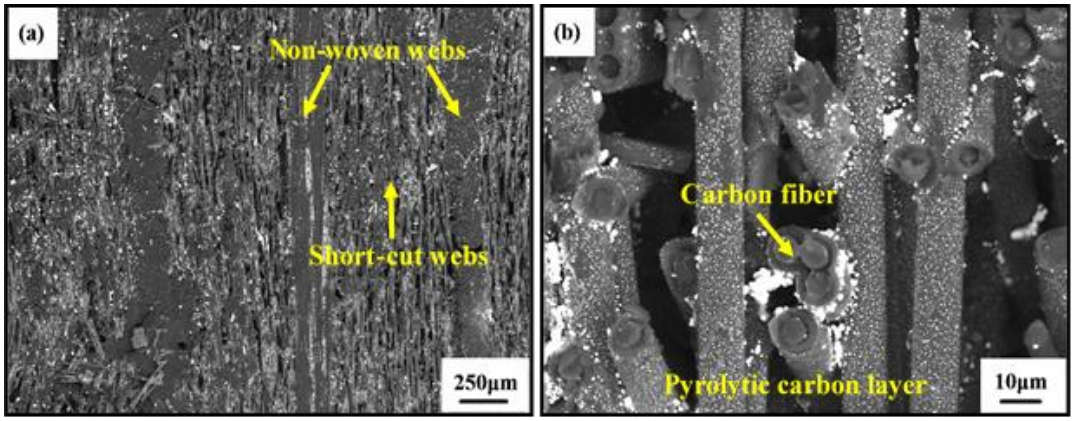

Figure 6-2. Microstructure of the C/C-HB composites after PIP process,
(a) low-magnification, (b) high-magnification.

The pores and gaps are expected to be filled by pyrolysis carbon in the next TCVI densification process, as shown in Figure 6-3. The pores (Figure 6-3 (a)) in the short-cut fiber webs and the small gaps (Figure 6-3 (b)) among carbon fibers are filled by the pyrolysis carbon.

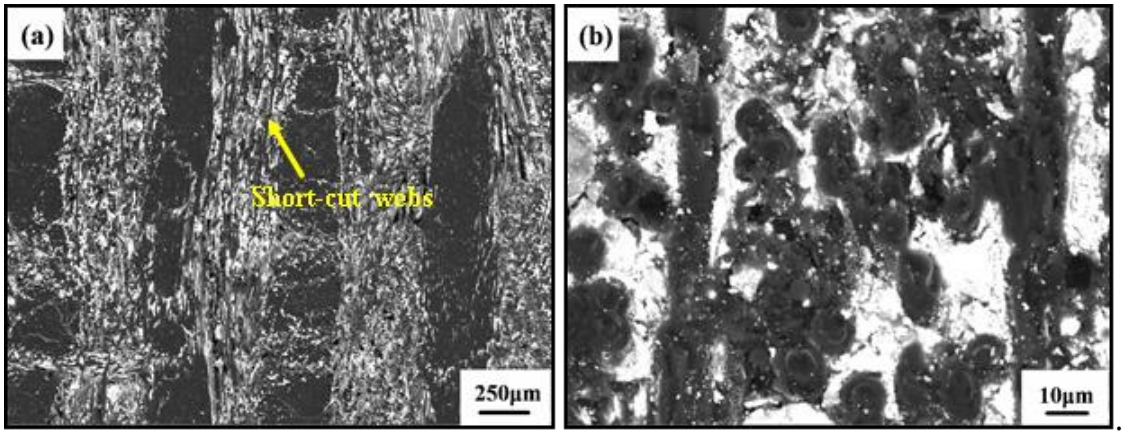

Figure 6-3. Microstructure of the C/C-HB composites after TCVI densification, (a) low-magnification, (b) high-magnification.

To investigate the effect of HfB_2 addition on the oxidation properties of C/C composites, TG analysis of bare C/C and C/C-HB is carried out in air, as shown in Figure 6-4. We clearly observe that C/C composites exhibit poor oxidation resistance: C/C composites loss mass at temperatures higher than 520ºC. With a further increase of test temperature, the mass loss increases quickly and reaches 82% at 900°C. Compared with the C/C composites, C/C-HB composites possess better oxidation resistance, which begin to loss mass at about 755ºC. When the test temperature reaches 1000 ºC, the mass loss percentage is just about 45%.

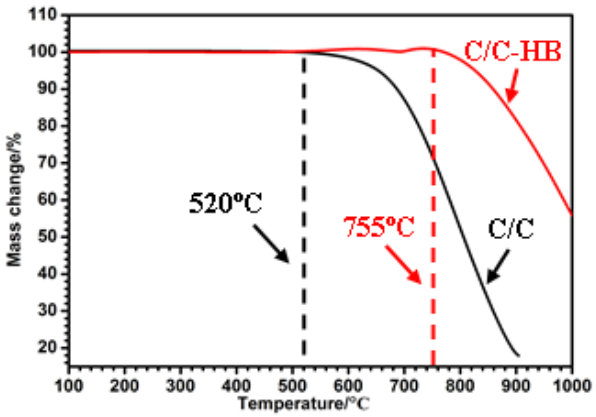

Figure 6-4. TG analysis of C/C and C/C-HB composites performed in air condition.

Figure 6-5 shows the experimental setup of the ablation test and the macroscopic images of the C/C-HB-L and C/C-HB-H samples after ablation. The oxyacetylene flame is applied in vertical direction to the sample, and the center region of the sample suffers the most severe combustion gas erosion. After ablation for 90 s, the linear ablation and mass ablation rates of C/C-HB-L are 3.14×10^{-3} mm/s and 0.86 $mg\cdot s^{-1}$, respectively. Compared to the C/C-HB-L, ablation performance of C/C-HB-H is degraded, and the corresponding linear ablation and

mass ablation rates are 6.56×10^{-3} mm/s and 1.94 mg·s^{-1}. But compared with the ablation properties of bare C/C composites measured in the same conditions [119], C/C-HB-L and C/C-HB-H both exhibit better ablation performance. After ablation, the surfaces of C/C-HB-L and C/C-HB-H are covered by ablation products and present different colors according to their distance from the center of the flame (Figure 6-5).

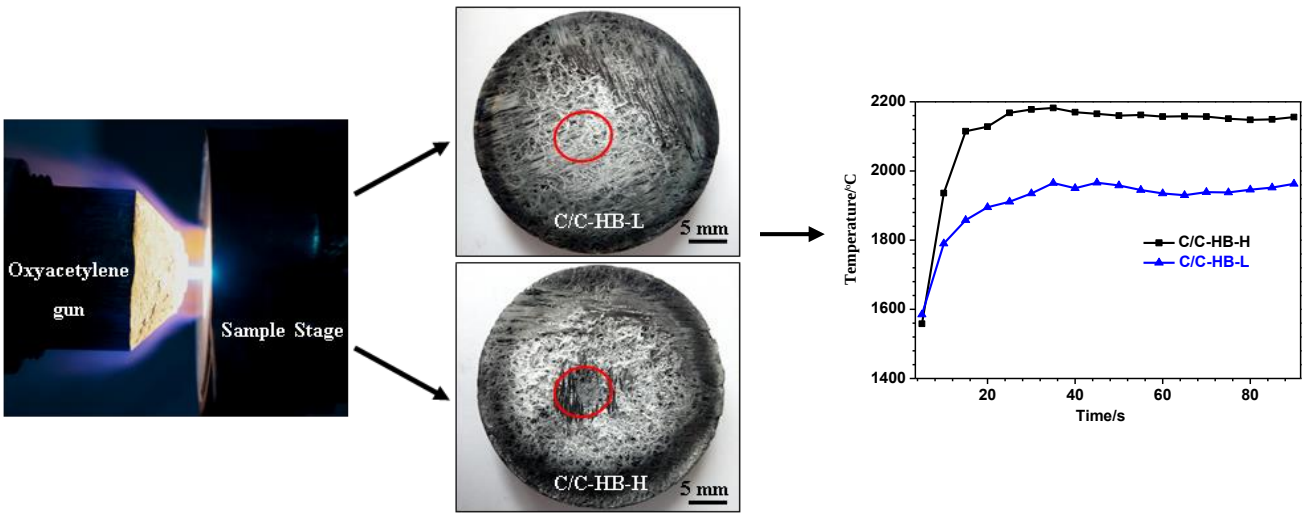

Figure 6-5. Experimental setup of the oxyacetylene torch (left) during ablation. Macroscopic images (middle) of the C/C-HB-L and C/C-HB-H after ablation. Surface temperature curves (right) of the center regions of C/C-HB-L and C/C-HB-H during ablation

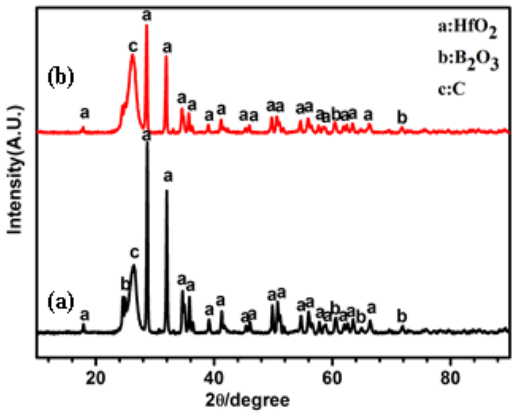

Figure 6-6. XRD pattern of the composites after ablation, (a) C/C-HB-L, (b) C/C-HB-H.

Phase composition determined by XRD are shown in Figure 6-6. The phase compositions of both C/C-HB-L and C/C-HB-H are the same, which mainly consist of HfO_2, B_2O_3 and C. HfO_2 and B_2O_3 are formed by the oxidation of HfB_2. The formation of B_2O_3 is beneficial for the improvement of oxidation resistance. Figure 6-7 shows the surface morphologies of the center regions of C/C-HB-L and C/C-HB-H after ablation. As for the

C/C-HB-L, according to the XRD pattern (Figure 6-6), a relatively dense and continuous HfO_2 layer along with a few pores covers the surface, which acts as a good barrier to heat transfer and denudation by the oxyacetylene torch. As the heat flux increases to 4.18 MW/m^2, the formed HfO_2 layer is peeled off partially and carbon fibers can be observed (Figure 6-5 and 6-7 (b)).

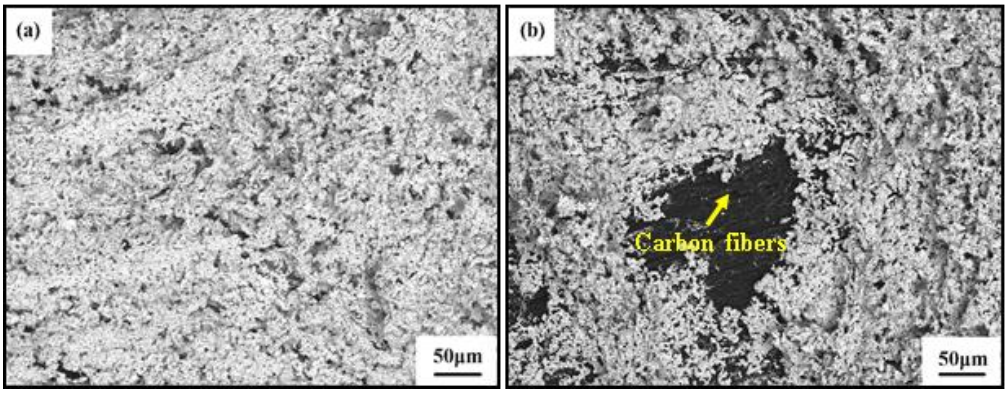

Figure 6-7. Surface morphologies of the center region of C/C-HB composites after ablation, (a) C/C-HB-L, (b) C/C-HB-H.

6.1.3 Oxidation and ablation mechanism

TG analysis of C/C-HB composites was carried out in air condition, so the following reactions could take place [120].

$$\frac{2}{5}HfB_2(s) + O_2(g) = \frac{2}{5}HfO_2(s) + \frac{2}{5}B_2O_3(g) \quad (6\text{-}1)$$

$$2C(s) + O_2(g) = 2CO(g) \quad (6\text{-}2)$$

$$C(s) + O_2(g) = CO_2(g) \quad (6\text{-}3)$$

Figure 6-8 shows the standard Gibbs free energy of the aforementioned reactions calculated by HSC software [84, 85, 114] . The lower the standard Gibbs free energy, the greater tendency of a chemical reaction to occur. So at the initial stage of oxidation (Figure 6-5), although the oxidation of C will lead to mass decrease (reactions 6-2 and 6-3)), the mass gain of the C/C-HB composites can be mainly attributed to the oxidation of HfB_2. Then the formed oxidation product B_2O_3 can further improve the oxidation resistant property of the composites due to its good self-sealing performance. So compared with C/C composites, C/C-HB composites possess better oxidation resistance. However, with the increase of test temperature, the volatilization of B_2O_3 (as shown in Figure 6-9) weakens its protective ability, which results in the significant degradation of the oxidation performance of C/C-HB composites.

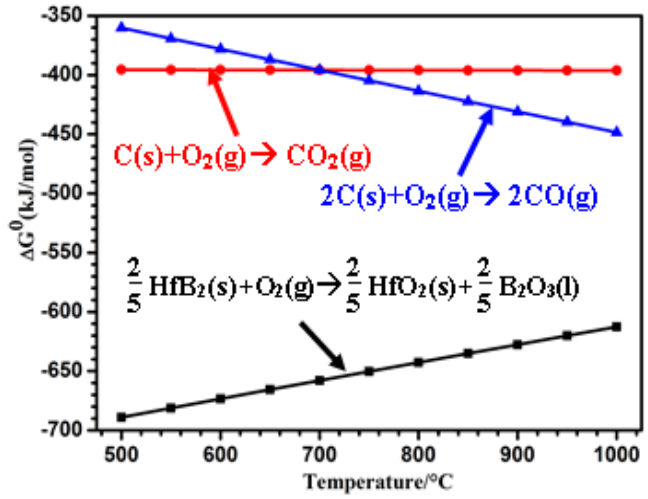

Figure 6-8. Standard Gibbs free energies of reactions (6-1) -(6-3) at different temperatures.

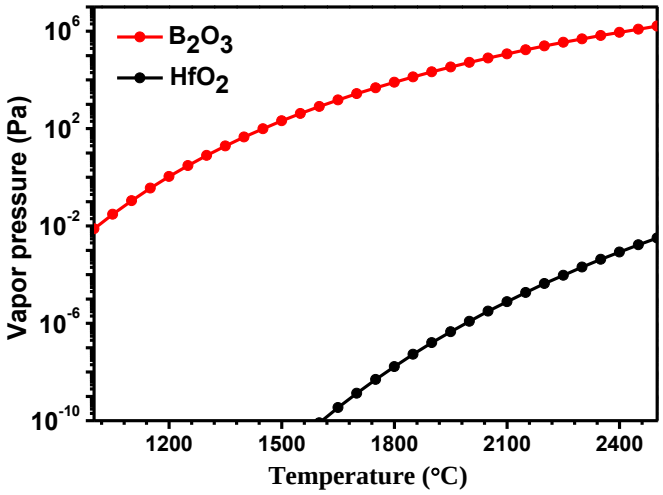

Figure 6-9. Vapor pressure vs temperature for B_2O_3 and HfO_2 calculated at ambient pressure (Vapor pressure in logarithmic scale).

From the measured surface temperature curves of the ablation center (Figure 6-5), we can find that the surface temperatures of C/C-HB composites rise quickly, and the maximum temperatures of C/C-HB-L and C/C-HB-H are 1960 and 2180ºC, respectively. Based on the TG analysis discussed above, it can be deduced that B_2O_3 will evaporate rapidly at these two high temperatures accompanied with the combustion gas erosion. So the protection ability of B_2O_3 is limited during ablation, and the ablation performance enhancement of C/C-HB composites can be mainly attributed to the formed HfO_2 layer (Figure 6-7). As for the C/C-HB-L composites, the formed HfO_2 layer (Figure 6-7 (a)) could cover the surface and then plays an efficient role in withstanding the heat transfer and denudation by oxyacetylene torch. However, as the heat flux increases to 4.18 MW/m^2, much more thermal energy of the

oxyacetylene torch will be concentrated on the ablated surface of C/C-HB-H composites. With the ablation time prolonging, thermal energy concentration and denudation enhancement of the oxyacetylene torch contribute to the cracking and spalling of the formed HfO_2 protective layer (Figure 6-7 (b)), which thereby results in the performance degradation.

6.2 HfB_2-SiC modified C/C composites

6.2.1 Introduction

Due to the good sealing performance of SiO_2 (the oxidation product of SiC) at high temperature, SiC is usually introduced in C/C-UHTCs to further enhance their oxidation and ablation properties. The addition of SiC into the C/C-HfB_2 is expected to give better performance. PIP is also convenient to achieve near net shape manufacturing and prepare special-shaped samples to simulate thermal structural components [17]. In this section, nose-shaped C/C-HfB_2-SiC (C/C-HS) composites were prepared by PIP. Ablation behavior of the prepared composites is investigated using oxyacetylene torch. For comparison, bare C/C composites are also investigated in the same conditions. Ablation time was 60 s. For the convenience of discussion, C/C-HS and C/C investigated in the heat flux of 2.38 MW/m^2 were marked as C/C-HS-L and C/C-L, respectively. Correspondingly, C/C-HS and C/C ablated in the heat flux of 4.18 MW/m^2 were marked as C/C-HS-H and C/C-H. Based on the analysis of phase compositions and surface morphologies evolutions, the ablation mechanism is discussed.

6.2.2 Microstructure and ablation test

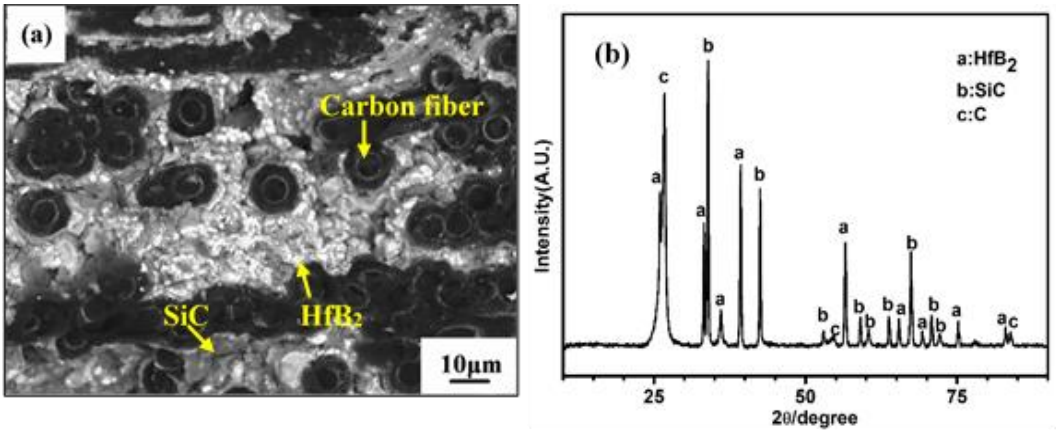

Figure 6-10. Microstructure (a) and phase composition (b) of the fabricated C/C-HS.

Microstructure and phase composition of the fabricated C/C-HS are shown in Figure 6-10. From Figure 6-10 (a), three phases presenting black, gray and white colors are observed.

According to the XRD pattern (Figure 6-10 (b)), the white and gray phases can be distinguished as HfB_2 and SiC, respectively.

Figure 6-11 shows the measured thermal conductivity (TC) of the C/C and C/C-HS at high temperature. It is observed that due to the good thermal conductivity of graphite (TC: 300-500 W/(m·K), C/C possesses higher thermal conductivity than that of C/C-HS. However, compared to graphite, C/C possesses lower TC. This could be explained by phonon interactions (phonon-phonon, phonon-defect and phonon-interface interactions), responsible for the heat conduction. There exists fiber/matrix interface, micro-pores and micro-cracks. They could act as the defects to prevent phonon interactions and enhance the phonon scattering, thereby resulting in the decrease of TC [121].

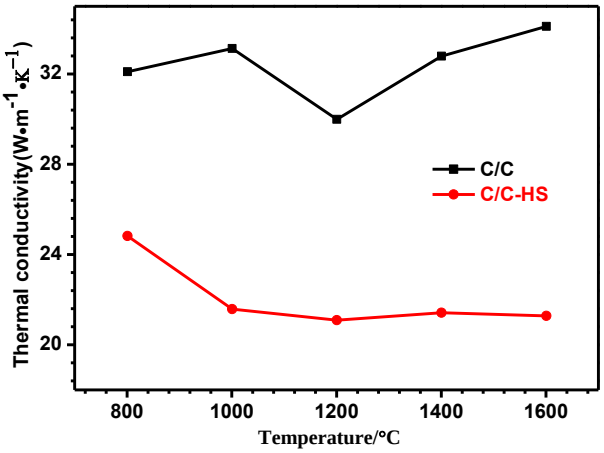

Figure 6-11. Thermal conductivity of the C/C and C/C-HS at high temperature.

As shown in the Figure 6-12, two nose-shaped samples including C/C and C/C-HS were adopted for the ablation test (shown in the left of Figure 6-12). Then the composites underwent ablation using oxyacetylene torch (shown in the right of Figure 6-12).

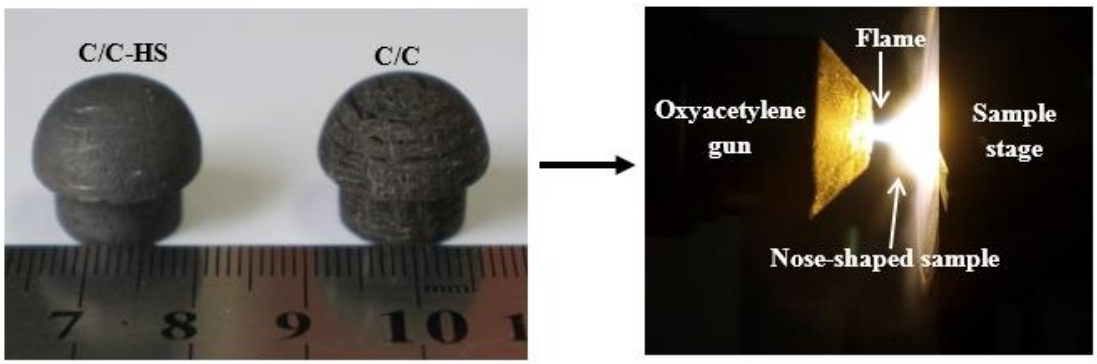

Figure 6-12. Macroscopic image (left) of the fabricated C/C and the C/C-HS and experimental setup (right) of the ablation test using oxyacetylene torch.

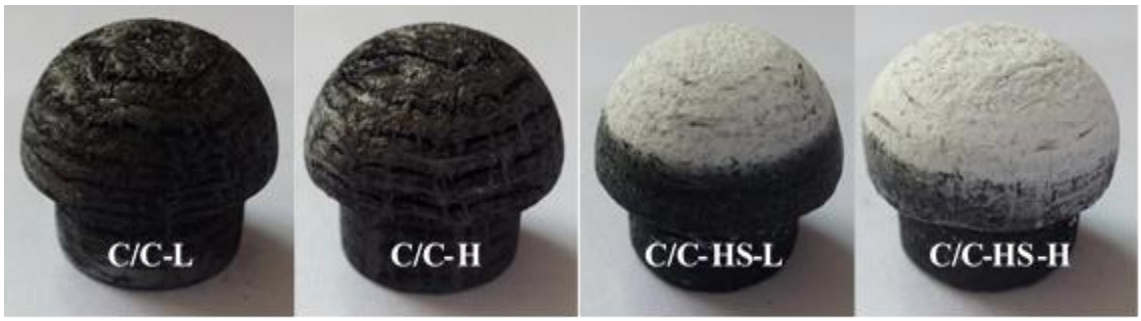

Figure 6-13. Macroscopic images of the C/C and C/C-HS after ablation test.

Table 6-1. Ablation properties of C/C and C/C-HS and the corresponding recorded maximum temperatures during ablation test using oxyacetylene torch.

Sample	Hemisphere top temperature (°C)	Cylinder Bottom temperature (°C)	Linear ablation rate ($mm \cdot s^{-1}$)	Mass ablation rate ($g \cdot s^{-1}$)
C/C-L	1973	568	0.0196	0.0032
C/C-H	2240	826	0.0282	0.0049
C/C-HS-L	2193	465	0.0147	0.0021
C/C-HS-H	2330	565	0.0229	0.0036

Figure 6-13 shows the macroscopic surface morphologies of the C/C and the C/C-HS after ablation test. With respect to the morphologies before ablation (Figure 6-12), significant evolutions have taken place after ablation: the surfaces present different morphologies and colors according to their distances to the top of the sample. For the C/C, due to the high thermal load and the presence of oxidizing species, it is seen with the increase of heat flux, the surface becomes much rougher. The average surface roughnesses of the top regions of C/C-L and C/C-H are 22.4 and 39.3 μm, respectively. Contrary to the C/C, white ablation products cover the surface of C/C-HS (C/C-HS-L). With the increase of heat flux, the covered area increases (C/C-HS-H). The higher heat flux of oxyacetylene torch leads to the increase of surface temperature and the enhancement of denudation, which then accelerates the corrosion consumption of C/C and C/C-HS. As a result, the linear and mass ablation rates of C/C and C/C-HS increase (Table 6-1). However, compared with the C/C, the C/C-HS exhibits better ablation resistant properties. In addition, with respect to the macroscopic appearance of C/C-HfB_2 composites (Figure 6-5 in section 6.1), due to the addition of SiC, the ablation products on the surface of C/C-HS show better stability. According to the observation of the surface morphologies after ablation (Figure 6-13), there exists a temperature gradient on the ablated surface. Based on the tested TC (Figure 6-11), the temperature distribution along the ablated surface was simulated by COMSOL software. The measured TC at 1600°C was used for the calculation which may differ a little to the practical situation.

Figure 6-14 (a) shows the simulated surface temperature distribution along the ablated surface of C/C-L, from which it can be clearly observed that the temperature decreases gradually from the top to the bottom. For the convenience of discussion, according to the calculated temperature distribution, three representative regions marked as A_1 (top), B_1 (middle) and C_1 (bottom) are selected on the nose ablated surface. Microstructure observations of A_1, B_1 and C_1 regions are shown in Figure 6-14 (b-f). During ablation, A_1 faced the flame directly, so it suffers the highest temperature and the most severe combustion corrosion. Ablation starts at the fiber/matrix interfaces. The circular carbon fibers turn into cone-shape and fiber/matrix interfaces are separated, resulting in the formation of gaps (Figure 6-14 (b)). The formed fiber/matrix gaps would provide the accesses for the flame and then enhance the corrosion of carbon matrix. From A_1 to B_1, the corrosion of C/C gradually decreases, as shown in Figure 6-14 (c-d). The carbon matrix becomes coarse mainly because of chemical corrosion (Figure 6-14 (c)). Due to the degradation of fiber/matrix interfaces, the denudation by oxyacetylene flame leads to the spalling of carbon matrix from carbon fibers (Figure 6-14 (d)). Compared with A_1 and B_1, less ablation is observed at C_1 because of its lower surface temperature (Figure 6-14 (e)). However, debonding of the pyrolytic carbon (around the carbon fiber) is observed (Figure 6-14 (f)), which occurs mainly owing to the TC difference of pyrolytic carbon in radial and axial directions. Pyrolytic carbon layers themselves are combined by weaker attractive bonds (Van der Waals type). According to [66], the radial TC of pyrolytic carbon (about 3.5-50 W/(m·K)) is much lower than that in the fiber axial direction (about 25.6–174W/(m·K)). So, temperature gradient is easily formed and then leads to the debonding of pyrolytic carbon layers.

Like the discussions of C/C-L, the surface morphologies of C/C-H are also divided into three regions (marked as A_2, B_2 and C_2) based on the temperature distribution along the ablated surface, as shown in Figure 6-15 (a). Figure 6-15 (b) shows the typical morphology of A_2. Compared with the morphology of A_1, the surface suffers much more serious ablation with the breakage of carbon matrix. The increased ablation temperature and the enhanced denudation effect of oxyacetylene flame even result in the formation of micro-pores due to the severe corrosion of carbon fibers (Figure 6-15 (d)). Figure 6-15 (c) reveals the morphology of B_2. In addition to the spallation of carbon matrix, part of the carbon fibers is oxidized and even blown away, contributing to the formation of grooves (Figure 6-15 (e)). As for C_2 (Figure 6-15 (f)), although cone-shaped carbon fibers and fiber/matrix gaps are also formed, the ablation is much slighter due to its lower surface temperature (Figure 6-15 (a)).

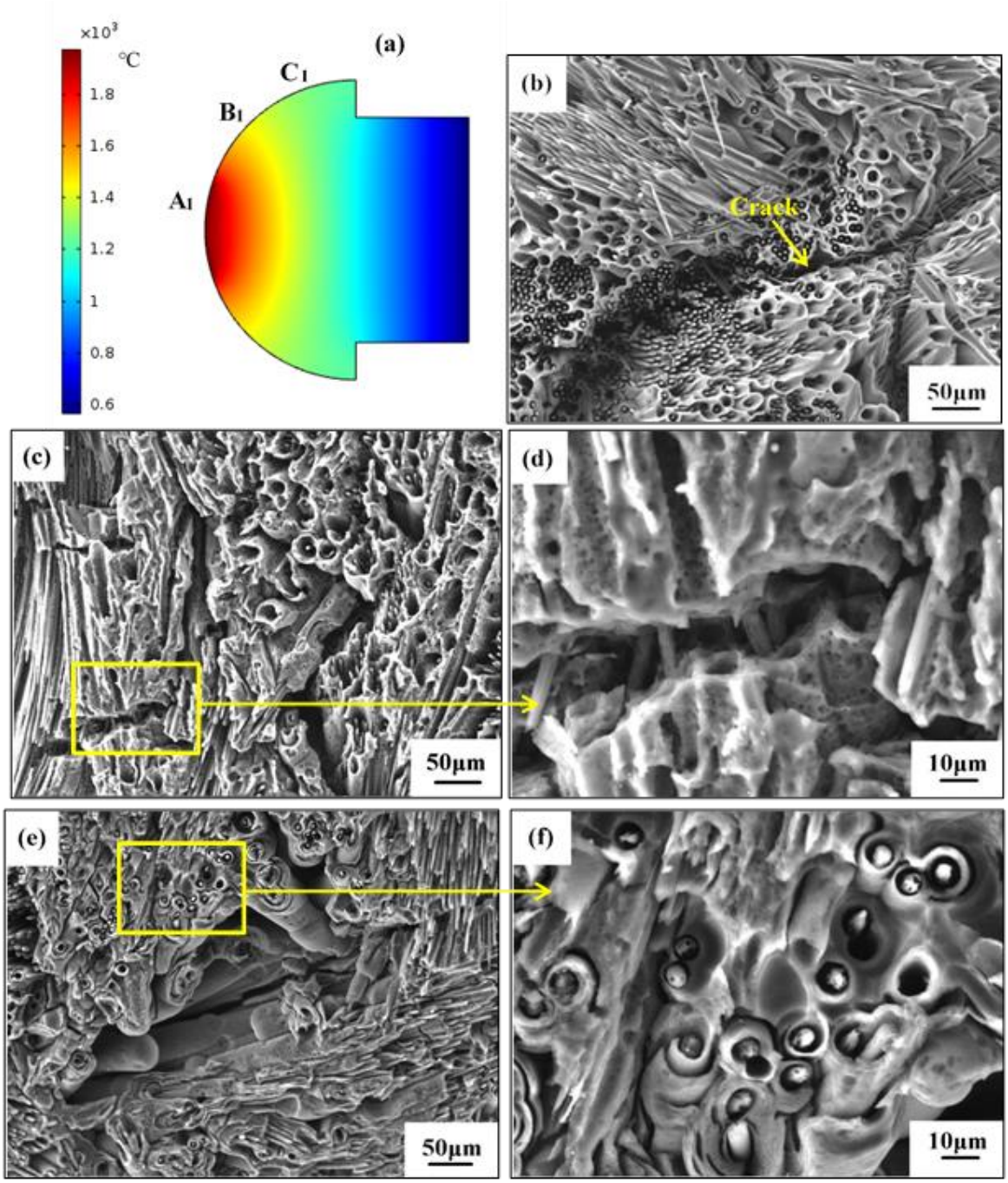

Figure 6-14. Surface temperature distribution and microstructure analysis of C/C-L, (a) Temperature distribution along the ablated surface during ablation, (b) Morphology of A_1, (c) Morphology of B_1, (d) Enlarged view of B_1, (e) Morphology of region C_1, (f) Enlarged view of C_1.

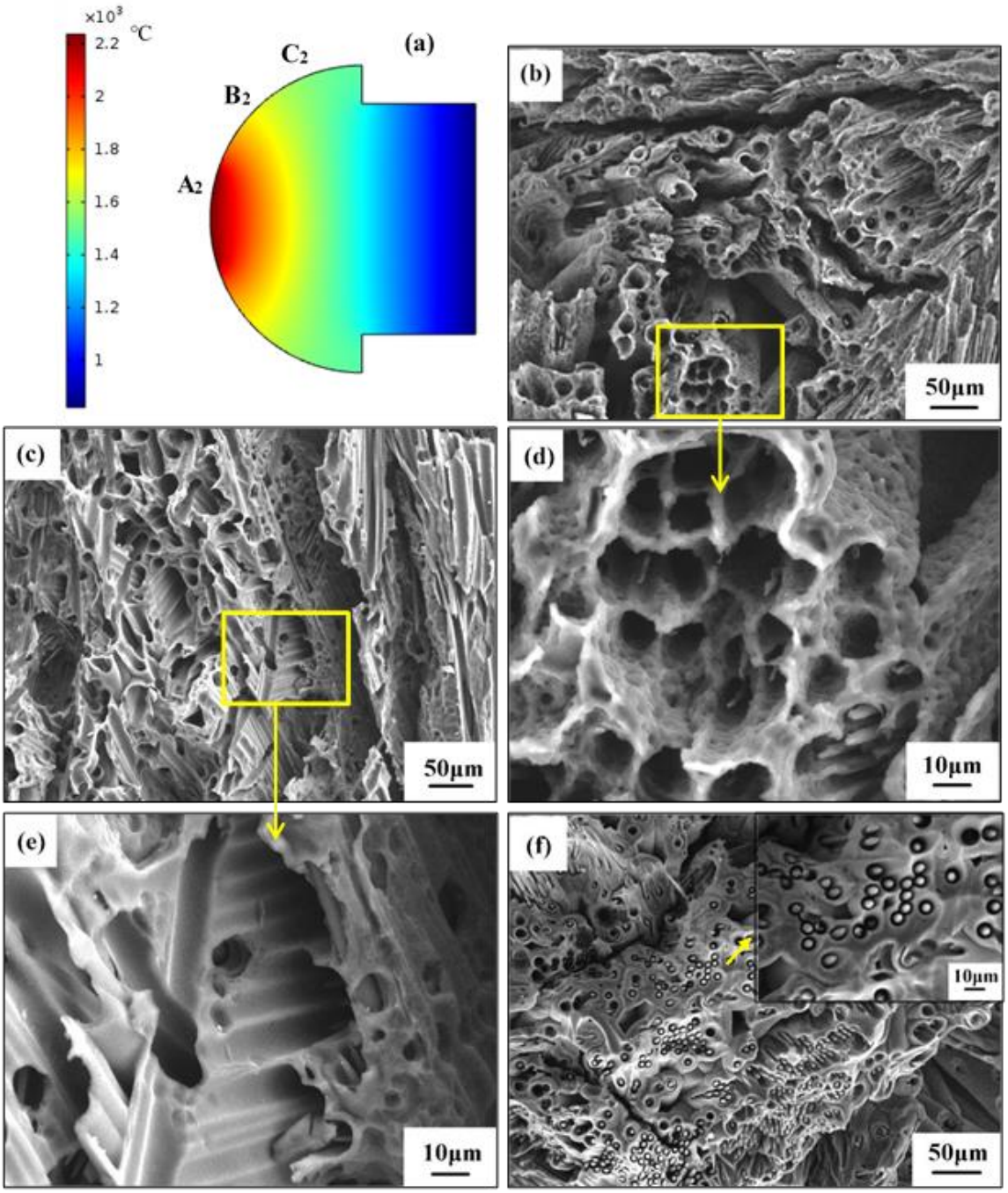

Figure 6-15. Surface temperature distribution and microstructure analysis of C/C-H, (a) Temperature distribution along the ablated surface during ablation, (b) Morphology of A_2, (c) Morphology of B_2, (d) Enlarged view of A_2, (e) Enlarged view of B_2, (f) Morphology of C_2.

Figure 6-16 shows the detected XRD patterns of the ablation products covering the surface of C/C-HS. The phase compositions, HfO_2, SiO_2, B_2O_3 and C, of C/C-HS-L are in accordance with those of C/C-HS-H. HfO_2 and B_2O_3 are the oxidation products of HfB_2, and SiO_2 is formed by the oxidation of SiC.

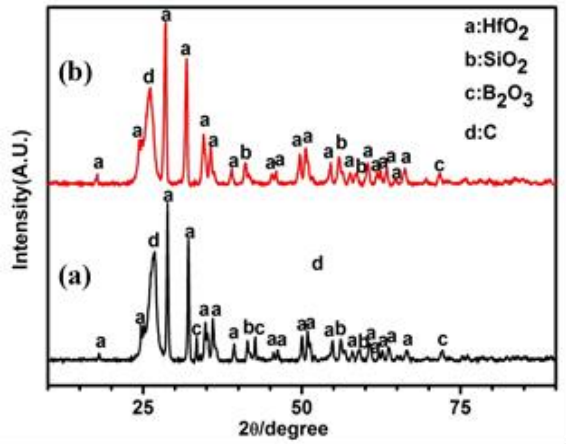

Figure 6-16. XRD patterns of C/C-HS-L (a) and C/C-HS-H (b) after ablation test.

Figure 6-17 (a) depicts the simulated surface temperature distribution along the ablated surface of C/C-HS-L. Like the analysis of C/C, according to the temperature distribution (Figure 6-17 (a)), the ablated surface of C/C-HS-L is also divided into three representative regions (marked as A_3, B_3 and C_3). Figure 6-17 (b) shows the typical morphology of A_3, from which it is observed that the surface is covered by a protective oxidation layer, indicating that the carbon fibers are not facing the oxyacetylene torch directly. From the enlarged view of Figure 6-17 (b), some micro-pores are distributed on the oxidized layer (Figure 6-17 (c)). According to the EDS analysis (Figure 6-17 (f)), the main elements of the oxidation layer are Hf and O. This layer is deduced to be HfO_2 (Figure 6-17). The absence of B_2O_3 and SiO_2 can be due to their quick consumptions. The formed HfO_2 layer could act as a barrier to the heat transfer and denudation of oxyacetylene torch. Figure 6-17 (d) displays the morphology of B_3. It is found that in addition to the white oxidation products, the surface is covered by a glassy layer. Based on its surface temperature (Figure 6-17 (a)), the phase compositions (Figure 6-16) and EDS analysis (see the insert in Figure 6-17 (e)), the glassy protective layer is deduced to be a borosilicate glass [122]. Some micro-cracks and micro-pores are distributed on its surface, which can be attributed to the escape of the gas products generated by the oxidation of SiC and carbon fibers [81]. As for the C_3, compared with B_3, the protective glass layer becomes much more uniform. Because of its low oxygen diffusion coefficient, the formed borosilicate glass layer can efficiently prevent the infiltration of the oxidizing species brought by the oxyacetylene flame.

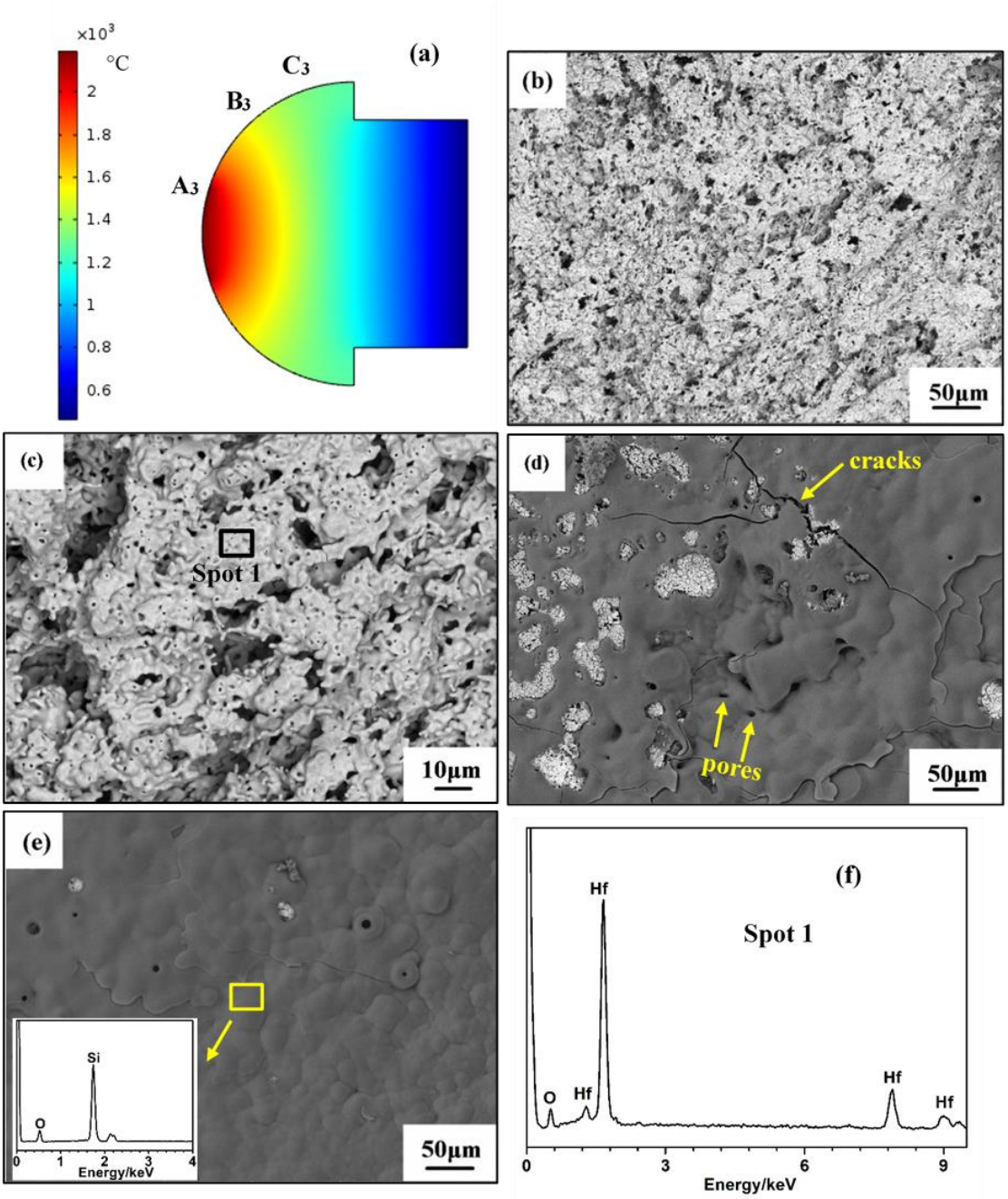

Figure 6-17. Surface temperature distribution and microstructure analysis of C/C-HS-L, (a) Temperature distribution along the ablated surface during ablation, (b) Morphology of A_3, (c) Enlarged view of A_3, (d) Morphology of B_3, (e) Morphology of C_3, (f) EDS of Spot1 in (c).

For C/C-HS-H, the heat flux increase leads to the increase of the surface temperature (shown in Figure 6-18 (a)) and the enhancement of denudation. The morphologies of the three representative regions (marked as A_4, B_4 and C_4) are selected to facilitate the discussion. Figure 6-18 (b) depicts the morphology of A_4. Compared with A_3 (Figure 6-17 (b-c)), the integrity of the HfO_2 layer is degraded, where more holes and grooves are formed. As seen in its enlarged view (Figure 6-18 (c)), the HfO_2 scale is partly broken.

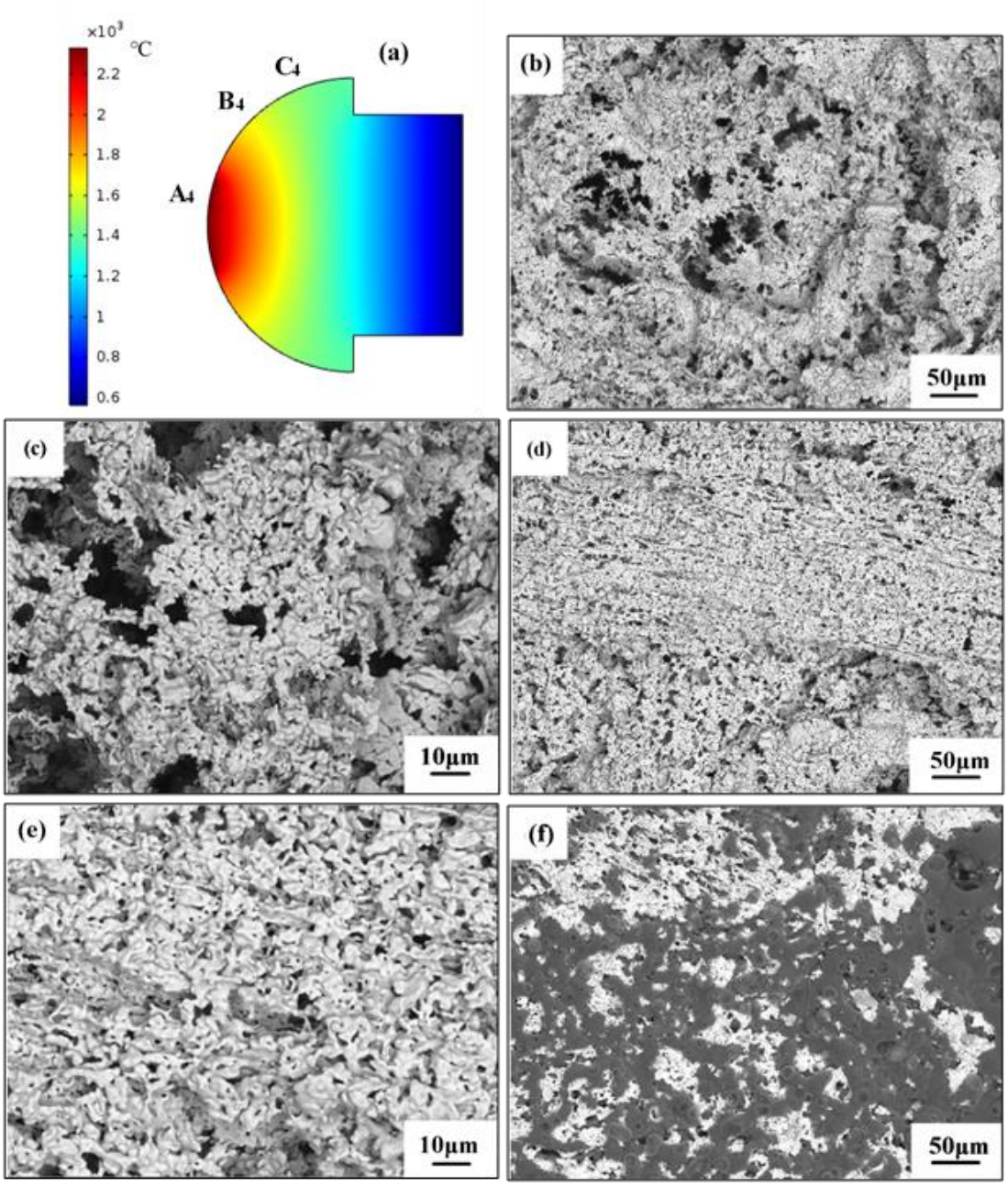

Figure 6-18. Surface temperature distribution and microstructure analysis of C/C-HS-H, (a) Temperature distribution along the ablated surface during ablation, (b) Morphology of region A_4, (c) Enlarged view of A_4, (d) Morphology of B_4, (e) Enlarged view of B_4, (f) Morphology of C_4.

As for the morphology of B_4 (Figure 6-18 (d)), compared with B_3 (Figure 6-17 (d)), due to its higher temperature and stronger denudation, SiO_2 and B_2O_3 are consumed much more rapidly, resulting in the absence of protective glassy layer. Form the enlarged view of Figure 6-18 (d), it is inferred that the increased denudation also promotes the formation of holes and grooves on the HfO_2 layer (Figure 6-18 (e)). Figure 6-18 (f) depicts the morphology of C_4. HfO_2-glass is observed, which is like the morphology of B_3 (Figure 6-17 (d)). But some

bubbles caused by the volatilization of the gas ablation products are distributed on the glassy layer, which is expected to degrade its protective performance and then enhances the denudation by oxyacetylene flame.

6.2.3 Ablation mechanism

The environment of oxyacetylene flame is regarded as an oxygen-rich condition. Depending on the surface temperature (Figure 6-14, 6-15, 6-17 and 6-18), the main possible reactions of C/C and C/C-HS during ablation are presented as follow [122, 123]:

$$HfB_2(s) + 2.5\ O_2(g) \longrightarrow HfO_2(s) + B_2O_3(l) \quad (6\text{-}4)$$

$$HfB_2(s) + 2.5\ O_2(g) \longrightarrow HfO_2(s) + B_2O_3(g) \quad (6\text{-}5)$$

$$SiC\ (s) + 1.5\ O_2(g) \longrightarrow SiO_2(l) + CO\ (g) \quad (6\text{-}6)$$

$$SiC\ (s) + 2\ O_2(g) \longrightarrow SiO_2\ (l) + CO_2\ (g) \quad (6\text{-}7)$$

$$SiC\ (s) + O_2(g) \longrightarrow SiO\ (g) + CO\ (g) \quad (6\text{-}8)$$

$$C\ (s) + 0.5\ O_2(g) \longrightarrow CO\ (g) \quad (6\text{-}9)$$

$$C\ (s) + O_2(g) \rightarrow CO_2(g) \quad (6\text{-}10)$$

The corresponding standard Gibbs free energy changes of the reactions ((6-4)-(6-10)) were calculated by HSC software [84, 114, 115], as is shown in Figure 6-19. According to the surface morphology observation and XRD analysis (Figure 6-16), it is anticipated that the above chemical reactions (6-4 to 6-10) could occur due to their negative standard Gibbs energy values. Concerning reaction (6-4), reaction (6-5) is more thermodynamically probable at temperatures above T_1 (2100 °C) shown in Figure 6-19, which corresponds to the boiling point of B_2O_3 [124]. For C/C, during ablation, the fiber/matrix interfaces are ablated in priority and then extend, resulting in the morphology changes of carbon fibers and carbon matrix (Figure 6-14, 6-15). So appreciable amounts of the heat flux are converted to an outward mass flux through the oxidation consumption (reaction (6-9) and (6-10)), leading to the mass loss (Table 6-1). The generated gases (CO (g) and CO_2 (g)) would then diffuse into the combustion gases, which is beneficial for reducing the oxygen concentration.

As for C/C-HS, based on the microstructure analysis after ablation (Figure 6-17 and 6-18), the ablation products of HfB_2 and SiC (reaction (6-4) and (6-8)) could form protective layers covering the surface, which efficiently withstand the heat transfer and denudation by

oxyacetylene flame. According to the microstructure evolutions shown in Figure 6-17, the ablation process of C/C-HS can be mainly divided into three steps. Firstly, when the sample is subjected to the oxyacetylene fame, the impacted area is heated instantaneously. SiC and HfB_2 will react with the hot oxidative gases, resulting in the formation of the borosilicate glass and HfO_2 [122]. The formed borosilicate glass has low diffusivity for oxygen. Because of the high wetting angle between the borosilicate glass and HfO_2 [122], the borosilicate glass, then viscous, flows to the surface of HfO_2 by capillary force [125], leading to the formation of a glassy protective layer (Figure 6-17 (e)). The glass then acts as a barrier against the inward diffusion of oxygen and the combustion gas corrosion. With the increase of the ablation temperature, the vapor pressures of SiO_2 and B_2O_3 increase (as shown in Figure 6-20). So, the second step begins when the temperature rises to the vaporization threshold of the glass layer. Due to the release of B_2O_3 and SiO_2 from the outermost borosilicate layer and the escape of the gas products (reactions (6-9) and (6-10)), some pores are formed on the surface, providing the diffusion accesses of the oxyacetylene flame. As a result, the formed glass layer is easily removed or even blown away from the surface, resulting in the appearance of some underlying HfO_2 areas (Figure 6-17 (d)). With the ablation time further prolonging, the higher temperature accelerates the removal of the glassy ablation products and then a HfO_2 scale appears on the surface. As shown in Figure 6-17 (b-c), the formed HfO_2 scale is not blown away, indicating that it could withstand the shearing force of the oxyacetylene torch and resist its denudation effect.

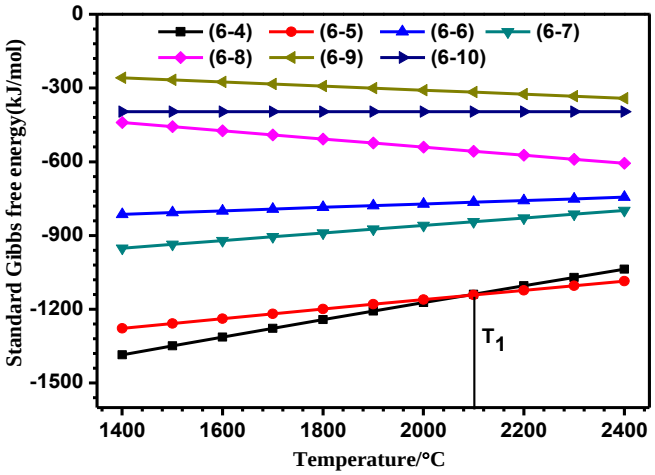

Figure 6-19. Changes of standard Gibbs free energies of reactions (6-4) to (6-10) at different temperatures calculated by HSC software.

For the ablation of C/C-HS-H, the increased heat flux promotes the increase of surface temperature and enhances the denudation by the combustion gas. As mentioned in the ablation process of C/C-HS-L, borosilicate and HfO_2 are formed on the surface. As for C/C-HS-H, on the contrary, its higher surface temperature and stronger denudation significantly promotes the removal or evaporation of the glassy ablation products due to their high vapor pressures (Figure 6-18 (f) and 6-20), leaving HfO_2 scale (Figure 6-18 (d-e)). Contrary to the HfO_2 scale at the nose tip of C/C-HS-L (Figure 6-17 (b-c)), the formed HfO_2 scale (Figure 6-18 (b-c)) is partly broken, indicating that the shear forces of oxyacetylene flame exceed the strength of the HfO_2 framework.

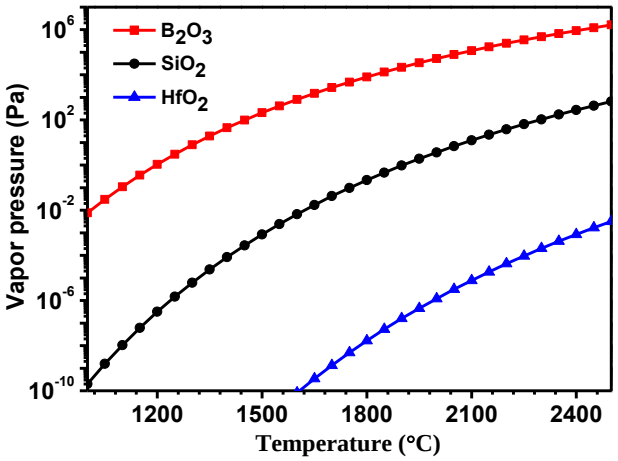

Figure 6-20. Vapor pressure vs temperature for SiO_2, B_2O_3 and HfO_2 calculated at ambient pressure (vapor pressure in logarithmic scale).

6.3 Conclusions

1. C/C-HfB_2 composites were prepared by precursor infiltration and pyrolysis and chemical vapor infiltration. Thermogravimetric analysis showed that the addition of HfB_2 can improve the oxidation resistance of C/C composites significantly in air condition. Ablation behavior was investigated using an oxyacetylene torch with two different heat fluxes. In the heat flux of 2.38 MW/m^2, the C/C-HfB_2 composites exhibited good ablation properties, and a HfO_2 layer was formed on the surface which played an efficient role in withstanding the heat transfer and denudation of oxyacetylene torch. As the heat flux increased to of 4.18 MW/m^2, ablation performance of the C/C-HfB_2 composites was degraded. Thermal energy concentration and denudation enhancement of the oxyacetylene torch resulted in the cracking

and spallation of the HfO_2 protective layer and then enhanced the erosion of C/C-HfB_2 composites.

2. To simulate the thermal-structural components, precursor infiltration and pyrolysis was proposed to facilitate the preparation of nose-shaped C/C-HfB_2-SiC composites. Ablation behavior was performed in two different heat fluxes (2.38 and 4.18 MW/m^2) using oxyacetylene torch. Different ablation morphologies were found because of the temperature differences caused by the nose-shaped features.

(1) During ablation in 2.38 MW/m^2, compared with the bare C/C, the prepared C/C-HfB_2-SiC composites showed better ablation performance and structural stability. Protective ablation products including borosilicate glass, HfO_2-glass and HfO_2 scale were distributed along the nose-shaped ablated surface, which were beneficial for enduring the heating conditions. Although the nose tip suffered the most serious corrosion, the HfO_2 scale could withstand the oxyacetylene torch scouring.

(2) As the heat flux increased to 4.18 MW/m^2, much more serious ablation took place. From the nose bottom to tip, the increased surface temperature and the enhanced denudation led to the elimination of the borosilicate glass, the removal of glass from the HfO_2-glass. The prepared C/C-HfB_2-SiC could still provide a stable resistance to the severe ablative environment due to the good stability of the formed ablation products. However, at the nose tip, the stronger oxyacetylene torch scouring led to the partly ruptured HfO_2 scale.

Chapter 7: Conclusion and Perspectives

In this thesis, we focused on the improvement of oxidation and ablation performances of C/C composites. Two methods, coating technology and matrix modification were implemented.

(1) Coating technology

To relieve the thermal expansion mismatch and improve the adhesive strength between coating and C/C substrate, blasting treatment was performed so as to construct an inlaid coating/substrate interface. We studied the inlaid coating/substrate interface on the adhesive strength of SiC coating. The results showed that the formed inlaid coating/substrate interface improves the coating/substrate adhesive strength efficiently. Compared with the coated C/C composites without blasting treatment, the maximum coating/substrate adhesive strength was increased by 43%.

We studied the inlaid coating/substrate interface on the cyclic ablation performance of Si-Mo-Cr coating. Due to the adhesive strength improvement and the thermal mismatch alleviation between coating and substrate, after 25 thermal cycles from 1600°C to room temperature, the coating was uniform with the formation of a glassy $SiO_2 + Cr_2O_3$ protective layer covering the surface. However, due to the inherent brittleness of the Si-Mo-Cr coating, micro-cracks also existed. To address this problem, inlaid coating/substrate design and introduction of SiC nanowires were combined. The results showed that SiC nanowires introduction further improves the coating/substrate adhesive strength and decrease the coating thermal stress during high-low temperature cycles. After thirty 1600^{o}C-room temperature thermal cycles under parallel oxyacetylene torch, the mass loss per unit area of the coated C/C composites was about 15 $mg \cdot cm^{-2}$. In contrast, the mass loss per unit area of the coated C/C composites without SiC nanowires was up to 28 $mg \cdot cm^{-2}$ and penetrating crack was formed.

SiC coating is easy to fail at temperature higher 1700^{o}C, to address the problem, we studied the effect of inlaid coating/substrate interface design and HfC additive on the cyclic ablation performance of SiC coating from 1750^{o}C to room temperature. Because of the thermal stress relief, coating/substrate adhesive strength improvement and the good thermal stability of HfO_2 and SiO_2 mixed layer, the HfC-SiC coating showed good ablation performance. However, due to its poor sintering property, the cyclic ablation performance of the HfC-SiC coating was limited after longer ablation time. As a result, we then studied the effect of construction of inlaid coating/substrate interface and ZrB_2 additive (instead of HfC)

on the performance of SiC coating. Compared with the HfC-SiC coating, the ZrB_2-SiC coating possessed better sintering performance. Cyclic ablation test from 1750^oC to room temperature showed that the prepared ZrB_2-SiC coating possessed better ablation performance.

In addition, to better evaluate the service reliability of multi-layer ceramic coating, a non-destructive depth sensitive characterization method, that is XRR combined with PIXE-Kossel were developed. We studied the feasibility of this method by using the Pt/Fe/Pt and Ta/Cr/Pt X-ray planar film waveguides. To obtain a satisfying agreement between experiment and simulation for both XRR and PIXE-Kossel curves, interlayers consisting of Fe and Pt form at the interfaces of the Pt/Fe/Pt waveguide, while in the Ta/Cr/Pt system, some intermixing takes place between the Ta and Cr layers to form a compound, which was subsequently partly oxidized. The results confirmed the feasibility of this method to be used in non-destructive characterization of multi-layer stacks. Based on the above results, we could also build a waveguide mode in HfC/SiC/HfC multilayer for C/C composites. By considering the Kossel curve simulation results, it will be helpful to analyze the oxidation process of the HfC/SiC/HfC multilayer in future work.

(2) Matrix modification

Matrix modification is the other method to improve the oxidation and ablation performances of C/C. We studied the effect of HfB_2 addition on the oxidation and ablation performances of C/C. C/C-HfB_2 composites were prepared by precursor infiltration and pyrolysis and chemical vapor infiltration. Thermogravimetric analysis showed that the addition of HfB_2 can improve the oxidation resistance of C/C composites significantly in air. Due to the formed HfO_2 layer on the surface, C/C-HfB_2 composites also showed good ablation performance in the heat flux of 2.38 MW/m^2 using oxyacetylene torch. However, as the ablated heat flux increased to 4.18 MW/m^2, thermal energy concentration and denudation enhancement of the oxyacetylene torch resulted in the cracking and spallation of the HfO_2 protective layer.

Due to limited protective ability of HfB_2, HfB_2-SiC were introduced into C/C. To simulate the thermal-structural components, nose-shaped C/C-HfB_2-SiC composites were prepared. After ablation, different morphologies were found because of the temperature differences caused by the nose-shaped features. After ablation in 2.38 MW/m^2 using oxyacetylene torch, the C/C-HfB_2-SiC composites showed good ablation performance and structural stability. Protective ablation products including borosilicate glass, HfO_2-glass and HfO_2 scale were distributed along the nose-shaped ablated surface, which were beneficial for enduring the heating conditions. As the heat flux increased to 4.18 MW/m^2, much more

serious ablation took place. From the nose bottom to tip, the increased surface temperature and the enhanced denudation led to the elimination of the borosilicate glass and the removal of glass from the HfO_2-glass. Due to the good stability of the formed ablation products, the prepared C/C-HfB_2-SiC composites could still withstand the severe ablative environment However, at the nose tip, the stronger oxyacetylene torch scouring led to the partly broken of the HfO_2 scale.

(3) Perspectives

In next work, the coating technology and matrix modification are expected to be combined. To provide a better protection of C/C composites at high temperature, protective coatings with an inlaid coating/substrate interface should be prepared on the surface of C/C-HfB_2-SiC composites.

For PIXE-Kossel method, the development of the codes which can perform the XRR fitting and Kossel curve simulation at the same time will facilitate our analysis. Working in the soft x-ray range by removing the Be filter in front of the CCD camera. This would make us have access to the characteristic emissions of oxygen, carbon, and probably also other interesting lines. Working at high spectral resolution with a crystal spectrometer will bring the chemical sensitivity in addition to the elemental one, this would be done at the expense of the acquisition time as scanning the angles would be required.

Annex

(1) Parameters of the Kossel curve simulation

The simulation is performed with the FLUORT code [107], which calculates the electric field generated within the stack by the emitted radiation according to the reciprocity theorem. The parameters of the Pt/Fe/Pt and Ta/Cr/Pt X-ray planar film waveguides (thickness, roughness) introduced in the simulation are those deduced from XRR analyses. For the giving the wavelength (nm) of the fluorescence emission, the optical indices (real part δ and imaginary part β) obtained from CXRO [61] are introduced. The parameters are given starting from the substrate and then from the layer closest to the substrate to the one closest to the surface. The emitted value i is set as 0-1 for a specific layer. If all the atoms of the layer are emitting, the i value is set as 1. If the layer is not emitting, the i value is set as 0. If the layer is a mixing layer formed by a compound, it is considered to be partly emitted and the corresponding i value is set between 0 and 1, which represents the weighting value that used to calculate the optical indices. In our simulation, the actual i value for a compound is adjusted based on the comparison of the simulation/experimental Kossel curve. Here we list the optical indices and emitted values used in our research.

Table 8-1. Thickness, optical indices and emitted values of the PFP-1 stack used for the Fe Kα (wavelength 0.19363 nm) Kossel curve simulation (listed from the top to the substrate).

	Thickness/Roughness (nm)	δ	β	Emitted value
Pt	4.62/0.60	8.2836872E-05	1.15023659E-05	0
Fe	6.65/0.80	3.41946798E-05	8.26432256E-07	1
Pt	11.06/0.77	8.2836872E-05	1.15023659E-05	0
Si substrate	bulk/0.42	1.20366931E-05	4.21871192E-07	--

Table 8-2. Thickness, optical indices and emitted values of the PFP-1 stack used for the Pt Lα (wavelength 0.13131 nm) Kossel curve simulation (listed from the top layer to the substrate).

	Thickness/Roughness (nm)	δ	β	Emitted value
Pt	4.62/0.60	3.71569477E-05	2.88326692E-06	1
Fe	6.65/0.80	1.69425839E-05	1.63661127E-06	0
Pt	11.06/0.77	3.71569477E-05	2.88326692E-06	1
Si substrate	bulk/0.42	5.48981643E-06	9.24908576E-08	--

Table 8-3. Thickness, optical indices and emitted values of the PFP-1 stack used for the Fe Kα (wavelength 0.19363 nm) Kossel curve simulation accounting for the presence of $Pt_{69}Fe_{31}$ interlayers at both interfaces (listed from the top layer to the substrate).

	Thickness/Roughness (nm)	δ	β	Emitted value
Pt	3.83/0.57	8.2836872E-05	1.15023659E-05	0
$Pt_{69}Fe_{31}$	1.62/0.90	6.26665278E-05	7.79348466E-06	0.5
Fe	5.19/1.20	3.41946798E-05	8.26432256E-07	1
$Pt_{69}Fe_{31}$	1.41/0.79	6.26665278E-05	7.79348466E-06	0.5
Pt	10.25/0.39	8.2836872E-05	1.15023659E-05	0
Si substrate	bulk/0.50	1.20366931E-05	4.21871192E-07	--

Table 8-4. Thickness, optical indices and emitted values of the PFP-1 stack used for the Pt Lα (wavelength 0.13131 nm) Kossel curve simulation accounting for the presence of $Pt_{69}Fe_{31}$ interlayers at both interfaces (listed from the top layer to the substrate).

	Thickness/Roughness (nm)	δ	β	Emitted value
Pt	3.83/0.57	3.71569477E-05	2.88326692E-06	1
$Pt_{69}Fe_{31}$	1.62/0.90	2.84809375E-05	2.28457861E-06	0.5
Fe	5.19/1.20	1.69425839E-05	1.63661127E-06	0
$Pt_{69}Fe_{31}$	1.41/0.79	2.84809375E-05	2.28457861E-06	0.5
Pt	10.25/0.39	3.71569477E-05	2.88326692E-06	1
Si substrate	bulk/0.50	5.48981643E-06	9.24908576E-08	--

Table 8-5. Thickness, optical indices and emitted values of the PFP-2 stack used for the Fe Kα (wavelength 0.19363 nm) Kossel curve simulation accounting for the presence of $Pt_{69}Fe_{31}$ interlayers at both interfaces (listed from the top layer to the substrate).

	Thickness/Roughness (nm)	δ	β	Emitted value
Pt	4.20/1.29	8.2836872E-05	1.15023659E-05	0
$Pt_{69}Fe_{31}$	2.06/0.92	6.26665278E-05	7.79348466E-06	0.5
Fe	7.89/1.72	2.86620361E-05	1.63661127E-06	1
$Pt_{69}Fe_{31}$	0.57/0.42	6.26665278E-05	7.79348466E-06	0.5
Pt	10.79/0.83	8.2836872E-05	1.15023659E-05	0
Si substrate	0.67	1.20366931E-05	4.21871192E-07	--

Table 8-6. Thickness, optical indices and emitted values of the PFP-2 stack used for the Pt Lα (wavelength 0.13131 nm) Kossel curve simulation accounting for the presence of $Pt_{69}Fe_{31}$ interlayers at both interfaces (listed from the top layer to the substrate).

	Thickness/Roughness (nm)	δ	β	Emitted value
Pt	4.20/1.29	3.71569477E-05	2.88326692E-06	1
$Pt_{69}Fe_{31}$	2.06/0.92	2.84809375E-05	2.28457861E-06	0.5
Fe	7.89/1.72	1.42013005E-05	1.3718103E-06	0
$Pt_{69}Fe_{31}$	0.57/0.42	2.84809375E-05	2.28457861E-06	0.5
Pt	10.79/0.83	3.71569477E-05	2.88326692E-06	1
Si substrate	0.67	5.48981643E-06	9.24908576E-08	--

Table 8-7. Thickness, optical indices and emitted values of the TCP stack used for the Cr Kα (wavelength 0.22901 nm) Kossel curve simulation (listed from the top layer to the substrate).

	Thickness/Roughness (nm)	δ	β	Emitted value
Ta_2O_5	7.87/1.09	4.71093408E-05	5.42594216E-06	0
Cr_2O_3	6.55/1.30	3.30634066E-05	6.50797574E-07	1
Cr	4.54/0.80	4.2895932E-05	1.08442578E-06	1
Pt	13.79/0.54	0.000115832874	2.08071779E-05	0
Si substrate	bulk/0.67	1.68926108E-05	8.0703353E-07	--

Table 8-8. Thickness, optical indices and emitted values of the TCP stack used for the Pt Lα (wavelength 0.13131 nm) Kossel curve simulation (listed from the top layer to the substrate).

	Thickness/Roughness (nm)	δ	β	Emitted value
Ta_2O_5	7.87/1.09	1.46212806E-05	7.47031322E-07	0
Cr_2O_3	6.55/1.30	1.15756538E-05	6.0811584E-07	0
Cr	4.54/0.80	1.55821581E-05	1.20304855E-06	0
Pt	13.79/0.54	3.71569477E-05	2.88326692E-06	1
Si substrate	bulk/0.67	5.48981643E-06	9.24908576E-08	--

Table 8-9. Thickness, optical indices and emitted values of the TCP stack used for the Ta Lα (wavelength 0.1522 nm) Kossel curve simulation (listed from the top layer to the substrate).

	Thickness/Roughness (nm)	δ	β	Emitted value
Ta_2O_5	7.87/1.09	2.03214768E-05	1.26726388E-06	1
Cr_2O_3	6.55/1.30	1.54236968E-05	1.04751325E-06	0
Cr	4.54/0.80	2.06609984E-05	2.0697355E-06	0
Pt	13.79/0.54	5.06351062E-05	4.88611749E-06	0
Si substrate	bulk/0.67	7.39785764E-06	1.65047382E-07	--

Table 8-10. Thickness, optical indices and emitted values of the TCP stack used for the Cr Kα (wavelength 0.22901 nm) Kossel curve simulation accounting for the compound formation and subsequent oxidation (listed from the top layer to the substrate).

	Thickness/Roughness (nm)	δ	β	Emitted value
$CrTaO_4$	10.75/1.10	3.5393281E-05	3.14593399E-06	0.8
$TaCr_2$	3.96/1.32	4.5005796E-05	4.46785589E-06	0.9
Cr	4.02/0.53	4.2895932E-05	1.08442578E-06	1
Pt	13.79/0.54	0.000115832874	2.08071779E-05	0
Si substrate	bulk/0.69	1.68926108E-05	8.0703353E-07	--

Table 8-11. Thickness, optical indices and emitted values of the TCP stack used for the Pt Lα (wavelength 0.13131 nm) Kossel curve simulation accounting for the compound formation and subsequent oxidation (listed from the top layer to the substrate).

	Thickness/Roughness (nm)	δ	β	Emitted value
$CrTaO_4$	10.75/1.10	1.13721972E-05	5.85948612E-07	0
$TaCr_2$	3.96/1.32	1.47605806E-05	1.04570006E-06	0
Cr	4.02/0.53	1.55821581E-05	1.20304855E-06	0
Pt	13.79/0.54	3.71569477E-05	2.88326692E-06	1
Si substrate	bulk/0.69	5.48981643E-06	9.24908576E-08	--

Table 8-12. Thickness, optical indices and emitted values of the TCP stack used for Ta Lα (wavelength 0.1522 nm) Kossel curve simulation accounting for the compound formation and subsequent oxidation (listed from the top layer to the substrate).

	Thickness/Roughness (nm)	δ	β	Emitted value
$CrTaO_4$	10.75/1.10	1.56097813E-05	9.98691007E-07	0.1
$TaCr_2$	3.96/1.32	2.02273768E-05	1.78457242E-06	0.2
Cr	4.02/0.53	2.06609984E-05	2.0697355E-06	0
Pt	13.79/0.54	5.06351062E-05	4.88611749E-06	0
Si substrate	bulk/0.69	7.39785764E-06	1.65047382E-07	--

Table 8-13. Thickness, optical indices and emitted values of the HfC/SiC/HfC stack used for the Hf Lα (wavelength 0.15696 nm) Kossel curve simulation (listed from the top layer to the substrate).

	Thickness (nm)	δ	β	Emitted value
HfC	4	3.35163568E-05	2.5344043E-06	1
SiC	8	1.08277827E-05	1.85544792E-07	0
HfC	10	3.35163568E-05	2.5344043E-06	1
C substrate	bulk	7.33721299E-06	1.25383295E-08	--

Table 8-14. Thickness, optical indices and emitted values of the HfC/SiC/HfC stack used for the Si Kα (wavelength 0.79784 nm) Kossel curve simulation (listed from the top layer to the substrate).

	Thickness (nm)	δ	β	Emitted value
HfC	4	0.000460319832	0.000117905416	0
SiC	8	0.000250403566	1.07448632E-05	1
HfC	10	0.000460319832	0.000117905416	0
C substrate	bulk	0.000196129447	8.82246422E-06	--

Table 8-15. Thickness, optical indices and emitted values of the HfO_2/SiC/HfC stack used for the Hf Lα (wavelength 0.15696 nm) Kossel curve simulation (listed from the top layer to the substrate).

	Thickness (nm)	δ	β	Emitted value
HfO_2	5.4	2.51479032E-05	1.68670647E-06	1
SiC	8	1.08277827E-05	1.85544792E-07	0
HfC	10	3.35163568E-05	2.5344043E-06	1
C substrate	bulk	7.33721299E-06	1.25383295E-08	--

Table 8-16. Thickness, optical indices and emitted values of the HfO_2/SiC/HfC stack used for the Si Kα (wavelength 0.79784 nm) Kossel curve simulation (listed from the top layer to the substrate).

	Thickness (nm)	δ	β	Emitted value
HfO_2	5.4	0.000386070809	8.85927802E-05	0
SiC	8	0.000250403566	1.07448632E-05	1
HfC	10	0.000460319832	0.000117905416	0
C substrate	bulk	0.000196129447	8.82246422E-06	--

(1) Python code for the PIXE spectrum processing

We make an adjustment of the generated signals of Koseel curves by using a specially written Python program, as follow:

```
import os
import time

print("Neccessite Python 3 ou +")
correction=float(input("Entrez le facteur de correction en pourcentage % (min : 1, max 3): "))
nom_fichier=input("Entrez le nom du fichier, si aucun, Fichier.dat sera utilisé : ")

if nom_fichier == "":

    nom_fichier = "Fichier.dat"
file = open(nom_fichier,"r")
data=[]
data = [ line.split() for line in file]

i=0
for ligne_calcul in data:
    try:
        if (i>0):
            data[i][1]=float(data[i][1])-float(data[i][0])*float(correction/100)
    except:
        pass
    i+=1

file_rotation = open("Fichier_Rotation.dat","w")
x=0
for i in data:
    for j in range(len(i)):
        file_rotation.write(str(i[j])+" ")
    file_rotation.write("\n")
    x+=1
file_rotation.close()

kossel_rotation=[0]*256
pe=0
for z in data:
##    print(z)
##    time.sleep(1)
    if (pe>0) and z!=[]:
        kossel_rotation[int(z[1])]=kossel_rotation[int(z[1])]+int(z[2])
    pe+=1
print(kossel_rotation)
file_rotation_kossel = open("Fichier_Kossel_Rotation.dat","w")
x=0
for i in kossel_rotation:
    file_rotation_kossel.write(str(x)+" "+str(i))
    file_rotation_kossel.write("\n")
    x+=1
file_rotation_kossel.close()


afficher = open("workfile.gnuplot","w")
afficher.write("set term wxt 0\n")
afficher.write("plot \"Fichier.dat\" u 1:2:3 w image t \"Affichage caméra (fermeture dans 10s)\"\n")
afficher.write("set term wxt 1\n")
afficher.write("plot \"Fichier_Rotation.dat\" u 1:2:3 w image t \"Affichage caméra (fermeture dans 0s)\"\n")
afficher.write("set term wxt 2\n")
afficher.write("plot \"Fichier_Kossel_Rotation.dat\" u 1:2 w l lw 3 t \"Kossel avec rotation(fermeture dans 0s)\"\n")
afficher.write("pause 15")
```

Bibliography

[1] Zazula J M, On graphite transformations at high temperature and pressure induced by absorption of the LHC beam, in, CERN-LHC-Project-Note-78, 1997,

[2] Savage G. Applications of Carbon-carbon composites. in: Carbon-Carbon Composites, Springer, pp. 323-359, 1993

[3] Buckley J D and Edie D D. Carbon-carbon materials and composites. William Andrew, 1993

[4] Windhorst T and Blount G. Carbon-carbon composites: a summary of recent developments and applications. *Materials & Design,* 18 (1), 11-15, 1997.

[5] Fitzer E and Manocha L M. Carbon reinforcements and carbon/carbon composites. Springer Science & Business Media, 2012

[6] Smeacetto F, Ferraris M and Salvo M. Multilayer coating with self-sealing properties for carbon–carbon composites. *Carbon,* 41 (11), 2105-2111, 2003.

[7] Sun W, Xiong X, Huang B-y, Li G-d, Zhang H-b, Chen Z-k and Zheng X-L. ZrC ablation protective coating for carbon/carbon composites. *Carbon,* 47 (14), 3368-3371, 2009.

[8] Padture N P. Advanced structural ceramics in aerospace propulsion. *Nature materials,* 15 (8), 804, 2016.

[9] Peng W, Shanbao Z, Xinghong Z, Kaixuan G, Yongxia L, Jiadong A and Wenbo H. Thermal cycling and oxidation resistance of B modified ZrB_2–SiC coatings on SiC coated graphite. *Surface and Coatings Technology,* 280, 330-337, 2015.

[10] ZhongLiu W, Peng X, Zhuan L, Wen H, Heng L, XiaoYu Y, Yang L and WenBo C. Microstructure and oxidation behavior of sol–gel mullite coating on SiC-coated carbon/carbon composites. *Journal of the European Ceramic Society,* 35 (14), 3789-3796, 2015.

[11] Friedrich C, Gadow R and Speicher M. Protective multilayer coatings for carbon–carbon composites. *Surface and Coatings Technology,* 151, 405-411, 2002.

[12] Pham D, Dycus J H, LeBeau J M, Manga V R, Muralidharan K and Corral E L. Processing Low‐Oxide ZrB_2 Ceramics with High Strength Using Boron Carbide and Spark Plasma Sintering. *Journal of the American Ceramic Society,* 99 (8), 2585-2592, 2016.

[13] Kütemeyer M, Schomer L, Helmreich T, Rosiwal S and Koch D. Fabrication of ultra high temperature ceramic matrix composites using a reactive melt infiltration process. *Journal of the European Ceramic Society,* 36 (15), 3647-3655, 2016.

[14] Li C, Li K, Ouyang H, Huang J, Li H, Zhang Y, Fei J and Kong X. Effect of ZrO_2

morphology on the ablation resistance of carbon/carbon composites containing ZrC prepared by the carbothermal reduction reaction. *Corrosion Science,* 102, 405-412, 2016.

[15] Jin X, He R, Zhang X and Hu P. Ablation behavior of ZrB_2–SiC sharp leading edges. *Journal of Alloys and Compounds,* 566, 125-130, 2013.

[16] Nisar A, Ariharan S, Venkateswaran T, Sreenivas N and Balani K. Effect of carbon nanotube on processing, microstructural, mechanical and ablation behavior of ZrB_2-20SiC based ultra-high temperature ceramic composites. *Carbon,* 111, 269-282, 2017.

[17] Tang S and Hu C. Design, preparation and properties of carbon fiber reinforced ultra-high temperature ceramic composites for aerospace applications: a review. *Journal of Materials Science & Technology,* 33 (2), 117-130, 2017.

[18] Fahrenholtz W G, Hilmas G E, Talmy I G and Zaykoski J A. Refractory diborides of zirconium and hafnium. *Journal of the American Ceramic Society,* 90 (5), 1347-1364, 2007.

[19] Jin X, Fan X, Lu C and Wang T. Advances in oxidation and ablation resistance of high and ultra-high temperature ceramics modified or coated carbon/carbon composites. *Journal of the European Ceramic Society,* 38 (1), 1-28, 2018.

[20] Christensen A N. Crystal growth and characterization of the transition metal silicides MoSi2 and WSi2. *Journal of Crystal Growth,* 129 (1-2), 266-268, 1993.

[21] Ren X, Li H, Fu Q and Li K. Ultra-high temperature ceramic TaB_2–TaC–SiC coating for oxidation protection of SiC-coated carbon/carbon composites. *Ceramics International,* 40 (7), 9419-9425, 2014.

[22] Wang Y, Li Z, Xiong X, Li X, Chen Z and Sun W. Action mechanism of hydrogen gas on deposition of HfC coating using $HfCl_4$-CH_4-H_2-Ar system. *Applied Surface Science,* 390, 903-908, 2016.

[23] Gan J A and Berndt C C. Thermal spray forming of titanium and its alloys. in: Titanium Powder Metallurgy, Elsevier, pp. 425-446, 2015

[24] Paul A, Venugopal S, Binner J, Vaidhyanathan B, Heaton A and Brown P. UHTC–carbon fibre composites: preparation, oxyacetylene torch testing and characterisation. *Journal of the European Ceramic Society,* 33 (2), 423-432, 2013.

[25] Jayaseelan D D, De Sa R G, Brown P and Lee W E. Reactive infiltration processing (RIP) of ultra high temperature ceramics (UHTC) into porous C/C composite tubes. *Journal of the European Ceramic Society,* 31 (3), 361-368, 2011.

[26] Lu J, He Q, Wang Y, Li H and Fu Q. Preparation of co-deposited C/C-ZrC composites by CLVD process and its properties. *Journal of Alloys and Compounds,* 686, 823-830, 2016.

[27] Sayir A. Carbon fiber reinforced hafnium carbide composite. *Journal of Materials*

Science, 39 (19), 5995-6003, 2004.
[28] Li Y, Ma X, Hu H and Zhang Y. Influence of preparation temperature on the properties of C/ZrC composites. *Journal of Alloys and Compounds,* 690, 206-211, 2017.
[29] Paul A, Binner J, Vaidhyanathan B, Heaton A and Brown P M. Heat flux mapping of oxyacetylene flames and their use to characterise Cf-HfB_2 composites. *Advances in Applied Ceramics,* 115 (3), 158-165, 2016.
[30] Paul A, Rubio V, Binner J, Vaidhyanathan B, Heaton A and Brown P. Evaluation of the high temperature performance of HfB_2 UHTC particulate filled Cf/C composites. *International Journal of Applied Ceramic Technology,* 14 (3), 344-353, 2017.
[31] Guo S, Naito K and Kagawa Y. Mechanical and physical behaviors of short pitch-based carbon fiber-reinforced HfB_2–SiC matrix composites. *Ceramics International,* 39 (2), 1567-1574, 2013.
[32] Liyun C, Qun M, Jianfeng H and Xinping Y. Influence of hydrothermal treatment temperature on oxidation modification of C/C composites with aluminum phosphates solution by a microwave hydrothermal process. *Corrosion Science,* 52 (11), 3757-3762, 2010.
[33] Wang S, Zhu Y, Chen H, Li W and Chen Z. Effect of Cu on the ablation properties of Cf/ZrC composites fabricated by infiltrating Cf/C preforms with Zr-Cu alloys. *Ceramics International,* 41 (4), 5976-5983, 2015.
[34] Boisse P. Advances in composites manufacturing and process design. Woodhead Publishing, 2015
[35] Xue L, Su Z-a, Yang X, Huang D, Yin T, Liu C and Huang Q. Microstructure and ablation behavior of C/C–HfC composites prepared by precursor infiltration and pyrolysis. *Corrosion Science,* 94, 165-170, 2015.
[36] Xin Y, Qizhong H, Zhean S, Xin C, Liang X, Ping Z and Jun L. Ablative property and mechanism of C/C-ZrB_2-ZrC-SiC composites reinforced by SiC networks under plasma flame. *Corrosion Science,* 107, 9-20, 2016.
[37] Feng B, Li H, Zhang Y, Liu L and Yan M. Effect of SiC/ZrC ratio on the mechanical and ablation properties of C/C–SiC–ZrC composites. *Corrosion Science,* 82, 27-35, 2014.
[38] Wang Y, Zhu X, Zhang L and Cheng L. C/C–SiC–ZrC composites fabricated by reactive melt infiltration with $Si_{0.87}Zr_{0.13}$ alloy. *Ceramics International,* 38 (5), 4337-4343, 2012.
[39] Sun C, Li H, Fu Q and Zhang J. Microstructure and ablation properties of carbon/carbon composites modified by $ZrSiO_4$. *Corrosion Science,* 79, 100-107, 2014.
[40] Zhang Y-L, Li H-J, Wang P-Y, Li K-Z and Zeng X-R. Si–Mo–Cr coating for C/SiC coated carbon/carbon composites against oxidation. *Surface Engineering,* 28 (7), 544-547,

2012.

[41] Huang J, Hao W, Li H, Fu Q, Cao L, Li C, Yin L and Ouyang H. Oxidation kinetics of the $AlPO_4$ ceramic coatings by pulse arc discharge deposition on SiC–C/C composites. *Vacuum,* 112, 25-28, 2015.

[42] Yu Y, Luo R, Xiang Q, Zhang Y and Wang T. Anti-oxidation properties of a BN/SiC/Si_3N_4–ZrO_2–SiO_2 multilayer coating for carbon/carbon composites. *Surface and Coatings Technology,* 277, 7-14, 2015.

[43] Hu C, Niu Y, Huang S, Li H, Ren M, Zeng Y, Zheng X and Sun J. In-situ fabrication of ZrB_2–SiC/SiC gradient coating on C/C composites. *Journal of Alloys and Compounds,* 646, 916-923, 2015.

[44] Yang X, Ying L and Feng C. The degradation behavior of SiC coated PIP-C/SiC composites in thermal cycling environment. *Composites Part B: Engineering,* 79, 204-208, 2015.

[45] Evans A, Zok F and McMeeking R. Fatigue of ceramic matrix composites. *Acta Metallurgica et Materialia,* 43 (3), 859-875, 1995.

[46] Zheng G-B, Mizuki H, Sano H and Uchiyama Y. CNT–PyC–SiC/SiC double-layer oxidation-protection coating on C/C composite. *Carbon,* 46 (13), 1808-1811, 2008.

[47] Yanhui C, Qiangang F, Hejun L, Xiaohong S, Kezhi L, Xue W and Gunan S. Effect of SiC nanowires on the mechanical and oxidation protective ability of SiC coating for C/C composites. *Journal of the American Ceramic Society,* 95 (2), 739-745, 2012.

[48] Feng T, Li H, Fu Q, Shi X, Hu M and Liu L. Erosion resistance of Mo–Si–Cr coating-modified C/C composites in a wind tunnel at 1873 K. *Journal of Alloys and Compounds,* 622, 1049-1054, 2015.

[49] Fu Q-G, Jing J-Y, Li H-J, Jin X-X, Zhuang L and Li L. Design of an inlaid interface structure to improve the oxidation protective ability of SiC–$MoSi_2$–ZrB_2 coating for C/C composites. *Ceramics International,* 42 (3), 4212-4220, 2016.

[50] Shan Y-C, Fu Q-G, Li H-J, Fang Q, Liu X-S, Zhao R and Zhang P-F. Improvement of the bonding strength and the oxidation resistance of SiC coating on C/C composites by pre-oxidation treatment. *Surface and Coatings Technology,* 253, 234-240, 2014.

[51] Li K-z, Jing X, Qian-gang F, He-jun L and Ling-jun G. Effects of porous C/C density on the densification behavior and ablation property of C/C–ZrC–SiC composites. *Carbon,* 57, 161-168, 2013.

[52] Yan C, Liu R, Cao Y, Zhang C and Zhang D. Preparation and properties of 3D needle-punched C/ZrC–SiC composites by polymer infiltration and pyrolysis process. *Ceramics*

International, 40 (7), 10961-10970, 2014.

[53] Zhao Z, Li K, Li W, Liu Q, Kou G and Zhang Y. Preparation, ablation behavior and mechanism of C/C-ZrC-SiC and C/C-SiC composites. *Ceramics International*, 44 (7), 7481-7490, 2018.

[54] Tang S, Deng J, Wang S, Liu W and Yang K. Ablation behaviors of ultra-high temperature ceramic composites. *Materials Science and Engineering: A*, 465 (1-2), 1-7, 2007.

[55] Leslie C J, Boakye E E, Keller K A and Cinibulk M K. Development and Characterization of Continuous SiC Fiber-Reinforced HfB_2-Based UHTC Matrix Composites Using Polymer Impregnation and Slurry Infiltration Techniques. *International Journal of Applied Ceramic Technology,* 12 (1), 235-244, 2015.doi:10.1111/ijac.12279

[56] Wang Z, Liu X, Xu B and Wu Z. Fabrication and properties of HfB_2 ceramics based on micron and submicron HfB2 powders synthesized via carbo/borothermal reduction of HfO_2 with B_4C and carbon. *International Journal of Refractory Metals and Hard Materials*, 51, 130-136, 2015.

[57] Shen X-T, Liu L, Li W and Li K-Z. Ablation behaviour of C/C–ZrC composites in a solid rocket motor environment. *Ceramics International*, 41 (9), 11793-11803, 2015.

[58] Wang S-L, Li K-z, Li H-J, Zhang Y-L and Zhang W-Y. Ablation behavior of CVD-ZrC coating under oxyacetylene torch environment with different heat fluxes. *International Journal of Refractory Metals and Hard Materials*, 48, 108-114, 2015.

[59] Wu M, Le Guen K, André J-M, Jonnard P, Vickridge I, Schmaus D, Briand E, Walter P, Huang Q and Wang Z. Kossel diffraction observed with X-ray color camera during PIXE of nano-scale periodic multilayer. *Nuclear Instruments and Methods in Physics Research Section B: Beam Interactions with Materials and Atoms*, 2018.

[60] Windt D L. IMD—Software for modeling the optical properties of multilayer films. *Computers in physics*, 12 (4), 360-370, 1998.

[61] Henke B, CXRO database for x-ray attenuation length, in,

[62] Lee S-H, Yang T-H, Hyun S-H and Yoon Y-S. Corrosion behavior of pre-oxidized and thermally nitrided stainless steel for polymer electrolyte membrane fuel cell bipolar plates. *Corrosion Science*, 58, 79-85, 2012.

[63] Wang K-T, Cao L-Y, Huang J-F, Fei J and Zhang B-Y. Microstructure and oxidation resistance of C-$AlPO_4$－mullite coating prepared by hydrothermal electrophoretic deposition for SiC · C/C composites. *Ceramics International*, 39 (2), 1037-1044, 2013.

[64] Chen Z, Li H, Li K, Shen Q and Fu Q. Influence of grain size on wear behavior of SiC

coating for carbon/carbon composites at elevated temperatures. *Materials & Design*, 53, 412-418, 2014.

[65] Liu C, Cao L, Chen J, Xue L, Tang X and Huang Q. Microstructure and ablation behavior of SiC coated C/C–SiC–ZrC composites prepared by a hybrid infiltration process. *Carbon,* 65, 196-205, 2013.

[66] Luo R, Liu T, Li J, Zhang H, Chen Z and Tian G. Thermophysical properties of carbon/carbon composites and physical mechanism of thermal expansion and thermal conductivity. *Carbon,* 42 (14), 2887-2895, 2004.

[67] Zhang J-P, Fu Q-G, Zhang P-F, Qu J-L, Yuan R-M and Li H-J. Rapid heat treatment to improve the thermal shock resistance of ZrO_2 coating for SiC coated carbon/carbon composites. *Surface and Coatings Technology,* 285, 24-30, 2016.

[68] Feng T, Li H-J, Wang S-L, Hu M-H and Liu L. Boron modified multi-layer $MoSi_2$–$CrSi_2$–SiC–Si oxidation protective coating for carbon/carbon composites. *Ceramics International,* 40 (9), 15167-15173, 2014.

[69] Paul B, Majumdar S and Suri A. Microstructure and mechanical properties of hot pressed Mo–Cr–Si–Ti in-situ composite, and oxidation behavior with silicide coatings. *International Journal of Refractory Metals and Hard Materials*, 38, 26-34, 2013.

[70] Rao C N R, Deepak F, Gundiah G and Govindaraj A. Inorganic nanowires. *Progress in Solid State Chemistry,* 31 (1-2), 5-147, 2003.

[71] Zhang Y, Han X, Zheng K, Zhang Z, Zhang X, Fu J, Ji Y, Hao Y-j, Guo X-y and Wang Z. Direct observation of super‐plasticity of beta‐SiC nanowires at low temperature. *Advanced Functional Materials,* 17 (17), 3435-3440, 2007.

[72] Liu L, Li H, Feng W, Shi X, Wu H and Zhu J. Effect of surface ablation products on the ablation resistance of C/C–SiC composites under oxyacetylene torch. *Corrosion Science,* 67, 60-66, 2013.

[73] Yanhui C, Hejun L, Qiangang F, Xiaohong S, Lehua Q and Bingbo W. Oxidation-protective and mechanical properties of SiC nanowire-toughened Si–Mo–Cr composite coating for C/C composites. *Corrosion Science,* 58, 315-320, 2012.

[74] Choi S R, Hutchinson J W and Evans A. Delamination of multilayer thermal barrier coatings. *Mechanics of Materials,* 31 (7), 431-447, 1999.

[75] Poerschke D L, Novak M D, Abdul-Jabbar N, Krämer S and Levi C G. Selective active oxidation in hafnium boride-silicon carbide composites above 2000 C. *Journal of the European Ceramic Society,* 36 (15), 3697-3707, 2016.

[76] Jayaseelan D, Zapata-Solvas E, Chater R and Lee W. Structural and compositional

analyses of oxidised layers of ZrB_2-based UHTCs. *Journal of the European Ceramic Society,* 35 (15), 4059-4071, 2015.

[77] Sciti D, Silvestroni L and Bellosi A. High‐density pressureless‐sintered HfC‐based composites. *Journal of the American Ceramic Society,* 89 (8), 2668-2670, 2006.

[78] Feng L, Lee S H and Yin J. Low‐Temperature Sintering of HfC/SiC Nanocomposites Using HfSi2‐C Additives. *Journal of the American Ceramic Society,* 99 (8), 2632-2638, 2016.

[79] Feng L, Lee S-H, Wang H-L and Lee H-S. Nanostructured HfC–SiC composites prepared by high-energy ball-milling and reactive spark plasma sintering. *Journal of the European Ceramic Society,* 36 (1), 235-238, 2016.

[80] Yang Y, Li K, Zhao Z and Li H. Ablation resistance of HfC–SiC coating prepared by supersonic atmospheric plasma spraying for SiC-coated C/C composites. *Ceramics International,* 42 (4), 4768-4774, 2016.

[81] Luo L, Wang Y, Duan L, Liu L and Wang G. Ablation behavior of C/SiC-HfC composites in the plasma wind tunnel. *Journal of the European Ceramic Society,* 36 (15), 3801-3807, 2016.doi:10.1016/j.jeurceramsoc.2016.03.017

[82] Zhang J-P, Fu Q-G, Qu J-L, Zhuang L, Wang P-P and Li H-J. An inlaid interface of carbon/carbon composites to enhance the thermal shock resistance of SiC coating in combustion environment. *Surface and Coatings Technology,* 294, 95-101, 2016.

[83] Cui Y, Li A, Li B, Ma X, Bai R, Zhang W, Ren M and Sun J. Microstructure and ablation mechanism of C/C–SiC composites. *Journal of the European Ceramic Society,* 34 (2), 171-177, 2014.

[84] Chase Jr M W. NIST-JANAF thermochemical tables. *J. Phys. Chem. Ref. Data, Monograph,* 9, 1998.

[85] Landolt B and Börnstein R, Thermodynamic properties of inorganic materials, in, Berlin: Springer-Verlag, 1999,

[86] Parthasarathy T, Rapp R, Opeka M and Kerans R. A model for the oxidation of ZrB_2, HfB_2 and TiB_2. *Acta Materialia,* 55 (17), 5999-6010, 2007.

[87] Liu Q, Han W and Han J. Influence of SiCnp content on the microstructure and mechanical properties of ZrB_2–SiC nanocomposite. *Scripta Materialia,* 63 (6), 581-584, 2010.

[88] Zhou H, Gao L, Wang Z and Dong S. ZrB_2–SiC oxidation protective coating on C/C composites prepared by vapor silicon infiltration process. *Journal of the American Ceramic Society,* 93 (4), 915-919, 2010.

[89] Silvestroni L, Sciti D, Melandri C and Guicciardi S. Toughened ZrB_2-based ceramics through SiC whisker or SiC chopped fiber additions. *Journal of the European Ceramic Society,* 30 (11), 2155-2164, 2010.

[90] Kim J, Kim W-J, Choi D, Park J and Ryu W-S. Design of a C/SiC functionally graded coating for the oxidation protection of C/C composites. *Carbon,* 43 (8), 1749-1757, 2005.

[91] Wang Y-l, Xiong X, Li G-d, Liu H-f, Chen Z-k, Sun W and Zhao X-j. Ablation behavior of HfC protective coatings for carbon/carbon composites in an oxyacetylene combustion flame. *Corrosion Science,* 65, 549-555, 2012.

[92] Subercaze A, Koumeir C, Métivier V, Servagent N, Guertin A and Haddad F. High energy PIXE: A tool to characterize multi-layer thick samples. *Nuclear Instruments and Methods in Physics Research Section B: Beam Interactions with Materials and Atoms,* 417, 41-45, 2018.doi:10.1016/j.nimb.2017.09.009

[93] Midy P and Brissaud I. Application of a new algorithm to depth profiling by PIXE. *Nuclear Instruments and Methods in Physics Research Section B: Beam Interactions with Materials and Atoms,* 103 (4), 489-493, 1995.

[94] Kossel W, Loeck V and Voges H. Die Richtungsverteilung der in einem Kristall entstandenen charakteristischen Röntgenstrahlung. *Zeitschrift für Physik,* 94 (1-2), 139-144, 1935.

[95] Tixier R and Wache C. Kossel patterns. *Journal of Applied Crystallography,* 3 (6), 466-485, 1970.

[96] Martínez-González J A, Li X, Sadati M, Zhou Y, Zhang R, Nealey P F and de Pablo J J. Directed self-assembly of liquid crystalline blue-phases into ideal single-crystals. *Nature communications,* 8, 15854, 2017.

[97] Langer E, Däbritz S, Schurig C and Hauffe W. Lattice constant determination from Kossel patterns observed by CCD camera. *Applied Surface Science,* 179 (1-4), 45-48, 2001.

[98] Jonnard P, André J-M, Bonnelle C, Bridou F and Pardo B. Soft-x-ray Kossel structures from W/C multilayers under various electron ionization conditions. *Physical Review A,* 68 (3), 032505, 2003.

[99] Aiken A C, DeCarlo P F and Jimenez J L. Elemental analysis of organic species with electron ionization high-resolution mass spectrometry. *Analytical Chemistry,* 79 (21), 8350-8358, 2007.

[100] Goldstein J I, Newbury D E, Michael J R, Ritchie N W, Scott J H J and Joy D C. Scanning electron microscopy and X-ray microanalysis. Springer, 2017

[101] Rousse A, Phuoc K T, Shah R, Pukhov A, Lefebvre E, Malka V, Kiselev S, Burgy F,

Rousseau J-P and Umstadter D. Production of a keV X-ray beam from synchrotron radiation in relativistic laser-plasma interaction. *Physical Review Letters,* 93 (13), 135005, 2004.
[102] Jonnard P, Yuan Y, Le Guen K, André J-M, Zhu J, Wang Z and Bridou F. Spontaneous soft x-ray fluorescence from a superlattice under Kossel diffraction conditions. *Journal of Physics B: Atomic, Molecular and Optical Physics,* 47 (16), 165601, 2014.
[103] Lucarelli F, Calzolai G, Chiari M, Giannoni M, Mochi D, Nava S and Carraresi L. The upgraded external-beam PIXE/PIGE set-up at LABEC for very fast measurements on aerosol samples. *Nuclear Instruments and Methods in Physics Research Section B: Beam Interactions with Materials and Atoms,* 318, 55-59, 2014.
[104] Guen K L, Andre J M, Wu M, Ilakovac V, Delmotte F, Rossi S, Bridou F, Meltchakov E, Giglia A, Nannarone S, Wang Z, Huang Q, Zhang Z, Zhu J, Tu Y, Yuan Y, Vickridge I, Schmaus D, Briand E, Steydli S, Walter P and Jonnard P. Kossel Effect in Periodic Multilayers. *J Nanosci Nanotechnol,* 19 (1), 593-601, 2019.
[105] Faigel G, Bortel G and Tegze M. Experimental phase determination of the structure factor from Kossel line profile. *Scientific Reports,* 6, 22904, 2016.
[106] Wu M, Le Guen K, André J-M, Ilakovac V, Vickridge I, Schmaus D, Briand E, Steydli S, Burcklen C, Bridou F, Meltchakov E, de Rossi S, Delmotte F and Jonnard P. Kossel interferences of proton-induced X-ray emission lines in periodic multilayers. *Nuclear Instruments and Methods in Physics Research Section B: Beam Interactions with Materials and Atoms,* 386, 39-43, 2016.
[107] Chauvineau J-P and Bridou F. Analyse angulaire de la fluorescence du fer dans une multicouche périodique Fe/C. *Le Journal de Physique IV,* 6 (C7), C7-53-C57-64, 1996.
[108] Solé V, Papillon E, Cotte M, Walter P and Susini J. A multiplatform code for the analysis of energy-dispersive X-ray fluorescence spectra. *Spectrochimica Acta Part B: Atomic Spectroscopy,* 62 (1), 63-68, 2007.
[109] Sato K, Hongu H, Ikekame H, Watanabe J, Tsuzukiyama K, Togami Y, Fujisawa M and Fukazawa T. Magnetooptical Spectra in Pt/Co and Pt/Fe Multilayers. *Japanese journal of applied physics,* 31 (11R), 3603, 1992.
[110] Díaz B, Światowska J, Maurice V, Pisarek M, Seyeux A, Zanna S, Tervakangas S, Kolehmainen J and Marcus P. Chromium and tantalum oxide nanocoatings prepared by filtered cathodic arc deposition for corrosion protection of carbon steel. *Surface and Coatings Technology,* 206 (19-20), 3903-3910, 2012.
[111] Hu W, Xu J, Lu X, Hu D, Tao H, Munroe P and Xie Z-H. Corrosion and wear behaviours of a reactive-sputter-deposited Ta_2O_5 nanoceramic coating. *Applied Surface*

Science, 368, 177-190, 2016.

[112] Asteman H and Spiegel M. A comparison of the oxidation behaviours of Al_2O_3 formers and Cr2O3 formers at 700°C–Oxide solid solutions acting as a template for nucleation. *Corrosion Science,* 50 (6), 1734-1743, 2008.

[113] Hüppauff M, Bange K and Lengeler B. Density, thickness and interface roughness of SiO_2, TiO_2 and Ta_2O_5 films on BK-7 glasses analyzed by x-ray reflection. *Thin Solid Films,* 230 (2), 191-198, 1993.

[114] Roine A. HSC Chemistry® for Windows, Chemical Reaction and Equilibrium Software with Extensive Thermochemical Database, Version 5.0. *Pori,(Finland). Outokumpu Research Oy, Information Service, PO Box,* 60, 2002.

[115] Europe S G T. Thermodynamic properties of inorganic materials. *Landolt-Boernstein New Series, Group IV,* 1999.

[116] Li M, Sun X, Li J, Zhang Z, Jin T, Guan H and Hu Z. Oxidation behavior of a single-crystal Ni-base superalloy in air. I: at 800 and 900 C. *Oxidation of Metals,* 59 (5-6), 591-605, 2003.

[117] Ren W, Ouyang F, Ding B, Zhong Y, Yu J, Ren Z and Zhou L. The influence of $CrTaO_4$ layer on the oxidation behavior of a directionally-solidified nickel-based superalloy at 850–900° C. *Journal of Alloys and Compounds,* 724, 565-574, 2017.

[118] Squire T H and Marschall J. Material property requirements for analysis and design of UHTC components in hypersonic applications. *Journal of the European Ceramic Society,* 30 (11), 2239-2251, 2010.

[119] Zhang J-P, Fu Q-G, Li H-J, Sun G-D, Sun C, Nan X-Y, Li S-F and Liu L. Ablation behavior of Y_2SiO_5/SiC coating for C/C composites under oxyacetylene torch. *Corrosion Science,* 87, 472-478, 2014.

[120] Ni D-W, Zhang G-J, Xu F-F and Guo W-M. Initial stage of oxidation process and microstructure analysis of HfB2–20 vol.% SiC composite at 1500 C. *Scripta Materialia,* 64 (7), 617-620, 2011.

[121] Cuiyan L, Kezhi L, Hejun L, Haibo O, Yulei Z and Lingjun G. Ablation resistance and thermal conductivity of carbon/carbon composites containing hafnium carbide. *Corrosion Science,* 75, 169-175, 2013.

[122] Monteverde F and Bellosi A. The resistance to oxidation of an HfB_2–SiC composite. *Journal of the European Ceramic Society,* 25 (7), 1025-1031, 2005.

[123] Zhang J-P, Fu Q-G and Wang L. Preparation, ablation behavior and thermal retardant ability of C/C-HfB_2-SiC composites. *Materials & Design,* 132, 552-558, 2017.

[124] Poilov V Z and Pryamilova E N. Thermodynamics of oxidation of zirconium and hafnium borides. *Russian Journal of Inorganic Chemistry,* 61 (1), 55-58, 2016.

[125] Beaudet J, Cormier J, Dragon A, Rollin M and Benoit G. Ablation Properties of C Fibers and SiC Fibers Reinforced Glass Ceramic Matrix Composites Upon Oxyacetylene Torch Exposure. *Materials Sciences and Applications,* 02 (10), 1399-1406, 2011.

Protection contre l'oxydation des composites carbone/carbone et développement de méthodes de caractérisation non destructives

Résumé :

Les composites de carbone renforcés de fibres de carbone (C/C) possèdent de nombreuses propriétés uniques, telles qu'une faible densité (< 2.0 g/cm^3), une résistance/module spécifique élevé, un faible coefficient de dilatation thermique et une excellente résistance aux chocs thermiques. Ils ont été utilisés comme matériaux structurels dans les boucliers thermiques des véhicules et les freins des avions. Cependant, le carbone est sensible à l'oxydation à haute température. L'idée principale de cette thèse est de développer une technologie de protection contre l'oxydation/ ablation pour C/C, qui proposait une technologie de revêtement et une modification de la matrice. concevoir une interface de couplage revêtement/substrat. En outre, afin de mieux évaluer la fiabilité de service du revêtement, des interférences de Kossel d'émissions de rayons X induites par un proton combinées à une réflectivité des rayons X, en tant que nouvelle méthode de caractérisation non destructive, ont été développées. La faisabilité de cette méthode a été confirmée dans les films de guides d'ondes planaires. Cette méthodologie est prometteuse pour nous d'évaluer la fiabilité de service de multicouches HfC/SiC/HfC pour C/C en application réelle. Pour la technologie de modification de matrice, les céramiques HfB_2 et HfB_2-SiC ont été introduites dans un substrat C/C. Combinés à l'analyse thermogravimétrique et à la mesure des performances d'oxydation/ablation, le rôle des céramiques HfB_2 et HfB_2-SiC a été examiné.

Mots-clés: composites carbone/carbone; Technologie de revêtement; L'ablation; Émission de rayons X induite par des particules; Diffraction de Kossel; Modification de la matrice; HfB_2-SiC.

Oxidation protection of carbon/carbon composites and non-destructive characterization methodology development

Abstract :

Carbon fiber reinforced carbon composites (C/C) possess many unique properties, such as low-density (< 2.0 g/cm^3), high specific strength/modulus, low coefficient of thermal expansion and excellent thermal shock resistance. They have been used as the structural materials in vehicle heat shields and aircraft brakes. However, carbon is sensitive to oxidation at high temperature. The main idea of this thesis is to develop oxidation/ablation protection technology for C/C, where coating technology and matrix modification were proposed. To improve the adhesive strength and relieve the thermal expansion mismatch between the coating and the substrate, blasting treatment was proposed to design an interlock coating/substrate interface. Additionally, to better evaluate the service reliability of the coating, Kossel interferences of proton-induced X-ray emissions combined with X-ray reflectivity, as a novel non-destructive characterization method, were developed. The feasibility of this method was confirmed in planar waveguides films. This methodology is promising for us to evaluate the service reliability of HfC/SiC/HfC multilayer for C/C in actual application. For the matrix modification technology, HfB_2 and HfB_2-SiC ceramics were introduced into C/C substrate. Combined with thermogravimetric analysis and oxidation/ablation performance measurement, the role of HfB_2 and HfB_2-SiC ceramics were discussed.

Keywords : Carbon/carbon composites; Coating technology ; Ablation ; Particle-induced X-ray emission ; Kossel diffraction ; Martix modification ; HfB_2-SiC.